# Structural insights into the catalytic binuclear center of cytochrome *c* oxidase from *Paracoccus denitrificans*

**Dissertation**

Zur Erlangung des Doktorgrades der Naturwissenschaften vorgelegt dem Fachbereich Biochemie, Chemie und Pharmazie der Johann Wolfgang-Goethe-Universität in Frankfurt am Main

von

**Felix Martin Kolbe**
aus Stade

Frankfurt am Main (2021)
(DE30)

vom Fachbereich 14 Biochemie, Chemie und Pharmazie der Johann Wolfgang-Goethe-Universität als Dissertation angenommen.

**Dekan:** Prof. Dr. Clemens Glaubitz

**Gutachter**: Prof. Dr. Clemens Glaubitz

**Gutachter**: Prof Dr. Dr. h.c. Harmut Michel

Datum der Disputation: 21.02.2022

Diese Dissertation wurde im November 2016 bis Juli 2021 unter Leitung von Prof. Dr. Dr. h.c. Hartmut Michel in der Abteilung Molekulare Membranbiologie am Max-Planck-Institut für Biophysik in Frankfurt am Main durchgeführt.

**Eidesstattliche Erklärung**

Hiermit versichere ich, dass ich die vorliegende Arbeit selbstständig angefertigt habe und keine anderen, als die angegeben Hilfsmittel und Quellen, verwendet habe.

_____

(Felix Kolbe)

Frankfurt am Main, den

Except where stated otherwise by reference or acknowledgment, the work presented in this thesis was generated by myself under the supervision of my advisors during my doctoral studies. Whenever a figure, table or text is identical to a previous publication, copyright permission has been obtained.

The following parts of the thesis were generated by me and have been published afterwards:

Parts of Section I

Parts of Section II

Parts of Section III, Fig. 3.2, Fig. 3.5, Fig. 3.6, Fig. 3.9, Fig. 3.11, Fig 3.12, Fig. 3.12, Fig. 3.13, Fig. 3.14, Fig. 3.16, Fig. 3.17, Fig. 3.18, Fig. 3.19, Fig. 3.20, Fig. 3.21, table 3.1

Parts of Section IV, Fig. 4.2

the above-mentioned contents have been published in

**Kolbe, F**., Safarian, S., Piórek, Ż. *et al*. Cryo-EM structures of intermediates suggest an alternative catalytic reaction cycle for cytochrome *c* oxidase. *Nat Commun* **12,** 6903 (2021). https://doi.org/10.1038/s41467-021-27174-y

According to the copyright policy of Nature, I as author retain copyright to my article and do not need to obtain permission to include content from my article as part of my dissertation.

See details: https://www.nature.com/nature-portfolio/reprints-and-permissions/permissions-requests

The following figure of the thesis are adapted from previous publications:

Figure 2.1

The original publication of this figure has been referenced and copyright permission licenses have been obtained

See copyright permission licenses in Appendix

## Declaration of collaborative work

Section 2.1.1 Zaneta Piorek[1] produced cytochrome *c* oxidase from rec. wildtype *Paracoccus denitrificans*

Section 2.1.2 Hannelore Müller[2] and assisted with the production and protein purification of the antibody-fragment from E. coli JM83

Section 2.1.3 Hannelore Müller[2] assisted with protein purification of cytochrome *c* oxidase from *Paracoccus denitrificans*

Section 2.2.4 Schara Safarian[3] assisted with grid freezing processes for the cytochrome *c* oxidase

2.2.5 Sonja Welsch[4] gave introduction, provided technique support and supervised data acquisition on Titan Krios G2 of cytochrome *c* oxidase

Section 3.5 Schara Safarian[3] supervised the data processing and interpretation of resulting density maps for each intermediate state of the cytochrome *c* oxidase

Zaneta Piorek[1], Department of Molecular Membrane Biology, Max Planck Institute of Biophysics, D-60438, Frankfurt/Main, Germany

Present address: Institute of Pharmaceutical Chemistry, Phillips University Marburg, D-35032, Marburg, Germany

Hannelore Müller[2], Department of Molecular Membrane Biology, Max Planck Institute of Biophysics, D-60438, Frankfurt/Main, Germany

Schara Safarian[3], Department of Molecular Membrane Biology, Max Planck Institute of Biophysics, D-60438, Frankfurt/Main, Germany

Sonja Welsch, Central Electron Microscopy Facility, Max Planck Institute of Biophysics, D-60438, Frankfurt/Main, Germany

# Contents

# 1. Abbreviations

| | |
|---|---|
| NADH | Nicotinamide adenine dinucleotide |
| eV | Electronvolt |
| ATP | Adenosine-5'-triphosphate |
| C*c*O | Cytochrome *c* oxidase |
| BNC | Binuclear center |
| *P. denitrificans* | *Paracoccus denitrificans* |
| HCO | Heme copper oxidase |
| Å | Ångström |
| PLS | Proton loading site |
| ΔG | Free enthalpy |
| $E_m$ | Redox midpoint potential |
| mV | Millivolt |
| kDa | Kilo Dalton |
| *K* | Rate constant |
| K | Kelvin |
| EPR | Electron Paramagnetic Resonance |
| XFEL | X-ray free electron laser |
| EM | Electron microscopy |
| NMR | Nuclear magnetic resonance |
| FTIR | Fourier-transform infrared |
| KPi | Potassium phosphate |
| DDM/LM | *n*-dodecyl-β-D-maltophyranoside, "lauryl maltoside" |
| IPTG | Isopropyl-β-D-thiogalactopyranosid |
| MSP | Membrane scaffold protein |
| Tris | Tris-(hydroxymethyl)-aminomethane |
| CV | Column volume |
| PMSF | Phenylmethylsulfonylfluorid |
| POPC | 1-palmitoyl-2-oleoyl-glycero-3-phosphocholine |
| SDS | Sodium dodecyl sulfate |
| EDTA | Ethylenediamine-tetraacetic acid |
| MES | 2-(N-morpholino)ethanesulfonic acid |
| TMPD | Tetramethylphenylene-diamine |
| TEV | Tobacco Etch Virus |
| IMAC | Immobilized metal affinity chromatography |
| Gyr | Billion years |

# 1. Introduction – Structure and function of cytochrome *c* oxidase

## 1.1 The respiratory chain and cytochrome *c* oxidase

The membrane integrated cytochrome *c* oxidase (E.C. 1.9.3.1), C*c*O, is the terminal enzyme of the respiratory chain of mitochondria and many bacteria, being capable of reducing molecular oxygen (dioxygen) to water promoted by the heme-containing protein cytochrome *c.* This reduction process is exergonic by 2.2 eV [1] and mainly invested into the generation of an electrochemical gradient of protons across the membrane, consisting of a pH-gradient and an electric voltage ("membrane potential"). This electrochemical proton gradient is of great importance as it significantly contributes to the synthesis of adenosine-5'-triphosphate (ATP) from adenosine-5'-diphosphate (ADP) and inorganic phosphate (Pi), catalyzed by the $F_oF_1$-ATP synthase and driven by the coupled backflow of protons, providing an indispensable energy source for numerous biological processes. Two complex processes contribute to the energy conservation, namely electrogenic chemistry and proton pumping. The redox

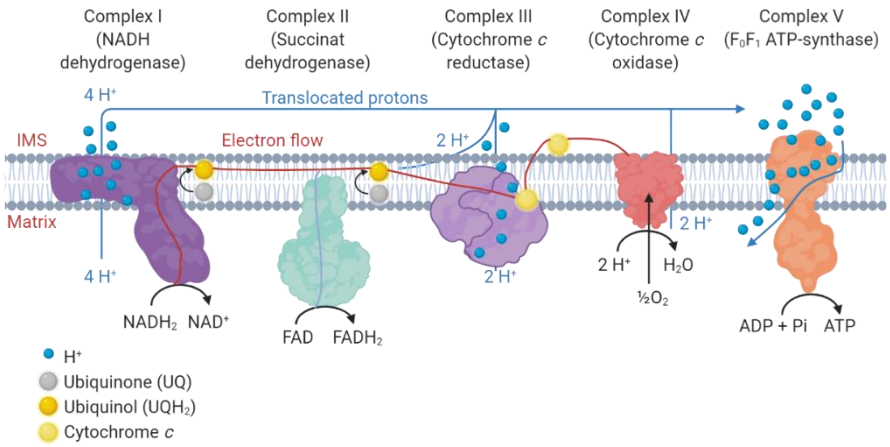


**Figure 1.1**. **Schematic representation of the respiratory chain**. Showing the electron transport chain coupled with proton translocation from complex I to complex IV where the reduction of molecular oxygen takes place. NADH and $FADH_2$ act as electron donors and cofactors in the electron transfer pathway. Oxidative phosphorylation takes place in complex V. The figure was prepared by BioRender.

reaction itself is coupled to the formation of a membrane potential and a pH gradient across the membrane as four electrons from cytochrome *c* and four "substrate" protons are taken up from opposite sides of the membrane, facilitating the reduction of molecular oxygen to water. Furthermore, this redox process is accompanied by active proton translocation from one side of the membrane to the other, - referred as "proton pumping", – with a stoichiometry of one proton per electron ($H^+/e^-$ = 1) [2]. Hence, the turnover reaction can be described as

$$4 \text{ cyt } c^{2+} + 8 H^+_i + O_2 \rightarrow 4 \text{ cyt } c^{3+} + 4 H^+_o + 2 H_2O$$

where $H_i^+$ (i = inside) represents protons taken from the matrix of mitochondria or the cytoplasm of bacteria and $H_o^+$ (o = outside) refers to protons released to the outside.

The respiratory chain is an electron transport chain consisting of four different protein complexes which are of great meaning for the oxidative phosphorylation (Fig 1.1). The membrane protein complexes are described as follows:

1. The NADH:ubiquinone-oxidoreductase or complex I is known for its characteristic L-shape and is capable of oxidizing NADH to $NAD^+$ and reduces ubiquinone to ubiquinol. In order to make this possible, the complex translocates four protons across the inner membrane per molecule of oxidized NADH [3].
2. Complex II is the succinate:ubiquinone-oxidoreductase. This membrane protein connects the citric acid cycle to the respiratory chain and is responsible for the oxidation of succinate to fumarate combined with the reduction of ubiquinone to ubiquinol. This complex is not known for pumping protons across the membrane [4].
3. The ubiquinol:cytochrome *c*-oxidoreductase is the third membrane protein in the respiratory chain. This complex is responsible for switching the electron-transport chain from a two-electron transport into a one-electron transport. Thereby, ubiquinol gets oxidized and turns into ubiquinone and two protons are released into the intermembrane space. The first electron is used for reducing cytochrome *c*. The second electron is transported back to a second ubiquinone binding site near the mitochondrial matrix, subsequently reducing ubiquinone to ubiquinol, using protons from the mitochondrial matrix. Therefore, Complex III contributes greatly to the increment of the proton gradient [5].

4. Complex IV, known as the cytochrome *c*:oxygen-oxidoreductase, reduces incoming molecular oxygen to water by oxidizing the electron donor cytochrome *c*. During one reaction cycle of C*c*O, four electrons are required for the reducing process. For substrate formation, four protons are consumed from the mitochondrial matrix and another four are pumped across the inner membrane into the intermembrane space.

Cytochrome *c* oxidase belongs to the heme/copper oxidase superfamily where the reduction reaction occurs at the binuclear center (BNC), characterized by a five-coordinated high spin heme iron ($a_3$ and $o_3$ in the A and B families, $b_3$ in the c family) and a copper atom ($\mathrm{Cu}_B$). In addition to that, a second low-spin heme is residing in proximity to the binuclear center, playing a significant role for electron transfer together with two copper atoms ($\mathrm{Cu}_A$). Bacterial respiratory chains are branched and may accommodate different types of heme groups (A, B or O hemes), whereas mitochondrial oxidases only utilize a-type heme. These different types of protein complexes are classified into three main groups: heme/Cu-containing oxidase superfamily, *bd*-type quinol oxidase family, and alternative oxidase family. The enzyme that is subject of this study is a $aa_3$-type cytochrome *c* oxidase from the soil bacterium *Paracoccus denitrificans*, belonging to the A-type heme/Cu-containing superfamily. Present in respiratory chains of prokaryotes and eukaryotes, aerobic terminal oxidoreductases are classified into different families based on different structural and functional properties.

### 1.2 Molecular oxygen – a turning point in earth's history

Approximately three billion years ago, ancestors of the cyanobacteria developed the ability to extract electrons from water, a process termed as oxygenic photosynthesis. As a consequence, photosynthesis-induced enrichment of the earth's atmosphere with dioxygen ($O_2$) led to dramatic changes on the planet's environment approximately 2.4 Gyr ago, known as the Great Oxygenation Event (GOE) [6]. Predominant obligate anerobic organisms were intoxicated by a rising level of molecular oxygen and reactive oxygen species (ROS) which led inevitably to one of the greatest mass extinctions events on earth. Evolutionary adaption was the only key to survive this oxygen threat either by inhabiting anaerobic niches or by inventing detoxifying biochemical strategies. In this dynamic process, complex macromolecular complexes were assembled capable of preventing damage caused by molecular oxygen. Superoxide dismutases catalyze the dismutation of superperoxide anions to either dioxygen or hydrogen peroxide while catalases are capable of converting peroxides to dioxygen and water in a two-step reaction [7, 8]. With the time, different types of enzymatic machineries have developed their own path to catalyze the direct reduction from molecular oxygen to water. As molecular oxygen is commonly present in high concentrations in the hydrophobic core of biomembranes, many organisms have devised membrane-integrated enzymes like the well-characterized terminal oxygen reductases of the heme-copper oxidase (HCO) superfamily to coexist with atmospheric molecular oxygen.

### 1.3 Three-dimensional structure and content of the metal cofactors in cytochrome *c* oxidase

The first crystallographic structure of the cytochrome *c* oxidase from *P. denitrificans* was solved by Iwata *et al.* in 1995 [9, 10] . The determination of the three-dimensional structure can be considered as a milestone as it gave first insights into the overall composition of the membrane protein and its binuclear center where the reduction of oxygen to water occurs. Concurrently, the mammalian structure from bovine heart mitochondria was determined providing additional insight, displaying a high structural similarity for the first three subunits between both A-type C*c*O [11]. While the bovine heart C*c*O is composed of thirteen subunits (dimeric form), the structure of the C*c*O in *P. denitrificans* is formed by four, commonly divided into three core subunits (I-III) and one small non-conserved subunit (IV) (Fig.1.2).

The first subunit is the largest one harboring twelve transmembrane helices with an approximate threefold rotational symmetric arrangement and contains three redox centers: low-spin heme $a$, high-spin heme $a_3$ and the copper ion $\mathrm{Cu}_B$. Both hemes

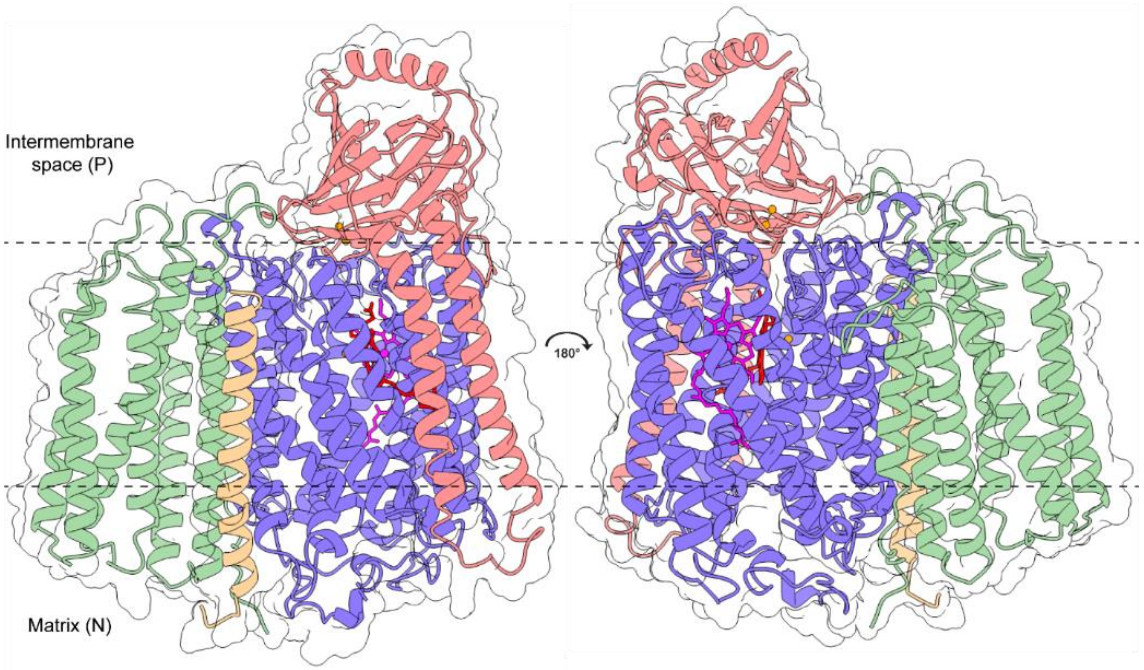


**Figure 1.2. Ribbon representation with modelled surface of the four-subunit cytochrome c oxidase from *P. denitrificans*** (PDB 7AU6). Subunits I, II, III and IV are shown in blue, red, green and yellow, respectively. Copper atoms are represented as orange spheres, heme $a$ and $a_3$ are shown in magenta and red as sticks, respectively. The surface of the structure is contoured in white. The figure was prepared by using ChimeraX

have an edge-to-edge distance of approximately 4.8 Å (13 Å metal-to-metal) and are embedded in the transmembrane region with a distance of roughly 20 Å away from the periplasmic surface and 34 Å from the cytoplasm (Fig.1.3). Heme $a$ is connected with two conserved histidine imidazole ligands ($His^{94.I}$, $His^{413.I}$), each of them axially aligned to the centralized iron atom. For heme $a_3$, another conserved histidine ($His^{411.I}$) operates as an axial ligand and appears to traverse structural motion upon dioxygen reduction [12]. The $Cu_B$ ion is coordinated by three additional histidine imidazole ligands ($His^{276.I}$, $His^{325.I}$, $His^{326.I}$) and is located 4.6 Å apart from the heme $a_3$ ion. Heme $a_3$ and $Cu_B$ together form a binuclear center and the oxygen reduction site of the enzyme. Beside the aforementioned three redox centers accommodated by subunit I, a fourth metal center ($Cu_A$) is located in subunit II which is significantly important for functioning electron transfer. Each copper atom is bridged by two cysteine residues ($Cys^{216.II}$, $Cys^{220.II}$) and one exclusive histidine residue for each ($His^{181.II}$, $His^{224.II}$). In this context, it should be noted that this metal center is absent in ubiquinol oxidases such as cytochrome *bo3* from *E.coli* which also belongs to the superfamily of heme/copper oxidases [13]. The role of subunit III and IV remains elusive as they appear not to have a functional relevance for the complex itself. There have been several studies in the past addressing their potential relevance either in terms of functionality or structural integrity, pointing out that deletion of subunit IV has no obvious effect on the enzymatic properties, expression, assembly and bacterial growth [14, 15].

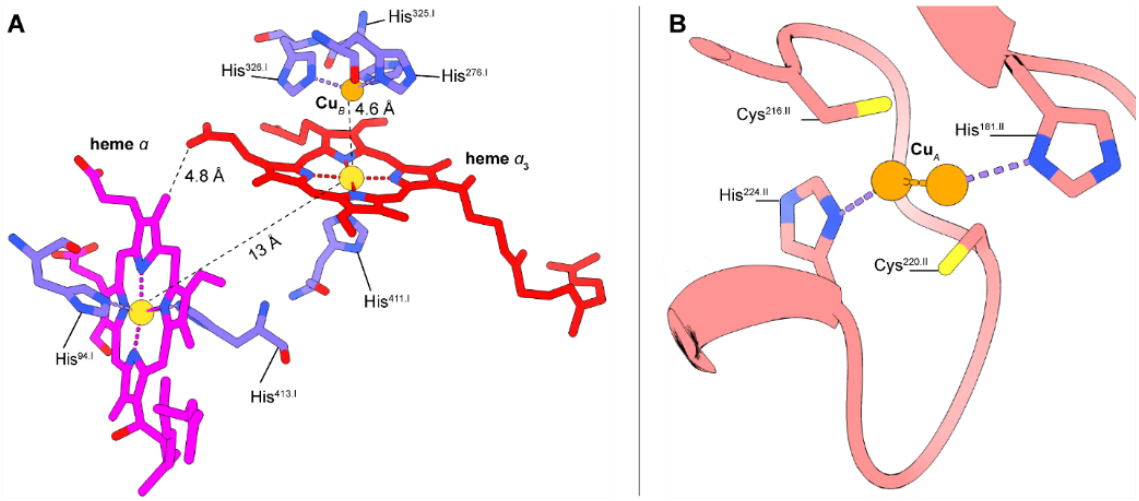


**Figure 1.3**. **Redox cofactors in cytochrome *c* oxidase**. **(A)** Depiction of all three redox cofactors (heme $a$, heme $a_3$ , $Cu_B$) and their ligated amino acids embedded in subunit I. Edge-to-edge and metal-to-metal distances are indicated. The iron atom is shown as yellow. **(B)** Location of the cupredoxin-type conformation bridged by two cysteine residues ($Cu_A$) in subunit II. The figure was prepared by using ChimeraX.

Even though there is a clarified picture of the general enzyme topography, detailed understanding of the redox processes and related structural rearrangements upon dioxygen reduction at the catalytic site remains mainly unknown [16]. Especially the true nature of the residing ligands in the binuclear center under turnover conditions are of great interest as they could reveal more about the mechanistic chemistry in cytochrome *c* oxidases.

### 1.4 Proton-coupled electron transfer in cytochrome *c* oxidase

For maintaining an unobstructed turnover of dioxygen reduction to water in terminal respiratory oxidases, precise uptake and translocation of protons as well as electrons are required to achieve a thermodynamically favored equilibrium. In contrast to proton conduction which is based on the so-called “Grotthuss mechanism” and uses protonatable protein residues as “proton wires” for proton translocation, electrons are approximately 2,000 times smaller in regard to their size and are influenced by quantum mechanical effects [17]. The directed electron transfer process is finely organized by thermodynamic driving forces which are mainly determined by the redox potential differences between acceptor and donor groups and associated electronic couplings based on their spatial distances [18].

As described in the previous section, the process of oxygen reduction in terminal heme-copper oxidases is closely linked to proton translocation from the cytoplasm or the mitochondrial matrix into the periplasm or mitochondrial intermembrane space (Fig 1.5). This transfer is responsible for generating a proton and charge gradient across the membrane. However, the exact molecular mechanism by which the two processes – electron transfer and proton movement – are connected to each other is still a matter of debate. Originally, two different schemes appeared to be likely: an indirect mechanism in which the occurring reduction of molecular oxygen is causing major conformational changes in the protein, or a direct mechanism where the coupling is achieved by rather minor structural changes in the proximity of the redox centers. As no major structural rearrangements for the redox centers and neighboring transmembrane helices were observed in reported structures of the cytochrome *c* oxidase, an indirect mechanism was excluded. Instead, a mechanistic sequence of

proton-pumping is considered as rather likely. As recently postulated by Fadda *et al.* and briefly summarized for this work, a proton-loading site (PLS), presumably located in close proximity to the A-ring propionate of heme $a_3$, receives a proton from the N-phase when an electron resides at the electron-queuing site, heme $a$, which has raised the pKa of the PLS. The residing proton in the PLS raises the redox potential of the BNC and facilitates electron transfer from heme $a$ to this site, which occurs with the same kinetics as the loading of the PLS. The electron in the BNC attracts a "chemical" proton more than it attracts the proton in the PLS (shorter electron/proton distance). Consequently, a proton is taken up from the N-side into the BNC and this expels the proton from the PLS into the P-phase by electrostatic repulsion [19, 20]. However, this mechanistic proposal is bringing up new questions as it fails to address securing the directionality of pumped protons ("proton-leaking").

### 1.4.1 Binding of cytochrome *c* and electron transfer

After docking of the reduced cytochrome *c* to the periplasmic P-side, electrons are accepted by $\mathrm{Cu}_A$ and forwarded via heme $a$ to its final destination, the binuclear center consisting of heme $a_3$ and the copper ion $\mathrm{Cu}_B$ where the oxygen reduction takes place (Fig.1.4). As mentioned before, the cytochrome *c* oxidase operates as a redox-driven proton pump that is capable of using the free-energy gap (ΔG cyt *c* → $O_2$ ~ -0.6 to 0.9 eV per electron) coming from the electron donor cytochrome *c* ($E_{m,7}$ = +250 mV) and the electron accepting substrate ($O_2$, $E_{m,7}$ = +810 mV) [20]. Cytochrome *c* itself is a small, ~12 kDa soluble electron carrier protein which transfers electrons between complex III and complex IV in the respiratory chain super complex. A consistent structural feature of this soluble protein, with few exceptions (e.g. *Bacillus subtilis*), is a covalently linked heme *c* to cysteine residues in a strictly conserved CXXCH motif. To enable binding of the positively charged cytochrome *c* to the negatively charged binding site of C*c*O, this process is driven by electrostatic forces, facilitated by numerous present carboxylate groups in the hydrophilic P-side (SU II) and conserved lysines located around the heme in cytochrome *c* [21]. It should be noted that the electron transfer between cytochrome *c* and C*c*O is remarkably fast (~6 x $10^4$ $s^{-1}$), but the overall cytochrome *c* oxidase reaction is determined by the formation between

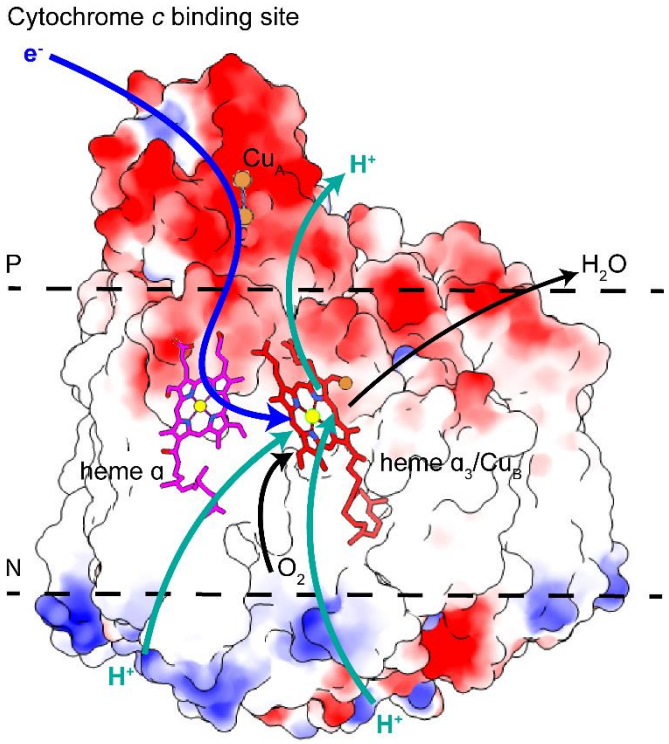


**Figure 1.4. Mapped electrostatic potentials derived from surface-exposed residues from *P. denitrificans* cytochrome *c* oxidase**. Stepwise electron transfer occurs from cytochrome *c* (not shown) to $Cu_A$ (orange), heme $a$ (magenta) and heme $a_3/Cu_B$ (red) and consequently consumed for the redox reaction. To do so, the uptake of protons is required by two individual proton transfer channels (turquoise line). The figure was prepared by using ChimeraX.

both redox proteins [22, 23]. Brownian dynamic simulations addressed this protein-protein interaction and predicted a high rate of 2 x $10^6$ $M^{-1}$ $s^{-1}$ which is obtained by diffusive processes and excludes attractive or steering forces [24]. From $Cu_A$, electrons are rapidly forwarded to heme $a$, depending on the source of enzyme ($K_{bovine}$ ~2 x $10^4$ $s^{-1}$, $K_{bacterial}$ ~4-6 x $10^4$ $s^{-1}$) demonstrated in various studies [25-28]. The direct electron transfer from $Cu_A$ to heme $a$ can be considered as highly probable as modifications to the pH or neighboring water networks showed no effect [29]. In addition, direct electron transfer from $Cu_A$ to heme $a_3$ has been observed but is insignificantly slow, due to a longer metal-to-metal distance (19.5 Å $Cu_A$ - heme $a$; 21.8 Å $Cu_A$ - heme $a_3$) and a higher reorganization energy [30]. Heme $a$ can be considered as an electron-storage site because further transport to the BNC is strictly controlled by proton translocation to stabilize the reduced state of heme $a_3$ [31]. Subsequent electron transfer from heme $a$ to the BNC is significantly fast due to its spatial location and close arrangement (13.2 Å meta-to-metal, 4.7 Å edge-to-edge). Quantum-chemical and molecular dynamic calculations studies demonstrated that there is no need for an single explicit

electron transfer route between both hemes as neighboring donor and acceptor atoms are equally contributing to the electron transfer process [32].

### 1.4.2 Proton transfer pathways

The required protons for dioxygen reduction in A-type HCOs are taken up by two water-filled proton transfer routes, denoted as the D- and K-pathway. Both pathways have been investigated by a combination of structural and site-directed mutagenesis studies for the bacterial C*c*O [9, 33]. For the bovine enzyme, an additional third proton pathway, the H-pathway, has been postulated, in contradiction to the two previous ones and is not conserved. Thus, this H-pathway is still under debate and is not yet fully accepted as a proton-pump system in the field of C*c*O studies. The following sequence numbers refer to those of the subunits from *Paracoccus denitrificans* cytochrome *c* oxidase.

The longer D-pathway starts at $Asp^{124.I}$ (“D”) and includes several conserved polar residues as $Asn^{131.I}$, $Ser^{134.I}$, $Tyr^{35.I}$, $Ser^{192.I}$, $Ser^{193.I}$, $Ser^{189.I}$ and $Glu^{278.I}$ (Fig.1.5). Numerous site-directed mutation studies of $Glu^{278.I}$ have demonstrated an eminent impact on the activity of bacterial C*c*O, showing no effect or even increased effect on turnover rates but an abrogated proton-pumping function, underlining its crucial role in proton translocation and coupled dioxygen reduction [34, 35]. Along this pathway, several water molecules can be seen in the oxidized structure and appear to form a connecting wire towards both hemes and a water-filled cavity which is considered as the proton-loading site (PLS). It is commonly believed that his water-filled cavity is necessary to deliver required chemical protons for subsequent water formation which could serve as a “continues refill” for the PLS under turnover conditions [20]. Without its existence, it becomes incomprehensible how protons should be transferred from $Glu^{278.I}$ to the binuclear center as their spatial locations are rather distant to each other (~12 Å). In this context, it should be noted that free energy calculations have shown that $Asp^{124.I}$, the entry point for the D-pathway, appears to gate and regulate the channel by isomerization [36].

The K-pathway, shorter than the D-pathway, leads to the binuclear center starting from the highly conserved $Lys^{354.I}$ (“K”) via $Ser^{291.I}$ and $Thr^{351.I}$ to the cross-linked $Tyr^{280.I}$.

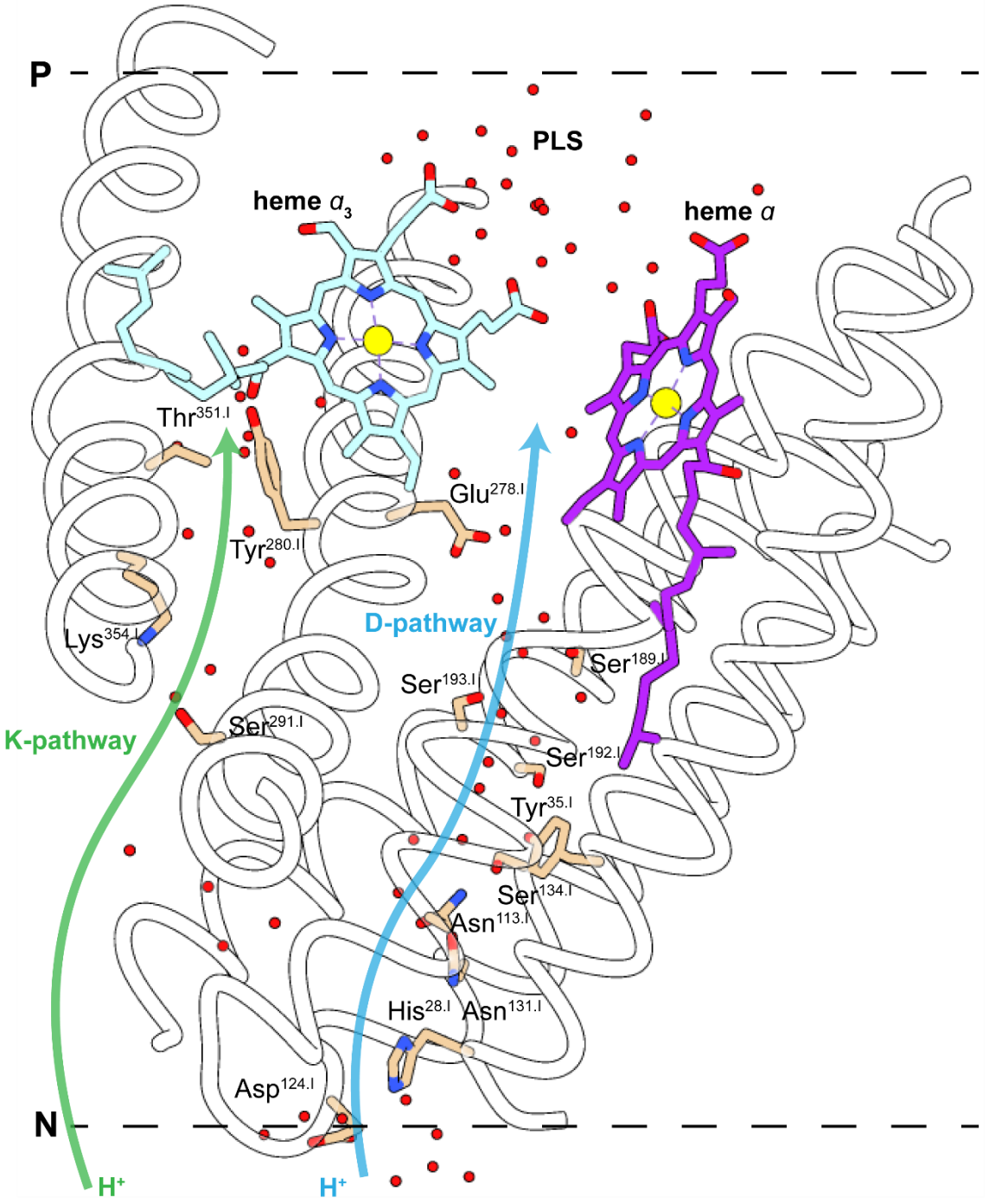


**Figure 1.5**. **Proton transfer pathways in *P. denitrificans* cytochrome *c* oxidase**. Transmembrane helices are shown in white and water molecules as red spheres. The D-pathway originates at Asp$^{124.I}$ and leads via several polar residues to Glu$^{278.I}$ (light blue). The K-pathway starts at Lys$^{354.I}$ and consists of three polar residues (green). In-between both hemes and pointing to the P-side, a water filled cavity is present, the proton-loading site (PLS). The figure was prepared by using Chimera.

These residues are located in the transmembrane helices VI and VIII (Fig.1.5). The involvement of the hydroxyl group of the heme $a_3$ hydroxyethylfarnesyl chain in proton translocation is presumed. Mutating the key-residue $Lys^{354.I}$ showed no major effect on the oxidative phase of the catalytic cycle but proved to inhibit the consequent reduction of the BNC. Derived from numerous site-directed mutagenesis studies, it has been deduced that the K-pathway is responsible for conducting the chemical protons of the reductive phase of the catalytic cycle, where the reduction of the ferric/cupric binuclear site takes place [37, 38].

### 1.5 Catalytic cycle intermediates

The sequence of different oxygen intermediate states in the catalytic cycle of cytochrome *c* oxidase is considered to be a complex mechanism and is still the subject of many ongoing studies. Even though, the first structure of C*c*O was published in the 1990s, numerous aspects of dioxygen reduction remain unclear. Most of the oxygen species generated at the binuclear center under turnover conditions have been identified via resonance Raman and optical spectroscopy. Additionally, highly sophisticated computational assisted calculation methods have contributed significant insight into the complex mechanism (for reviews, see Michel *et al.*, 1999 [39]; Kaila *et al*., 2010 [20]). Related kinetics of intermediates were mainly investigated by flow-flash techniques which is still a common technique, using differently reduced forms of the C*c*O.

Beginning from the fully oxidized binuclear center (**O** state) in the reductive phase (**O→E→R**), the first resulting intermediate is the one-electron reduced form (**E** state) (Fig.1.6). In early studies, it was demonstrated that the arriving electron is transiently located between the $Cu_A$, heme $a$ and the binuclear center, implying a rapid equilibrium between the redox centers [40, 41]. Based on spectroscopic and electric measurements, it is assumed that there is a larger fraction of reduced heme $a$ [27]. Arrival of a second electron turns the binuclear center into the mixed-valence reduced form (**R** state) whereby it receives the ability to bind dioxygen for consequent redox chemistry. As the initial binding rate was shown not to be proportional to $[O_2]$ but to saturate at high oxygen concentrations, transient ligation of dioxygen to another site

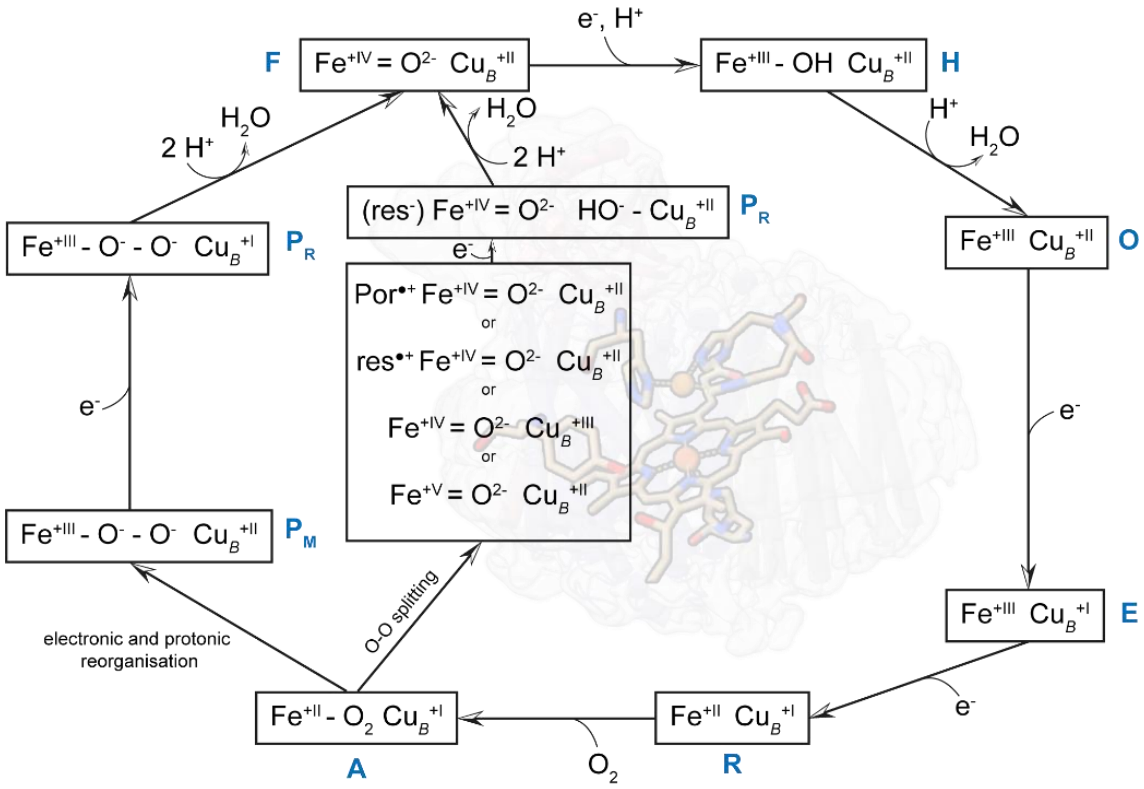


**Fig. 1.6 Detailed overview of the oxygen intermediates in the catalytic cycle of cytochrome *c* oxidase**. As the chemical composition of the **P** state remains unsettled, alternative proposed structures are presented (split dioxygen bond right, intact bond left). Por• and res• denote radicals of the porphyrin ring and an amino acid residue. Context is explained in the text.

prior to binding to the heme has been suggested, presumably to the copper atom [42, 43]. Since the dioxygen binding is of transient nature, the interaction between $O_2$ and $Cu_B$ was shown to be rather weak ($K_d$ = 8 mM) with a second-order forward rate constant of 3.5 x $10^8$ $M^{-1}$ $s^{-1}$ [42, 44].

Upon dioxygen binding, the oxidative phase of the catalytic cycle is initiated by forming the ferrous-oxy species which is traditionally termed compound **A** [45]. Compound **A** is characterized by an increase in absorbance (relative to the non-substrate bound enzyme) at 595 nm and 430 nm and time-resolved resonance Raman studies demonstrated a shift of the v(Fe-$O_2$) stretching mode from 572 $cm^{-1}$ to 546 $cm^{-1}$ by using $^{18}O^2$ [46-48]. The corresponding dissociation constant was determined to be 0.28 mM, resulting in an off rate of almost 40,000 $s^{-1}$ [49]. The formed heme-oxygen adduct is reminiscent of corresponding oxygen species found in structures of oxyhemoglobin or oxymyoglobin. Upon binding of molecular oxygen to the reduced BNC (~ 10 µs at 300 K and 1 mM $O_2$), splitting of the O-O bond occurs within ~25 µs (depending on the source of C*c*O) [50]. The decay of this oxygen species occurs via

the so-called **P** state which is characterized by an absorbance band at 607 nm with a red-shift of the Soret band to 428 nm and was originally postulated to be a ferric/cupric/**p**eroxy intermediate. As a first step, electronic reorganization forms a species denoted as $\mathbf{P_M}$ which is obtained in the reaction of the **m**ixed-valence enzyme with oxygen in the absence of additional electron donors with a rate of approximately 5 x $10^3$ $s^{-1}$ [29, 51, 52]. $\mathbf{P_M}$ has been associated with a signal in the resonance Raman spectrum at 803 $cm^{-1}$ that shifts to 769 $cm^{-1}$ when the reaction is initiated by $^{18}O_2$. Hence, the structural composition of the BNC was assigned to a ferryl species [53]. However, the true structural composition of this state, which is at redox level two electrons above the oxidized enzyme, remains elusive and the aforementioned Raman modes have not been observed in cytochrome $bo_3$ despite the oxygen intermediates being identical in both terminal oxidases ($aa_3$/$bo_3$) [54, 55]. Additionally, the α-band (607 nm, **P** minus **O**) of the absorption spectrum of fully-reduced enzyme ($\mathbf{P_R}$) is very similar to the one of the $\mathbf{P_M}$ state, although $\mathbf{P_R}$ is at a redox level one electron above $\mathbf{P_M}$. For the scenario of a residing oxoferryl species at the BNC as suggested by Kitagawa *et al*., the dioxygen bond is already broken at this stage of the dioxygen reduction cycle [56]. However, when assuming a $Fe^{4+}$=O structure for the $\mathbf{P_M}$, an additional electron must be provided from a nearby source as four electrons in total are required for dioxygen reduction. As known, three electrons can be provided by the metal centers ($Fe^{2+}$→$Fe^{4+}$, $Cu_B^{+}$→ $Cu_B^{2+}$), hence the required fourth electron has to be delivered by a non-metal source. Based upon this information, different chemical structures, as $Fe^{5+}$, $Cu_B^{3+}$ or $Fe^{4+}$=O / $Cu_B^{2+}$ with an additional either porphyrin or protein radical or a $Tyr^{280}$-radical formed upon cleavage of the O-O bond have been suggested [57-60].

Input of a third electron to the binuclear center produces the $\mathbf{P_R}$ state which can be observed in the reaction of the reduced enzyme with oxygen. Its formation occurs with a rate of 3 x $10^4$ $s^{-1}$ from compound **A** [29]. This fast phase has been attributed to electron transfer from heme $a$ to the BNC, highlighting that this electron transfer reaction is responsible for trapping the substrate within the active site [23, 49, 61]. As the optical characteristics of $\mathbf{P_M}$ and $\mathbf{P_R}$ appear to be similar, the latter shows a unique EPR signal from cupric $Cu_B$, presenting a potential fourth oxygenous copper ligand [62]. Thus, the most likely structure of the BNC for the $\mathbf{P_R}$ state would consist of a ferryl heme ($Fe^{4+}$=$O^{2-}$) and a hydroxide ion bound to $Cu_B$ ( $Cu_B^{2+}$-$HO^-$).

In a next step, no further electron is delivered to the active site for the formation of the ferryl-cupric **F** state. The rate of the consecutive step **P→F** during the turnover of reduced C*c*O with dioxygen is listed with ~ 100 µs [49]. However, the time for this transition varies strongly depending on the source of enzyme. The **F** state species is characterized by a difference absorption band at 580 nm (**F** minus **O**) and a $\nu(Fe^{4+}=O)$ mode at 785 $cm^{-1}$ in the resonance Raman spectrum [61, 63, 64]. Commonly, there are three different approaches to generate the **F** state, either by one-electron oxidation of the binuclear center in reversed $O_2$-reduction, input of three electrons to the enzyme and further mixing with molecular oxygen or excessive addition of hydrogen peroxide to the oxidized enzyme [58, 65, 66]. It is difficult to interpret the optical differences for the $\mathbf{P_R}$ state (607 nm) and **F** state (580 nm) assuming an oxoferryl structure for both intermediates [67]. Nevertheless, early studies have shown a successful transition of a 607 nm species to a 580 nm species (denoted as **F'** form) by pH decrease (8 to 6) without further additional electron input. Hence, it appears to be logical that both intermediates share a common structural composition at the active site [68]. Optical spectroscopic discrepancies can be explained by an altered ligand environment of $Cu_B$ with an additional proton that forms a water molecule as the fourth ligand instead of a hydroxide ion. Such an aquo ligand bound to the copper could offer a hydrogen bond to the oxo ligand of the ferryl heme, changing the axial symmetry of the heme which could result in a modified α-band spectrum as pointed out previously [20]. Ligand-mimicking studies have brought evidence for this assumption, however, it remains questionable if a process like that could cause such an impact on the spectral properties and is therefore still under debate [69].

After uptake of the last electron which is forwarded to the binuclear center, the decay of the **F** state into the **O** state occurs via a transient state, denoted as **H** state, where a distal hydroxide ligand resides next to the ferric heme producing a Raman signal at 450 $cm^{-1}$ [70]. Final uptake of an additional proton leads to the regeneration of **O** state, completing the oxygen reduction cycle.

### 1.6 Bridging ligands in the binuclear site

Due to the magnetically coupled nature of the ferric heme $a_3$ and the cupric $Cu_B$ in the oxidized enzyme, paramagnetic EPR signatures are quenched and precise structural determination of bridging ligands has been challenging. As already outlined for the active site of the fully oxidized state of the C*c*O, a negatively charged bridging ligand is required to prevent electrostatic repulsion between positively charged metal ions [60]. High-resolution X-ray structures of bovine and bacterial C*c*O have brought evidences for such occupancies [71, 72]. However, those observed densities are the subject of ongoing debates as the space within the binuclear center is very limited and spatial allocations of molecules are limited by geometrical and steric constraints. Early studies have suggested two oxygenous ligands e.g. a hydroxide at $Cu_B$ and a water at heme iron. Recently determined structures of higher quality underlined the possible existence of a peroxide dianion in the **O** state. The majority of deposited structures provide only insight into the binuclear site of the **O** state. Therefore, the structural composition of the other intermediate states, namely **P** and **F** state, remain elusive to-date and an even recently published XFEL (X-ray free electron laser) bovine structure under turnover conditions has raised more questions than providing answers [73]. As highlighted previously, radical formation, originating either from $Tyr^{280.I}$ or the macrocycle of heme $a_3$, cannot sufficiently explain the apparent spectral differences between the **P** and **F** intermediates [60]. In this light, it becomes inevitable to determine precisely the chemical composition of the bridging ligands for the $\mathbf{P_M/P_R}$ and **F** state in order to fully understand the mechanism of dioxygen reduction.

Summarizing the previous sections, it is evident that even with such an enormous amount of data from uncountable experiments done in the past decades, the detailed molecular mechanism of dioxygen reduction occurring in the binuclear site of cytochrome *c* oxidase remains obscure. Even though the three-dimensional structure of this redox enzyme is mainly known and numerous functional studies have provided more details about the intermediate states, the structural composition of those states remain almost completely unknown due to the lack of high-resolution information at the binuclear center. Additionally, traditional structural techniques, such as

crystallography, are strongly limited as they require well-formed and reproducible crystals which is commonly known as a bottleneck. Furthermore, it is very challenging to stabilize those intermediates of interest over days which are required to form crystals of high quality.

### 1.7 Goal of this study

Single-particle electron cryo-microscopy (cryo-EM) provides a powerful method for solving the three-dimensional structures of biological macromolecules, especially for membrane proteins. Where X-ray crystallography is encountering limitations (e.g. reproducible crystal forming, higher protein concentrations), cryo-EM is an elegant way to bypass these issues. Due to ongoing technical progress in this field, it is possible to determine cryo-EM structures at resolutions that highlight atomic details [74]. Even more importantly, cryo-EM samples are prepared by rapid vitrification in liquid ethane directly from solution, therefore maintaining the macromolecules in their soluble states in comparison with a state in crystal packing constraint. These possibilities enable us to unravel protein structures in defined biochemical conditions in a close-to-native state by cryo-EM.

The primary goal of this work was to study the intermediate states (**O, R, $P_{CO}$, F**) belonging to the oxidative phase of dioxygen reduction catalyzed by the cytochrome *c* oxidase ($aa_3$) from *Paracoccus denitrificans* enabled by single particle cryo-EM. Even though, numerous structures of $aa_3$ C*c*O have been reported in the past, the majority of these structures represent either a fully oxidized or reduced state, no high-resolution cryo-EM structure is present to-date and only very few ones are trying to address the structural composition of the active site [69]. Based on that, the main interest of this project was to obtain a coherent structural data set of all four intermediate states. This was accomplished by applying given inhouse methods and protocols to generate stable intermediate species for subsequent three-dimensional structure determination by cryo-EM.

# 2. Materials and methods

## 2.1 Biochemical methods

### 2.1.1 Production of cytochrome *c* oxidase from rec. wild-type *P. denitrificans*

The cytochrome *c* oxidase ($aa_3$-type) from *Paracoccus denitrificans* was produced in *P. denitrificans* AO1 cells transformed with the pUB39 (pBBR1 MCS derivative) plasmid and RP-4 helper strain via triparental mating according to a standardized in-house protocol [75, 76]. A pre-culture was set up by adding 0.1 mL of 50% glycerol stock to 50 mL succinate (25 µg/mL kanamycin, 25 µg/mL streptomycin) growth medium. Cells were incubated at 32 °C while shaking (180 rpm) over night. An intermediate-culture was started by inoculating 500 mL succinate (25 µg/mL kanamycin, 25 µg/ml streptomycin) growth medium with 50 mL of the pre-culture. Subsequently, cell growth was carried out by adding 200 mL from the intermediate-culture to 2.5 L of cell media maintained at 32 °C and shaking with reduced speed (150 rpm) for approximately 8 hours. The cells were harvested by centrifugation (10,500x g at 4 °C, 15 minutes), and then the cell paste was disrupted using a high-pressure homogenizer (Constant System Ltd.) with an applied pressure of 25 kpsi. The cell lysate was centrifuged at 6,000x g at 4 °C for 60 minutes followed by an ultra-centrifugation step with a speed of 205,000x g at 4 °C for 12 h (Avanti J-26XP, Beckman Coulter, Brea, Ca, USA). Collected membrane pellets were resuspended in 50 mM KPi (pH 8) with an approximately concentration of 20 mg/mL.

### 2.1.2 Production and purification of the antibody-fragment from *E. coli* JM83

The antibody-fragment Fv7E2 was produced in *Escherichia coli* JM83 with the plasmid pASK68 ($Amp^r$) which possess the ability to bind to SU II of C*c*O and carries a C-terminal Strep-tag [77, 78]. Subsequent protein production was achieved by expressing the gene of interest after addition of IPTG. For production, a pre-culture was inoculated with a volume of 0.1 mL 50% glycerol stock and grown in 200 mL LB (100 µg/mL ampicillin) growth medium at 30 °C (180 rpm) overnight. The 200 mL pre-culture was expanded to a 2-liter main culture (100 µg/mL ampicillin) and grown at 23.5 °C while shaking (165 rpm) to an $OD_{600}$ (Ultrospec 2100 pro, Amersham Biosciences, UK) of 0.5 before recombinant antibody-fragment production was induced by the addition of 0.5 mM IPTG for additional 3 hours. Collected cell material was centrifuged at 3,500x g for 15 minutes at 4 °C and pellets were subsequently mixed with 500 mM sucrose, 35 mM KPi (pH 8) for 20 minutes on ice which led to the formation of spheroblasts due to osmotic shock. The disrupted cell lysate was centrifuged at 24,000x g at 4 °C for 60 minutes and the supernatant, containing the antibody-fragment, was collected and stored in 30 mL aliquots at -20 °C.

### 2.1.3 Purification of cytochrome *c* oxidase from rec. wild-type *P. denitrificans*

For preparation of the four-subunit cytochrome *c* oxidase, pelleted membranes were solubilized in 50 mM KPi, pH 8 using 5% (w/v) dodecyl-β-maltoside (DDM) while stirring. In a first step, solubilized C*c*O was incubated with the strep-tagged Fv antibody-fragment for 30 min at 4 °C while stirring to allow efficient binding. The final mixture was centrifuged at 325,000x g for 60 minutes at 4 °C and the supernatant was loaded on Strep-Tactin®XT Superflow® high capacity affinity column (IBA GmbH). For washing, 5 column volumes [CV] of buffer (50 mM KPi pH 8, 0.05% (w/v) DDM) was used and for the final elution (5 CV), the washing buffer was supplemented with 50 mM biotin. To increase sample homogeneity, ion exchange chromatography was

performed using a Q Sepharose® High Performance column (Sigma Aldrich). Washing was done by applying a salt gradient (50 mM/200 mM 0.05% (w/v) DDM, KPi pH 8) before eluting with 300 mM KPi (pH 8) and 0.05% (w/v) DDM. As a final sample polishing step, size exclusion chromatography was performed using a Superdex® 200 10/300 increase column (GE Healthcare Life Sciences) with a running buffer consisting of 50 mM KPi (pH 8) and 0.02% (w/v) DDM. To control the redox state of the purified cytochrome *c* oxidase, each protein batch was purified in the presence of $K_3[Fe(CN)_6]$.

### 2.1.4 Production and purification of MSP1D1

The production of the N-terminal 7x histidine tagged MSP1D1 (Membrane scaffold protein) was done according to a standardized protocol [79]. Therefore, BL21Gold (DE3) *E. coli* cells were transformed with the pMSP1D1 gene and grown in LB-Kan medium (50 µg/mL kanamycin) at 37 °C. Once reached an $OD_{600}$ of 0.6, induction with 1 mM of IPTG (final concentration) was carried out to start the MSP1D1 protein production for 4 h before cell harvest. The pellet from 4 L cell culture was resuspended in a cell disruption buffer (20 mM Tris-Cl pH 8, 1 mM PMSF) and afterwards supplemented with Triton X-100 (1% (v/v)). Mechanical disruption of cells was done by using a French Press cell disruptor (Thermo Scientific, St. Leon-Rot, Germany) with an applied pressure of 700-1000 psi. The resulting lysate was centrifuged at 104,000x g at 4 °C for 30 minutes and then filtered via a 0.22 µm pore filter. In a final step, the cell solution was supplemented with 500 mM of NaCl. For the subsequent purification procedure, the lysate was mixed with 6 mL Ni-NTA agarose which had been equilibrated with 10 CV of a washing buffer (20 mM Tris-Cl pH 8, 500 mM NaCl, 1% Triton X-100). The mixture was incubated for 12 hours while stirring at 4 °C. Next, the solution was loaded onto a column and washed with 7 CV of the aforementioned buffer. In a second washing step, 50 mM Na-cholate was used with 50 mM of imidazole. As a final elution step, 500 mM of imidazole was loaded and the eluted fractions were pooled and dialyzed against buffer (20 mM Tris-Cl pH 7.5, 150 mM NaCl) for 12 hours. The protein solution was concentrated to 4-5 mg/mL, frozen in liquid nitrogen and stored at -80 °C.

### 2.1.5 Lipid solubilization

To facilitate the assembling process of the purified membrane scaffold protein (MSP1D1) with the membrane protein (C*c*O), a phospholipid component, 1-palmitoyl-2-oleoyl-glycero-3-phosphocholine (POPC), is mixed with purified MSP1D1 in exact stochiometric amounts (see 2.1.7). To bring the lipid into solution, POPC was dissolved in chloroform to a concentration of 100 mM and subsequently dried to a thin film under vacuum conditions at 100 mbar near its phase transition temperature ($T_M$, 4-10 °C). For that, a Laborota 4001 Efficient rotary evaporator from Heidolph (Schwabach, Germany) was used in combination with a PC 301 vacuum pump from Vacuubrand (Wertheim, Germany). To fully remove remaining solvent, the lipid film was incubated under high vacuum conditions using the Chemistry-Hybrid-Pump RC 5 from Vacuubrand (Wertheim, Germany) for additional 8-12 hours. In a final step, the dried lipid film was brought into solution by using a Na-cholate buffer (20 mM Tris-Cl, 150 mM NaCl, 200 mM Na-cholate, pH 7.5) and aliquoted into 100 mM stocks. To increase the speed of solubilization, sonification, mixing and heating up to 60 °C was applied to the mixture.

### 2.1.6 Activation of Bio-Beads SM-2

Bio-Beads SM-2 from Bio-Rad (München, Germany) were activated by mixing with methanol following the manufactures directions and subsequently incubated and stirred at room temperature for 1 hour. This step was repeated three times. In a final step, the methanol was discarded and the remaining, activated Bio-Beads were washed with water at least 5 times. Activated Bio-Beads SM-2 were kept at 4 °C in water stored no longer than one week.

### 2.1.7 Reconstitution of cytochrome *c* oxidase in MSP1D1 and lipids

The reconstitution of cytochrome *c* oxidase into lipid nanodiscs was accomplished by using the aforementioned protocols [79]. Here, mixing the POPC, MSP1D1 and the membrane protein was done in a molar ratio of 500:10:1 and subsequently incubated at 4 °C for 1 h. Extensive detergent removal is obligatory and achieved by adding 0.2 mg dried, active Bio-Beads™ SM-2 (Bio-Rad) every 2 h keeping at 4 °C. For successful formation, the mixture was incubated for an additional 12 h while shaking at 4 °C three times. In a next step, the Bio-Beads were removed by filtration and the reconstituted C*c*O was applied to a Superdex® 200 10/300 increase column to separate the homogenous complex and remove empty nanodiscs using 50 mM KPi (pH 8) as final storage buffer. Fractions containing nanodiscs-reconstituted $aa_3$ oxidase were pooled together, concentrated to 2 mg/L and directly used for following cryo-EM studies.

### 2.1.8 SDS-polyacrylamide gel electrophoresis

Sodium dodecyl sulfate polyacrylamide gel electrophoresis (SDS-PAGE) is a widespread method in the field of molecular biology to separate and visualize proteins. The basic principle relies on separating molecules of different molecular weights facilitated by the individual electrophoretic mobility of each SDS denatured protein under the influence of an external electrical field. Binding of SDS leads to protein denaturation and a correlating negative charge per mass ratio by which proteins can be separated according to their molecular weight. The gel acts as a molecular sieving matrix and thereby the proteins migrate with different velocities according to their size.

To confirm the presence of all subunits of the cytochrome *c* oxidase, this was the method of choice. SDS-PAGE samples were prepared by mixing the protein with 4x NuPAGE® LDS sample buffer (106 mM Tris-Cl, 141 mM Tris Base, 2% LDS, 10% Glycerol, 0.51 mM EDTA, 0.22 SERVA®Blue G250, 0.175 mM Phenol Red, pH 8.5) from Invitrogen (Darmstadt, Germany) in a ratio of 1:4. Following separation of protein

subunits was performed on NuPAGE® 4-12% Bis-Tris polyacrylamide gels at 200 V for approximately 45 minutes with 1x NuPAGE® MES SDS running buffer (2.5 mM MES, 2.5 mM Tris Base, 0.005% SDS, 0.05 mM EDTA, pH 7.7) from Invitrogen. Electrophoretically separated proteins were stained by using PageBlue™ protein staining solution from Fermentas (St. Leon-Rot, Germany).

### 2.1.9 Native-polyacrylamide gel electrophoresis

In contrast to the SDS-gel electrophoresis, the native polyacrylamide gel electrophoresis is used to visualize macromolecules in their native shape without applying reducing agents or heat to the sample. While the basic principle of both methods can be considered to be similar, physiological conditions in a common native Bis-Tris gel system are less harsh and therefore this technique provides a higher resolution of the analyte's structure. Consequently, Native-PAGE can be used to study protein conformations or aggregation as they retain their folded conformation.

According to the manufacture's protocol, 4x CN-PAGE™ sample buffer (50 mM Bis-Tris, pH 7.0, 50 mM NaCl, 10% (v/v) glycerol, 0.01% (w/v) bromophenol blue) was mixed in a ratio of 1:4 with the protein. The 1x cathode buffer (50 mM Tricine, pH 7.0, 15 mM Bis-Tris, 0.05% (w/v) sodium deoxycholate, 0.01% (w/v) dodecyl-*β*-D-maltoside (DDM)) and the 1x anode buffer (50 mM Bis-Tris, pH 7.0) were prepared in sufficient volumes. The electrophoretic separation was done by using Novex® 4-16% Bis-Tris polyacrylamide gels in combination with a XCell SureLock® Mini-Cell (Invitrogen, Carlsbad, USA) at 150 V at room temperature for approximately 60 minutes and was continued at 4 °C at 250 V for 30 to 90 minutes. Separated proteins were stained with PageBlue™ protein staining solution from Thermo Fisher Scientific (St. Leon-Rot, Germany).

## 2.2 Biophysical methods

### 2.2.1 Uv/visible absorption spectroscopy

Determination of the protein concentration of purified CcO was done by using a Lambda 35 (Perkin Elmer, Waltham, USA) spectrophotometer. Uv/visible spectrophotometry is a quantitative measurement of the absorption/transmission or scattering of a material as a function of wavelength. Materials absorb light according to the Lambert-Beer-law ($A = \varepsilon c l$) where the A is the absorbance of light at a specific wavelength and the ε is the extinction coefficient which is an intrinsic descriptor of the molecular electronic state and is specific to the wavelength applied as well. Most protein absorbance measurements are done at 280 nm due to the strong absorbance by the aromatic amino acids at this wavelength. Here, the protein concentration was calculated using the extinction coefficient of $\varepsilon_{425\ nm}$ = 158 $mM^{-1}$ $cm^{-1}$; this extinction coefficient is related to the metal centers in the protein complex as these can be also used for measurements/determinations of different oxidation states [58]. A quartz-cuvette (Hellma, Müllheim, Germany) with a path length of 1 cm was used and filled up with approximately 7 µM CcO in 50 mM KPi, pH 8.0, 0.02% (w/v) DDM. The spectrum was recorded in the range of 380 nm to 700 nm with a scan rate of 400 nm/min and a split bandwidth of 2.0.

Apart from protein determination, uv/visible absorption spectroscopy was used to determine different intermediate states of the binuclear center of C*c*O. The fully oxidized state (**O** state) was obtained by incubating the membrane protein in the presence of 200 µM potassium ferrocyanide at 4° C overnight. The potassium ferricyanide was then removed by gently washing the protein several times in an amicon concentrator (Milipore, Bellerica, USA) with the standardized buffer. For the fully reduced state (**R** state), 8.3 mM of sodium dithionite (DT) was added to the protein solution without the need of an incubation time as the reduction of the metal cofactors occurs instantly. For the peroxy state (**P** state), the protein solution was pipetted into a glass vial, sealed with a rubber seal and the headspace was flushed with gaseous carbon monoxide for approximately 10 minutes to create the two-electron $\mathbf{P_{CO}}$ state.

Special care was taken here as too intensive incubation time can lead to a three-electron state (**$P_R$/F**). The ferryl state (**F** state) was induced by using 500 molar equivalents of hydrogen peroxide (Hydrogen peroxide 30%, Merck, Darmstadt, Germany) to achieve a high population of the three-electron intermediate state. The concentration of hydrogen peroxide was determined measuring the absorption at 240 nm with an extinction coefficient of $\varepsilon_{240\,nm} = 40\ M^{-1}\ cm^{-1}$.

For Cryo-EM studies, the protein stock solution where the aliquot was taken from was kept under constant conditions (e.g. carbon monoxide atmosphere for **P** state generation) and was spectroscopically verified prior and after vitrification processes. From sample adjustment to freezing in liquid ethane, no more than 10 minutes were used to avoid potential decay processes.

### 2.2.2 Oxygen reductase activity measurement

The oxygen consumption of C*c*O was measured using a Clark-type oxygen electrode (OX-MR-Electrode) linked to a multimeter PA 2000 (Unisense A/S, Aarhus, Denmark) at 20 °C. The working principle of the oxygen electrode is based on diffusion of molecular oxygen through a silicone membrane to an oxygen reducing cathode. The reducing cathode is polarized against an internal Ag/AgCl anode. Generated signals were recorded via an A/D converter and the micro trace basic software (Unisense A/S, Aarhus, Denmark). Cytochrome *c* (Biomol, Hamburg, Germany) was reduced by sodium dithionite and subsequently washed to remove excess of the salt using a PD-10 column (Amersham, Biosciences, UK). Next, the concentration was determined via uv/visible absorption spectroscopy by recording the redox-spectra of cytochrome *c.* For this, the fully oxidized spectrum was obtained in the presence of 1 mM potassium ferricyanide. The concentration of reduced cytochrome *c* was calculated using the Lambert-Beer law with an extinction coefficient of $\varepsilon_{redox550\,nm} = 18.7\ mM^{-1}\ cm^{-1}$ [80]. Oxygen reductase activity measurements were performed under stirring conditions in 2 mL glass vials with a sample volume of 600 µl. The vials remained open during activity measurements because oxygen consumption or production rate is considered to be fast enough to neglect diffusion processes of molecular oxygen related to the measuring buffer.

The electrode was polarized for approximately 24 hours prior to use at -0.8 V. For zero oxygen calibration, a solution consisting of 0.1 M NaOH and 0.1 M sodium ascorbate was used. The air saturated measuring buffer with the same temperature was used as a second calibration point (100% saturation). Influencing factors for oxygen concentration calculation as temperature or salinity were considered according to the manufacture protocol. The activity of solubilized C*c*O was measured in 50 mM KPi pH 8.0, 0.02% (w/v) DDM, 0.3 mM tetramethylphenylene-diamine (TMPD), 3 mM sodium ascorbate and 40 µM of reduced cytochrome *c*. As a final step, 5 nmol of C*c*O was added to initiate the turnover reaction. Obtained raw data were analyzed and the oxygen turnover rate was calculated using Origin 2020 (OriginLab Corporation, Northampton, MA, USA).

### 2.2.3 Cryo-electron microscopy of membrane proteins

Structure determination of biological molecules is a very important aspect for a detailed understanding of biological processes. In the past decades, multiple methods with different physical principles were developed and applied to gain structural insights. X-ray crystallography, NMR spectroscopy, cryo-electron microscopy (cryo-EM), X-ray solution scattering, neutron diffraction, and various spectroscopic techniques provide structural biologists a broad set of methods. Excitingly, cryo-EM has gained more and more attraction in the past years due to dramatical technical advancement and is becoming to revolutionize the field of structural biology, commonly referred to as the "resolution revolution" [81]. One of the major bottle necks for X-ray crystallography is the production of reproducible, diffracting, well-ordered crystals which is a critical obstacle, especially for membrane proteins. In contrast to X-ray crystallography, cryo-EM uses high energy electrons which travel through very

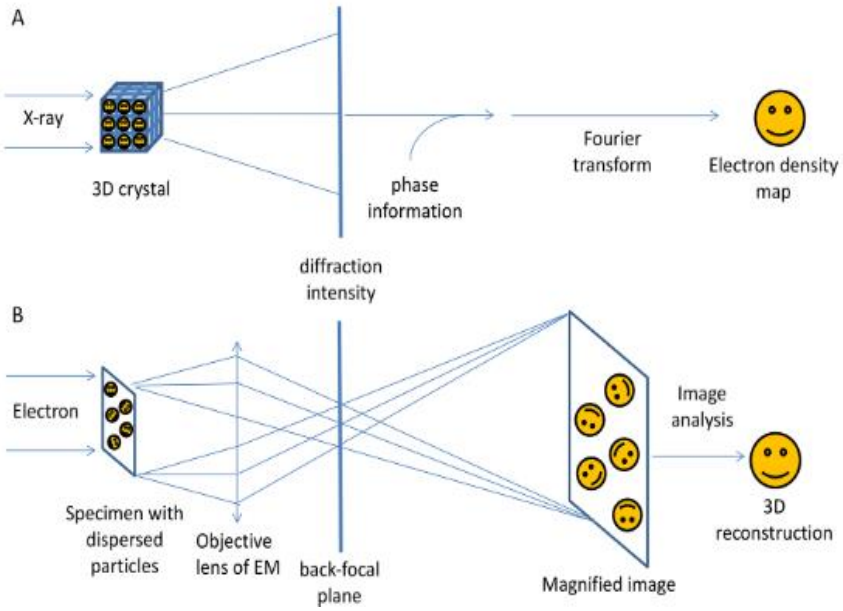


**Fig. 2.1. Technical difference between X-ray crystallography and single particle cryo-EM. (A)** Shows the physics and mathematical principles of X-ray crystallography to solve a structure of a specimen. Because of the lack of focus lens for X-rays, only intensities can be recorded and phases ("Phase problem") are lost. **(B)** Shows the physics and mathematical principles of cryo-EM to solve the structure of a biological target. Individual molecules within the protein can be imaged directly due to the strong interaction between an electron and Coulomb potential of an atom. The obtained Coulomb map (density map) can then be used to reconstruct the structure of the protein. Figure and context were taken from Wang et al. [82].

thin vitrified specimens and takes advantage of the negatively charged electron's trajectory which is bended by a magnetic field to focus the electron beam passing through the sample. A magnetic objective lens is required to produce both the diffraction pattern of a specimen at the back-focal plane and the magnified image in the image plane (Fig 2.2). Due to the strong interaction between the electron coming from the beam and each atom's Coulomb potential, single molecules of the vitrified specimen can be visualized and the magnified image already includes the full structural information about the molecule of interest [82]. A major advantage of this technique is that non-crystalline structures can be determined while keeping the required amount of protein relatively low. In the case of single-particle cryo-EM, hundreds of thousands of particles are recorded as images and subsequently classified, aligned and used for final model reconstruction by intense computational calculations. Furthermore, the underlying principle of cryo-EM allows the user to keep the protein in its native state without any additional biological engineering as often required for crystallography. EM samples are typically made by fast freezing the biological sample in liquid nitrogen, thereby maintaining its native state and opening up the opportunity to determine the structure in a more close-to-native state.

### 2.2.4 Sample vitrification for Cryo-EM

Quantifoil R1.2/1.3 copper grids (Quantifoil Micro Tools GmbH, Großlöbichau, Germany) were firstly washed with chloroform under gentle stirring conditions at room temperature until remaining solvent was gone. Then, washed grids were glow discharged with a PELCO easiGlow device (Ted Pella, INC., Redding, CA, USA) at 15 mA for 45 seconds. This step was repeated twice. For each recorded data set, a volume of 4 µl with a concentration of 2 mg/mL was applied on the grid before plunge freezing in liquid ethane for cryofixation to avoid crystal formation. A Vitrobot IV device (Thermo Fisher Scientific) was used to vitrify the sample at 4° C, 100% humidity, and the blot force was set to 20. The blotting time was set to 4 seconds before plunge freezing.

### 2.2.5 Image recording

Images for each data set were recorded by using a Titan Krios G3 microscope (Thermo Fisher Scientific) operated at 300 kV. Coma and beam tilt correction along with other optical parameters were done by using the EPU software (Thermo Fisher Scientific). Additionally, an overview (Atlas) of all mounted grids in the autoloader was taken to determine whether vitrified grids are of sufficient quality for the following automated recording session. As a final step, selected grid squares and foil holes were selected for data acquisition and the acquisition template for each foil hole was defined. The data collection was conducted by operating in an electron counting mode with a Falcon III (Thermo Fisher Scientific) direct electron detector at a nominal magnification of x96,000, corresponding to a calibrated pixel size of 0.833 Å. An accumulated electron dose of 0.98 $e^-/Å^2$ per fraction was used for the 30 dose-fractionated frames (~ total dose 30 $e^-/Å^2$). Applied defocus values were set in a range from -0.5 to -2.5 µm.

### 2.2.6 Image processing

Collected data in MRC format were exclusively processed with RELION-3.1 and motion corrected with the MotionCor2 algorithm [83-85]. Initial CTF parameters from each dose-weighted image were determined using CTFFIND4 and particle images were automatically selected followed by initial model building, 3D classification, CTF refinement, Bayesian polishing and final map reconstruction using RELION-3.1 [86]. To reduce potential beam-induced damage of the specimen coming from the electron source, the last 15 frames per data set were excluded prior final map reconstruction. Unfiltered maps were sharpened by applying different *B*-factors (Debye-Waller factor) to allow simplified structural building and for visual improvement purposes. The final overall resolution was estimated by using the gold-standard Fourier shell correlation ($FSC_{0.143}$) which is commonly calculated from two independently refined data sets. Global resolution anisotropy was examined by RELION-3.1. This was consistently done for each recorded and processed data set. Significant map quality improvements

were achieved by applying a density-modification procedure to each data set in a consistent way as recently described [87].

### 2.2.7 Model building and geometry refinement

For building the correct four-subunit atomic model of the $aa_3$ C*c*O, the Protein Data Bank (PDB) submission by Harrenga and Michel (PDB 1QLE) was used as a template structure [88]. After manual backbone and side chain fitting in the respective map using Coot (Version 0.9.4.1), real-space refinement was conducted using Phenix (version 1.18) [89, 90]. Subsequently, density-modified maps were used for more precise molecule allocation in and around the binuclear center. Here, for reasons of modelling and comparison, a template structure, containing only the first two subunits of C*c*O, with a better resolution (2.25 Å) was taken from Koepke *et al.* (PDB 3HB3) [71]. Each build structure was individually validated by the MolProbity online server [91]. Summarized parameters and corresponding cryo-EM statistics are listed in the results chapter (see 3.6, table 3.1). For illustration purposes, models were visualized by using Chimera and ChimeraX [92, 93].

### 2.2.8 Visualization of oxygen channel

To reveal potential oxygen channels embedded in the first subunit of C*c*O leading towards the binuclear center, computational assisted calculations were done by using the Mole 2.5 online server [94]. For this reason, the **O** state structure was taken for calculations by applying follow settings - bottleneck radius: 1.5 Å, bottleneck tolerance 3 Å, origin radius 5 Å, surface cover radius 10 Å, max tunnel similarity 1. The oxygen channel proposed by Mole 2.5 was subsequently visualized with Chimera. Oxygen molecules were manually placed with Coot into corresponding densities observed in the **O** state density map. Based on the computational calculations, additional channels and cavities were suggested in proximity to the hemes. Each of them was carefully elucidated and could be sorted out as they did not meet the demanded parameters for transporting molecular oxygen. It should be noted that the van der Waals radius, the

steric size, of molecular oxygen is reported with 152 pm and therefore cannot traverse channels with a diameter smaller than 1.5 Å. Indicated cavities were assigned to solvent filled reservoirs.

# 3. Results

The goal of this study was to determine the three-dimensional structures of four intermediate states (**O, R, $P_{co}$, F**) of the prototypical cytochrome *c* oxidase from *Paracoccus denitrificans*. While the primary focus of this work was set on giving further understanding of the catalytic mechanism of the $aa_3$-type C*c*O, efforts were made to structurally characterize the oxygen conducting pathway towards the active site. For this purpose, single-particle electron cryomicroscopy was employed as the primary method of this work.

Results of this thesis are divided into three main sections:

(I) production, purification, and characterization of cytochrome *c* oxidase from *Paracoccus denitrificans* and subsequent reconstitution in lipid nanodiscs (MSP1D1) produced in *E. coli*.

(II) uv/visible absorption spectroscopy and oxygen reductase activity measurements to confirm the existence of each desired intermediate state and to verify the functional activity of the nanodisc reconstituted membrane protein complex.

(III) determination of four atomic structures of the cytochrome *c* oxidase by Cryo-EM including all essential steps of data collection, data processing, model building and validation of the resulting structures.

### 3.1 Purification of the membrane scaffold protein (MSP1D1)

The membrane scaffold protein was recombinantly produced in cells of the *E. coli* BL21-Gold (DE3) strain which contains an N-terminal 7x histidine tag followed by a TEV protease cleavage site. For the purpose of this work, a TEV protease digestion was not required. The purification was carried out by using Ni-IMAC as described in chapter 2.1.4. A final gel filtration step was done to verify the sample's homogeneity and the presence of all subunits were confirmed by SDS-PAGE analysis. As shown in figure 3.1A, the majority of impurities was removed from the Ni-NTA resin by stringent washing. The first washings steps with different types of detergents are required to remove residual *E. coli* lipids from the highly lipophilic His-MSP. Further washing by applying an imidazole gradient and subsequent elution with 500 mM imidazole showed a distinct band on the gel in the range of ~ 25 kDa which is in accordance with the molecular weight of MSP1D1 (~22.8 kDa). The protein containing fraction was applied onto a gel filtration column to remove smaller impurities and to change to a buffer without imidazole (Fig 3.1B). The purified protein showed sufficient quality for further use. Approximately 50 mg of His-MSP were obtained from 1 L of production culture.

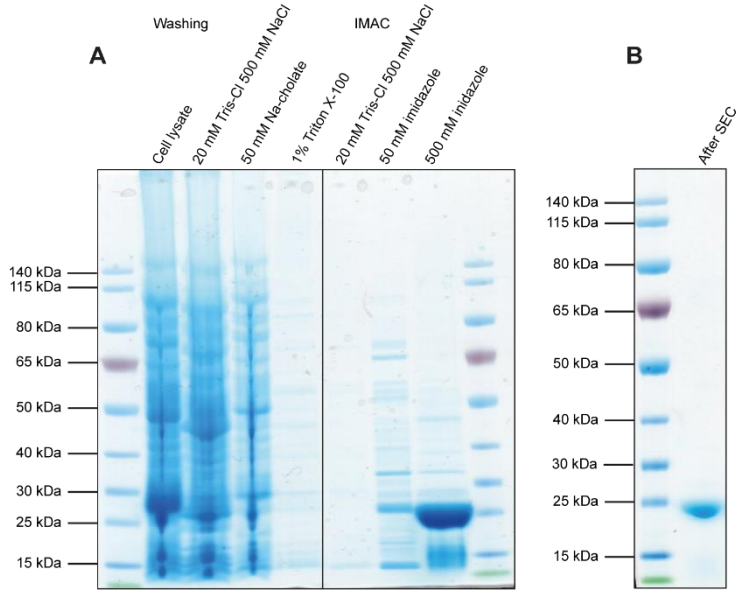


**Fig. 3.1. SDS-PAGE gels demonstrating Ni-IMAC purification of His-tagged MSP. (A)** SDS-PAGE gel of MSP purification fractions from Ni-IMAC. **(B)** SDS-PAGE gel of the purified protein after a gel filtration step.

## 3.2 Purification and characterization of the cytochrome *c* oxidase

### 3.2.1 Purification and reconstitution of the cytochrome *c* oxidase from *P. denitrificans*

The $aa_3$-type cytochrome *c* oxidase from *Paracoccus denitrificans* was recombinantly produced in the homologous host under microaerobic conditions. A previously established protocol was used and adapted in order to purify the untagged C*c*O as described in the chapter 2.1.1. The membrane fraction of the cells was isolated, solubilized and incubated with the recombinantly produced Fv-fragment from *E. coli* to facilitate the strep-tag affinity purification. To achieve the highest possible grade of sample purity and homogeneity, ion exchange chromatography and size-exclusion chromatography runs were performed. As the main goal of this work was to obtain structures from a membrane protein by cryo-EM, the use of detergent (DDM) was excluded and lipid nanodiscs were the method of choice for subsequent structure determination. To verify the successful reconstitution prior sample vitrification and to separate empty nanodiscs, an additional size exclusion chromatography step was included in the sample preparation workflow.

As presented in figure 3.2A, the membrane protein was already eluted in a relatively pure state prior to the ion exchange chromatography step. To further increase the purity, the collected fractions from the strep-purification step were significantly improved by applying a step-wise salt gradient. The eluted profile of the membrane protein from the IEC step exhibited already a high sample quality, however, a size-exclusion chromatography step was mandatory to determine which specific fractions contained the cytochrome *c* oxidase by measuring the intrinsic absorbance of the heme prosthetic groups at 420 nm (Fig. 3.2B). Here, the retention volume of the four-subunit cytochrome *c* oxidase with an attached Fv-fragment was approximately 12.5 mL. In a next step, an aliquot of the polished sample was used for reconstitution into lipid nanodiscs (MSP1D1). For separation of empty nanodiscs, an additional size-exclusion chromatography step was performed and the heme containing fractions (420 nm), which showed a monodisperse peak, were collected and pooled for

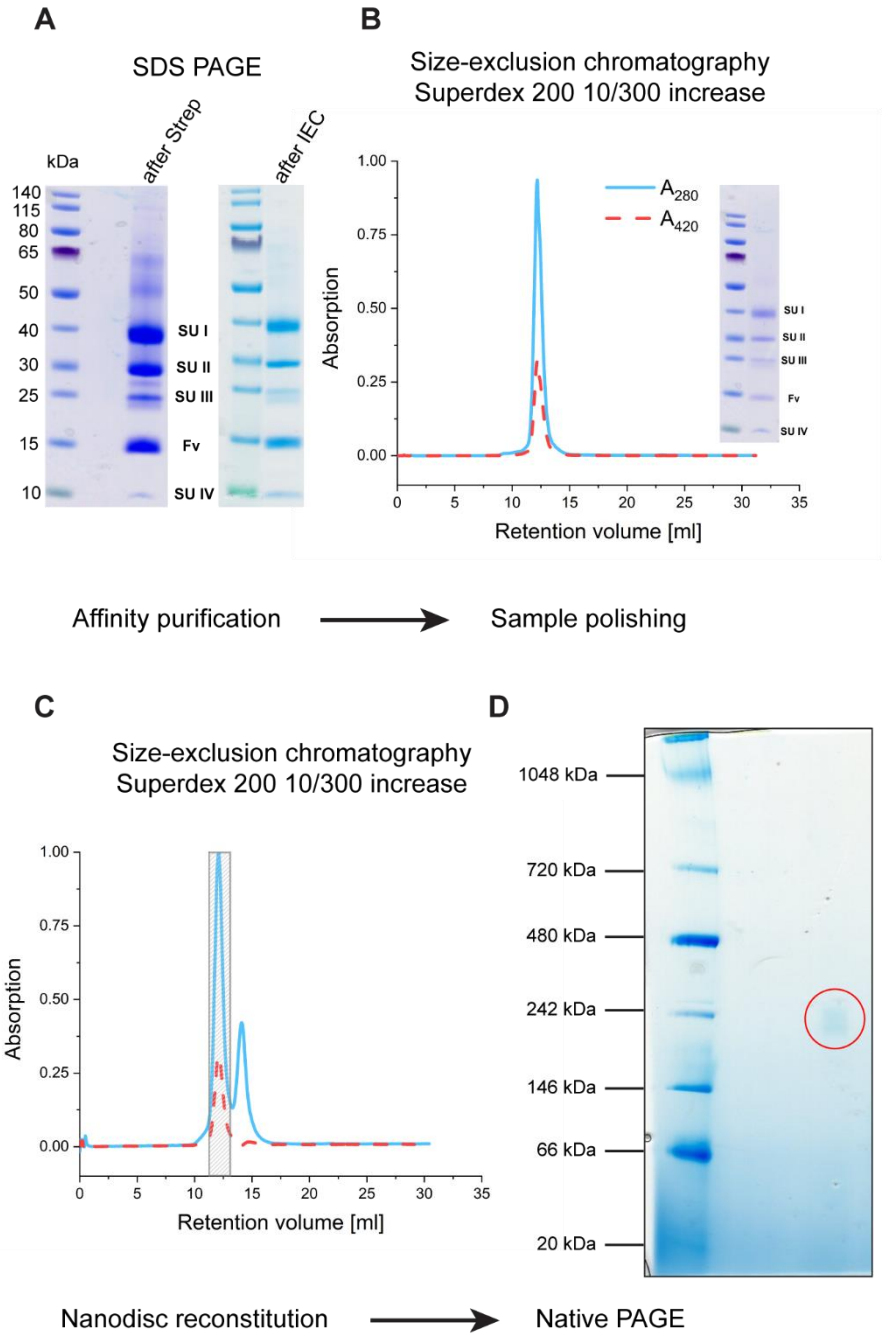


**Fig. 3.2. Gel filtration profiles and SDS PAGE gels demonstrating purification and reconstitution of cytochrome *c* oxidase from *Paracoccus denitrificans*. (A)** SDS-gels of applied affinity chromatography steps (strep-tag/IEC). **(B)** A size-exclusion chromatography step (280 nm – blue line; 420 nm – red line). As shown on the SDS-gel, all four subunits plus the attached Fv-fragment are present. **(C)** The purified protein was reconstituted into lipid nanodiscs and the protein containing fraction (grey) was pooled. **(D)** Native PAGE gel of the reconstituted, detergent-free reconstituted complex after SEC.

subsequent structural studies (Fig. 3.2C). As can be seen, the retention volume is slightly shifted to approximately 12.3 mL which appears to be reasonable as the reconstituted protein complex is larger (~200 kDa) in comparison to the non-reconstituted complex (154.2 kDa). In order to confirm the result of the sample

homogeneity analysis from the size-exclusion chromatography run, a native PAGE experiment was carried out (Fig.3.2D). Here, a distinct band in the range of ~ 200 kDa was observable which corresponds well to the size of the reconstituted membrane protein complex. Additionally, every final size-exclusion step was done in the presence of potassium ferricyanide as the as-isolated protein differed strongly from batch-to-batch in its electronation state.

### 3.2.2 Biophysical characterization of the cytochrome *c* oxidase from *P. denitrificans*

In order to assess if the purified cytochrome *c* oxidase was correctly assembled regarding the metal cofactors and exhibits an unaltered functionality when inserted in lipid nanodiscs, a biophysical characterization of the protein and the reconstituted complex was required

Therefore, the uv/visible absorption spectrum of a biochemical defined C*c*O sample was recorded, either in the fully oxidized or fully reduced state. The recorded spectra are in good agreement with literature data and indicating correctly incorporated heme cofactors [69]. Figure 3.3A shows the spectrum of the fully oxidized enzyme in comparison to the fully reduced one. As can be seen, a bathochrome shift of the Soret band from 425 nm to 448 nm occurs upon full reduction and is reversible (not shown) after treatment with an oxidizing agent (e.g. potassium ferricyanide). The visible α-

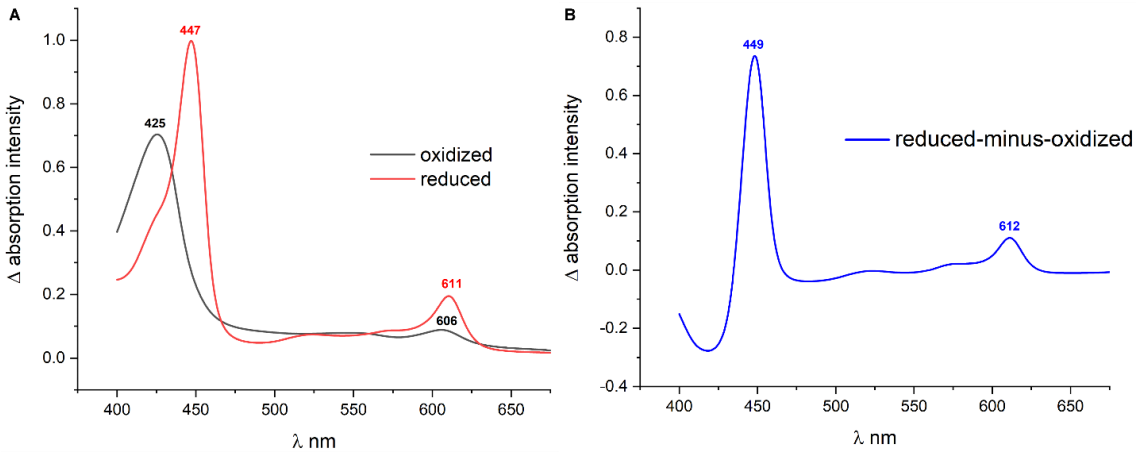


**Fig. 3.3. Absorbance spectra of purified cytochrome *c* oxidase. (A)** The uv/visible absorption spectra (375 nm – 675 nm) of the fully oxidized (black line) and fully reduced (red line) enzyme were recorded. **(B)** Corresponding reduced-minus-oxidized difference spectrum.

region indicates that the high-spin heme, belonging to the binuclear center, is predominantly oxidized and shifts from 606 nm to 611 nm accompanied by a hyperchromic effect. Fig 3.3B shows the corresponding redox spectrum. Based on these spectroscopic results, a correctly assembled protein complex was verified.

In a following step, the oxygen reductase activity was measured of the purified and assembled protein complex to verify its functionality. As all structural determination processes of the intermediate states were done in lipid nanodiscs, an unchanged enzyme activity of the reconstituted C*c*O had to be given. As shown in Figure 3.4A, a rapid decrease of oxygen concentration was observed upon addition of the protein and a turnover rate of approximately 371 $e^- \times s^{-1}$ was calculated which is consistent with previous measurements found in the literature (~ 400 $e^- \times s^{-1}$) [76]. A loss of roughly 5 % activity was observed when measuring the oxygen consumption rate of the reconstituted complex which can be neglected due to slightly different experimental conditions during sample preparation and substrate incubation (Fig. 3.4B). Moreover, the calculated turnover rate of approximately 352 $e^- \times s^{-1}$ indicates a full functionality of the reconstituted complex.

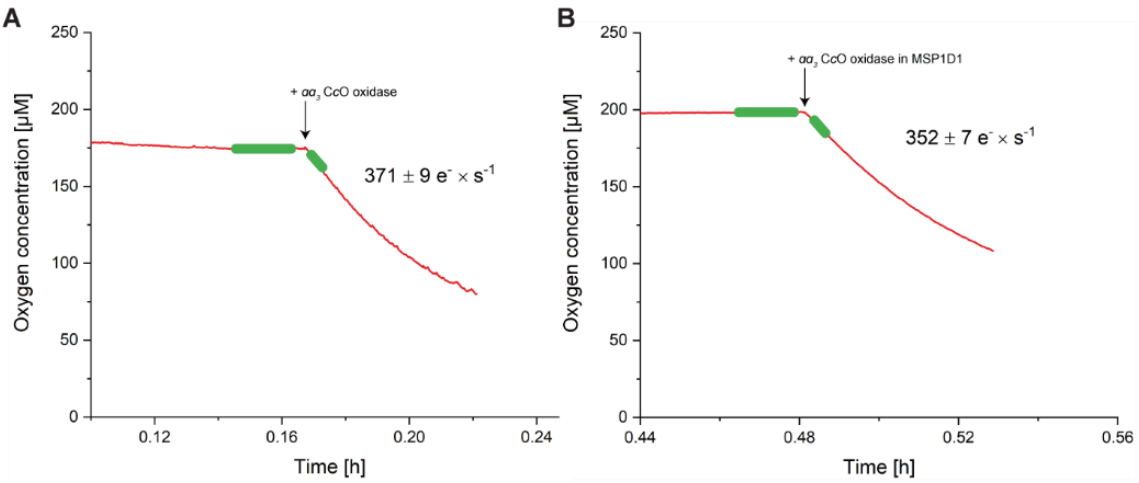


**Fig. 3.4. Oxygen reductase activity of cytochrome *c* oxidase. (A)** Indicates the oxygen consumption rate of the purified C*c*O in presence of cytochrome *c*. **(B)** Same conditions as for (A), but using the reconstituted C*c*O complex in MSP1D1. The activity assay presented in this work is based on the reduction of molecular oxygen measured by Clark-type oxygen electrode. The green traces before and after addition of the enzyme represents the slopes used for turnover calculations.

### 3.3 Characterization of the C*c*O intermediates by uv/visible absorption spectroscopy

As the main goal of this work was to visualize the chemical structure of the catalytic site of the cytochrome c oxidase in different redox states, the inducibility and stability of the intermediate states, especially the two ($\mathbf{P_{CO}}$) and three (**F**) electron intermediates, had to be characterized as the reconstituted samples were vitrified for cryo-EM. Hence, it was a crucial prerequisite to record the absorption spectra of the reconstituted sample in aqueous solution and to compare those spectra, in a second place, with ones from vitrified cryo-EM samples.

Figure 3.5 shows the spectrum of each relevant catalytic intermediate state in this work, the fully oxidized (**O**), the fully reduced (**R**), the peroxy (**P**) and the ferryl (**F**) intermediate. To illustrate the **P** and **F** state, the difference spectra are shown (induced-minus-oxidized). A maximum in the difference absorption spectrum typically for **P** state formation is located at 607 nm accompanied by a bathochromic shift of the Soret band (433 nm) in comparison to the oxidized form which is in accordance with the literature data [69]. The present gaseous carbon monoxide is oxidized by the C*c*O at the pH of 8 whereby two reduction equivalents are provided for a stable **P** state formation ($CO + 2OH^- \rightarrow 2e^- + CO_2 + H_2O$). As already outlined previously, this is considered to be a critical step as a too long exposure time of the sample (> 15 minutes) to carbon monoxide can lead to overreduction, resulting in a three-electron intermediate state ($\mathbf{P_R/F}$). Therefore, the generation procedure for the two-electron state had to be experimentally adjusted in numerous trials and was confirmed by a bathochromic shift of the Soret band of approximately 7 nm. For this procedure, the calculated maximum yield of $\mathbf{P_{CO}}$ state formation was around ~ 90 % [95]. Longer incubation time with carbon monoxide showed a comparable absorption maximum of the Soret band (~438-440 nm, not shown) as it is the case for the **F** state (438 nm). In this context it should be noted that all two-electron induced **P** states species, either formed by low molar level of hydrogen peroxide ($\mathbf{P_H}$) or gaseous carbon monoxide ($\mathbf{P_{CO}}$), share a very similar spectroscopic behavior.

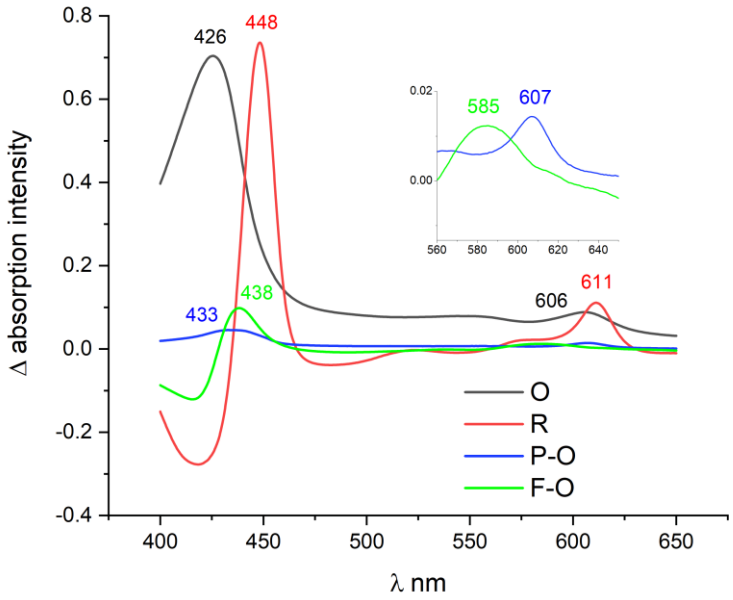


**Fig. 3.5. Absorbance and redox spectra of the reconstituted C*c*O complex.** The uv/visible absorption spectra (375 nm – 675 nm) of all intermediate states of interest. For the **P** (blue) and **F** (green) state, the induced-minus-oxidized difference spectra are indicated. Each intermediate was identified by its unique spectroscopic fingerprint.

Addition of 500-fold molar excess of hydrogen peroxide to the reconstituted, fully oxidized protein complex results in **F** state formation which is indicated by the disappearance of the 607 nm peak in the α-region and an appearance of an absorption maximum around 585 nm in the difference spectrum. Further evidence for the successful generation of the three-electron induced **F** state provides the red-shifted Soret band having its absorption maximum at 438 nm. As a molar excess of hydrogen peroxide is used, it is expected that the majority of present C*c*O molecules are converted into the **F** state at pH 8. Thus, the **F** state is considered as the most stable intermediate in the catalytic cycle as it progressively catalyzes the dismutation of $H_2O_2$ to water and oxygen.

Next, the established procedure for the intermediate generation was applied to each sample prior to vitrification and subsequent structure determination via Cryo-EM. Due to the fact that on-grid spectroscopic studies are not feasible to date unlike it is possible for protein crystals, the most promising approach was to record the uv/visible absorption spectra prior and after sample vitrification within shortest time for each prepared sample.

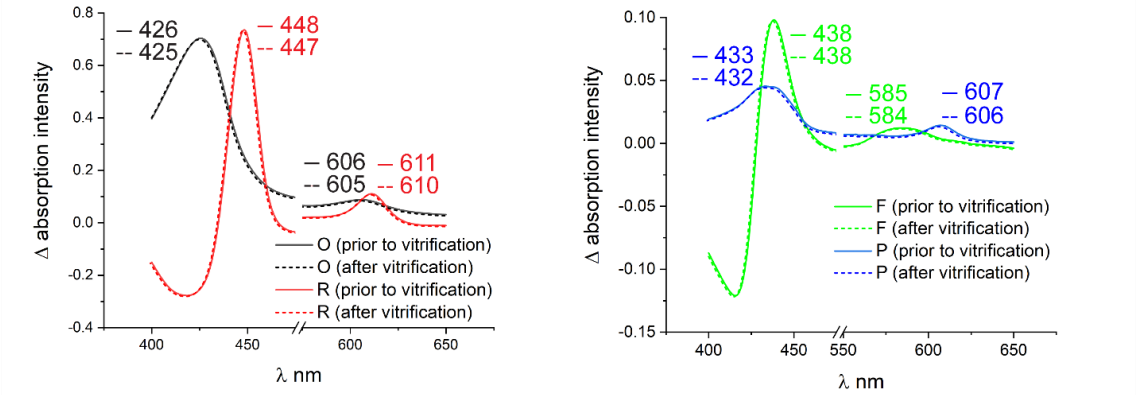


**Fig. 3.6. Recorded absorption spectra of the adjusted C*c*O complex prior and after sample vitrification.** Uv/visible absorption spectra (375 – 675 nm) of all intermediate states of interest. For the **P** (blue) and **F** (green) state, the induced-minus-oxidized difference spectra are shown. The solid line of each state shows the spectra prior the vitrification process while the dashed line represents the sample after the vitrification process.

As shown in Figure 3.6, the uv/visible absorption spectra unambiguously constitute and confirm the presence of the intermediate states of interest. Slight hypsochromic shifts (1-2 nm) can be seen but have no further meaning as a negligible oxidation process from sample adjustment to freezing was to be expected. Generally, those spectroscopic data underline the stability and robustness of the intermediates formed in the oxidative phase of the catalytic cycle in C*c*O. However, even if the obtained uv/visible spectra are of sufficient information for that novel approach in combination with Cryo-EM, a further confirmation giving method as Resonance Raman spectroscopy would be desirable.

### 3.4 Single-particle electron cryomicroscopy (cryo-EM)

Purified, characterized, adjusted and vitrified cytochrome *c* oxidase samples from *Paracoccus denitrificans* were used for conducting cryo-EM studies as described in section 2.2.5. Since the main objective of this work was to obtain a coherent data set of four intermediate states, it was of high importance to keep the image and data recording conditions as much consistent as possible during the entire process. The stated goal was to collect approximately 5,000 movies (corresponding to ~ 2,500.000 particles, 0.0833 Å pixel size) for each recording session as this amount of data was feasible to collect within an ordinary 72-hour cryo-EM session (Fig. 3.7). However, minor discrepancies regarding the amount of collected particles/movies between each recording session are existing for the reason of partly extended calibration time of the optical system resulting in reduced image recording time and less particles.

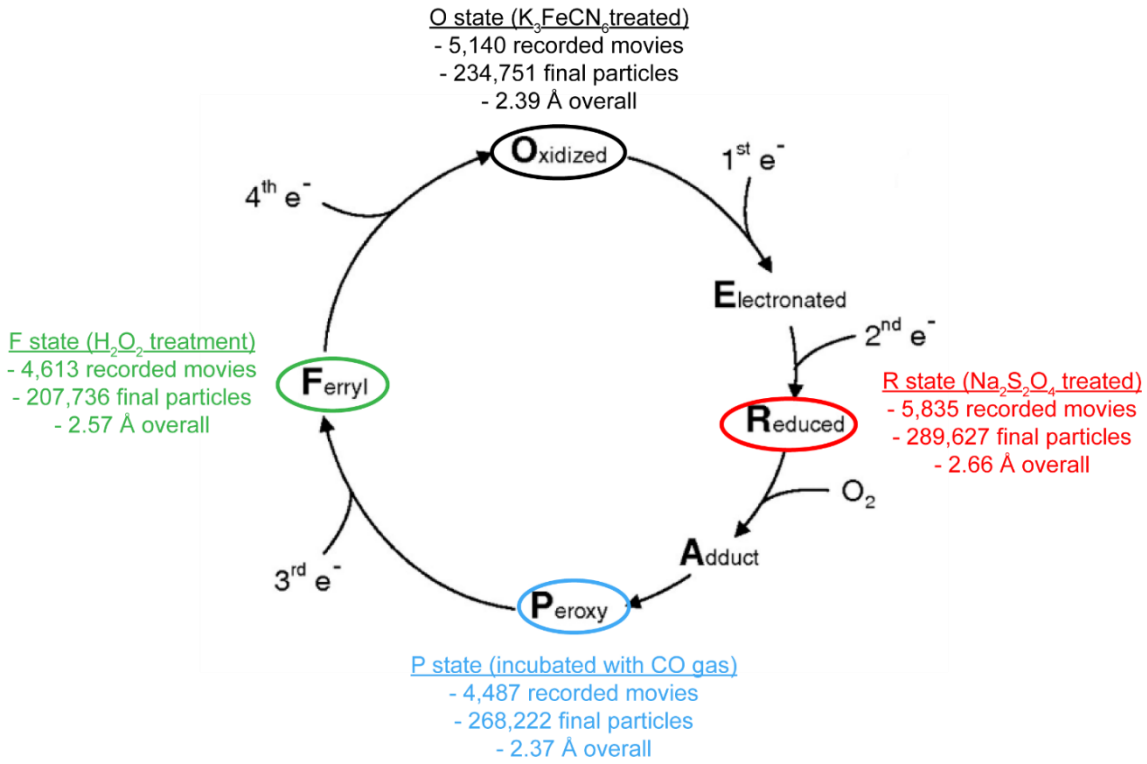


**Fig. 3.7. Image acquisition statistics for each recorded data set.** For each intermediate state, approximately 5,000 movies were collected with the Falcon 3 camera to obtain structures of high resolution (< 3 Å) and for reasons of comparability (~ 48 particles per movie per data set).

### 3.5 Image analysis and processing by RELION-3.1

As all recorded data sets were processed in a unified standard, the detailed image processing strategy, exemplarily shown for the **P** state data set, will be presented. For the **P** state session, 4,487 movies were collected and step-wise processed by using RELION-3.1. As a preliminary step, beam-induced motion correction was applied by using the implemented MotionCor2 algorithm and CTF parameters of each motion-corrected micrograph were estimated by CTFFIND-4.1 (Fig 3.8). Analyzing these obtained parameters are of great significance as they already provide valuable information about the accuracy of CTF determination, an important prerequisite for near-atomic 3D reconstruction. Therefore, it should be noted that the obtained cryo-EM image of a vitrified specimen is modulated by the contrast transfer function (CTF) and major factors that affect the quality of the CTF are the defocus and astigmatism of the operating lens. All micrographs were sorted out which had an estimated CTFMaxResolution of higher than 4.2 Å to increase the data set quality. This quality control step led to a reduced number of movies from 4,487 to 4,371. Next, a template-free auto-picking procedure based on Laplacian-of-Gaussian (LoG) filter was set and 2.313,196 particles were picked from 4,371 micrographs which corresponds to approximately 530 picked particles per micrograph (Fig. 3.9A). For the **O**, **R** and **F** state data set, comparable numbers of particles per micrograph were obtained. After successful particle extraction, which include the necessary metadata, 2D class

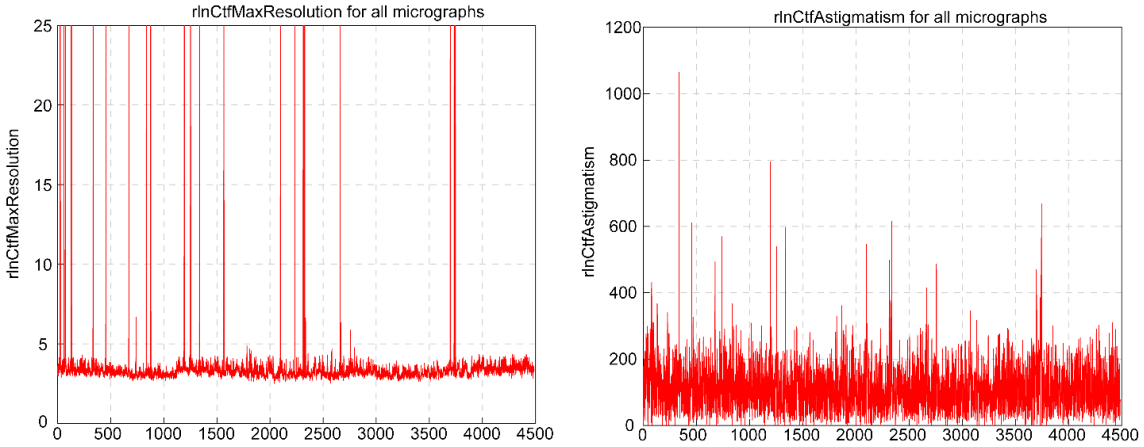


**Fig. 3.8. CTF parameter estimation by CTFFIND-4.1.** The estimated CtfMaxResolution value of each motion-corrected micrograph was in average smaller than 4 Å and showed average astigmatism values of ~ 200 Å.

averaging was performed (Fig 3.9B). In total, 43 two-dimensional classes were obtained (~ 375,589 particles) yielding distinct structural features and a sufficient distribution of viewing directions to facilitate the generation of a *de novo* 3D initial model from the 2D classes using a Stochastic Gradient Descent (SGD) algorithm [96]. Here, a randomized subset of 5,000 particles from selected 2D classes were used for the calculation of an initial reference model at ~ 15 Å resolution (Fig. 3.9C).

For further selection of high-quality particles, classification in three-dimensional space was performed. By using more classes in the parameter settings, it is rather likely that the data set will be divided into more subsets, potentially describing more variability and reducing the structural quality of the final reconstruction due to a reduced number of particles. As presented in Figure 3.9D, three major classes were obtained. The volume maps of these classes indicate that the particle set of only one class (red box) clearly represented the reconstructed map of the C*c*O comprising the majority of particles (~71.4 %) and provides already secondary structure information (e.g. transmembrane helices) at a resolution of 4.3 Å. Nonetheless, both other classes were carefully examined to exclude potential sub-species but were proven to be of no further significance.

A total number of 268,222 particles from the distinct C*c*O class were refined to high resolution in a fully automated manner. Thereby, the so-called *gold-standard* way is employed to calculate the Fourier Shell Correlation (FSC) from independently refined half-reconstructions in order to estimate the resolution more precisely [97]. Combined with a procedure to estimate the accuracy of the angular assignments, it automatically determines when a refinement has successfully converged. After the 3D auto-refinement, the map was sharpened which was done in a first step by creating a mask that defines the end of a protein and the beginning of the solvent region. The map and its corresponding mask were inspected in Chimera to confirm that the mask encapsulated the entire structure, but did not leave a lot of solvent inside the mask (Fig. 3.10) Subsequently, this mask was used for “post-processing” the density map consisting of 268,22 particles to sharpen the *B*-factors (Debye-Waller-factor) and to calculate the masked solvent-free FSC curves, resulting in a 2.84 Å map. Note that playing and changing the mask parameters (Soft-edge pixel number) were leading in some cases to improved FSC-based resolution estimations.

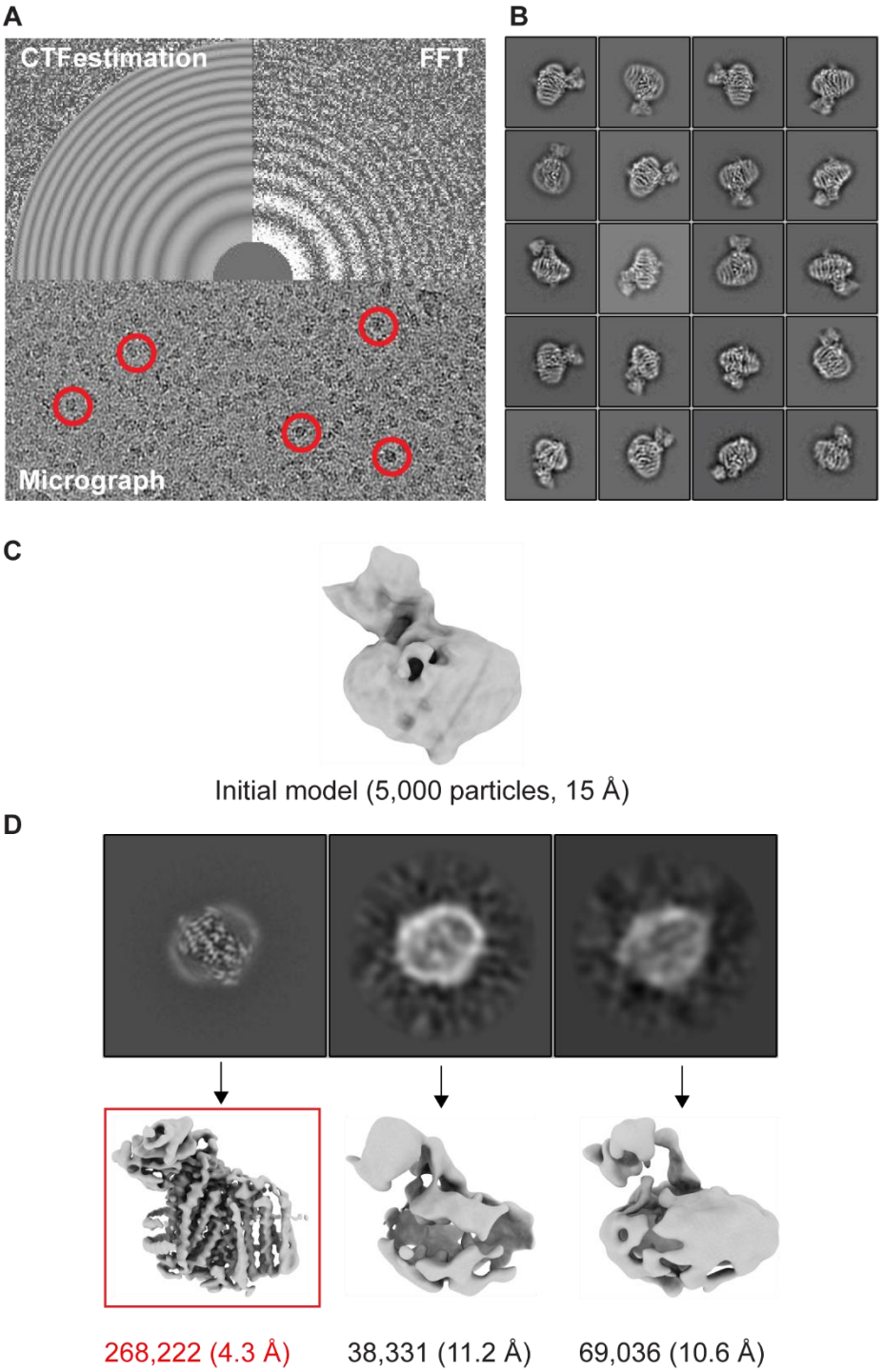


**Fig. 3.9. Autopicking of particles from motion-corrected micrographs for reference-free 2D class averaging and subsequent 3D classification (A)** Particles of each motion-corrected micrograph were template-free picked. Circular, well-defined thon rings (Power spectrum) were observed providing reliable information about the data quality. (**B**) 43 2D classes with defined structural features (e.g. attached Fv fragment) and an intact overall morphology were selected and taken for further 3D reconstruction calculations. (**C**) Selected 2D classes were used for the *de novo* 3D initial model calculation. (**D**) The first class (red box) represents the reconstruction of interest as it provides the highest quality. The density maps were visualized by Chimera.

To further improve the resolution of the reconstruction, “Bayesian polishing” was applied for per-particle, reference-based beam-induced motion correction. The goal of this calculation was to optimize a regularized likelihood that allows the user to associate with each hypothetical set of particle trajectories a prior likelihood that favors spatially coherent and temporally smooth motion without imposing any hard constraints [98]. First, a training with 20,000 particles of the reconstruction was carried out to estimate the process that yields the best motion tracks. Next, the obtained estimation results were taken to fit tracks for the motion of all particles and to produce adequately weighted averages of the aligned movie frames. Afterwards, the data of this polishing step were used for CTF and aberration refinements to estimate the asymmetrical and symmetrical aberrations in the motion-corrected particles. To confirm that the new particle file of those both steps gave better results, a re-run of 3D auto-refine and post-processing was conducted. In a final step, “Bayesian polishing” was performed with the purpose to exclude the last 15 frames which could potentially suffer from electron-beam induced damage. The final 3D model reconstruction of the cytochrome *c* oxidase showed an overall resolution of 2.37 Å (Fig. 3.11A) with even higher local resolutions (Fig. 3.11B), especially around the catalytic site. Unmasking the bound Fv fragment did not result in resolution improvement but a lower B-factor.

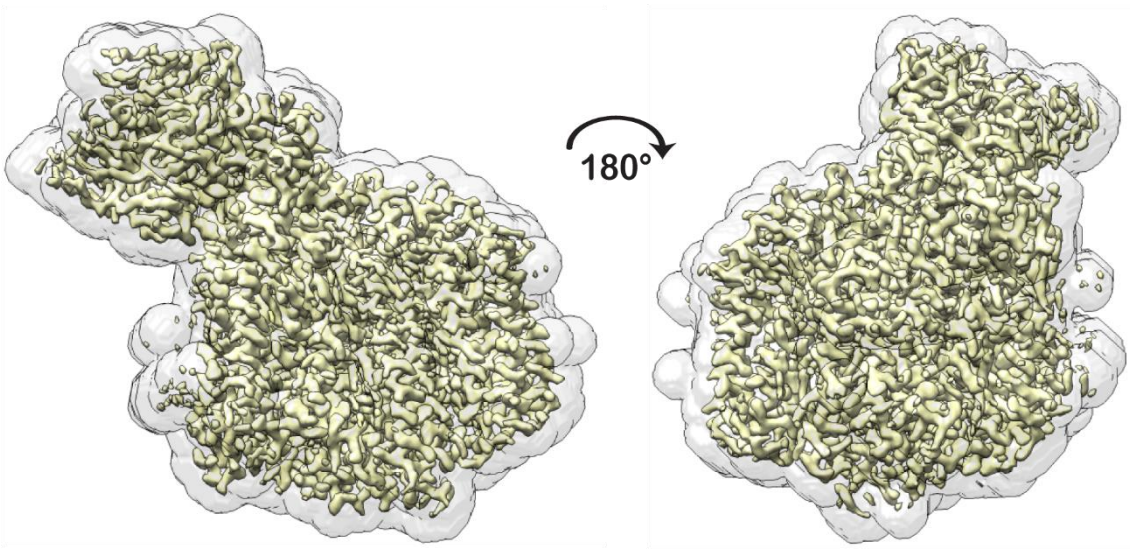


**Fig. 3.10. Masked 3D reconstruction after 3D auto-refinement.** As shown, the created mask (white) is covering the calculated density map (yellow) and mainly excluding the solvent region. Mask and map were visualized by Chimera.

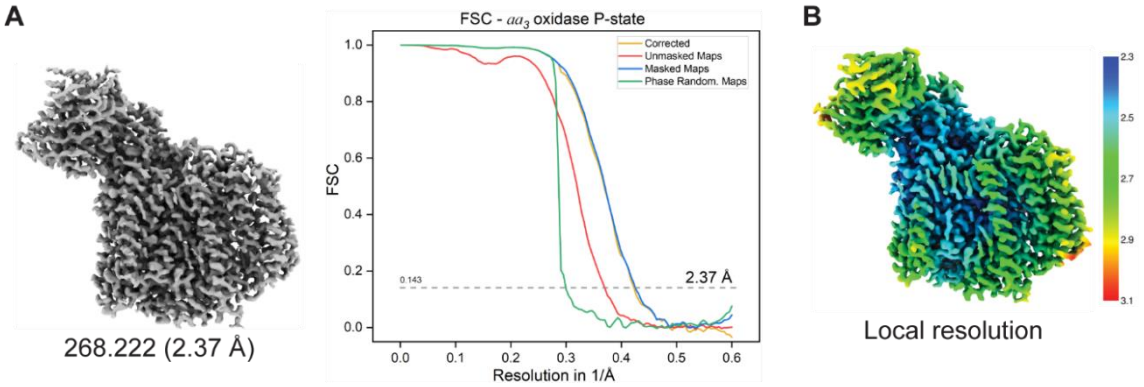


**Fig. 3.11. Final 3D reconstruction of the cytochrome *c* oxidase (P state).** (**A**) The final 3D map reconstruction yields 268,222 particles with an overall $FSC_{0.143}$ resolution of 2.37 Å. (**B**) Distinct higher resolution at local spots, especially within the first subunit including the catalytic site, can be observed. The density maps were visualized by Chimera.

### 3.5.1 Density modification

All obtained density maps from RELION-3.1 were improved in terms of resolution and map quality by applying a density-modification procedure implemented in Phenix (1.18). Shortly explained, this procedure is a standardized step in processing data from macromolecular crystallography to reduce the errors in the phases, which are rather poorly estimated, and thereby improve the resulting map. As described by Terwilliger *et al.*, a form of density modification can be applied during the process of image reconstruction in electron microscopy. The main difference here lies in the fact that cryo-EM maps do not suffer from lacking the phases and amplitudes which simplifies the reconstruction calculation. Yet, cryo-EM half-maps with errors that are nominally

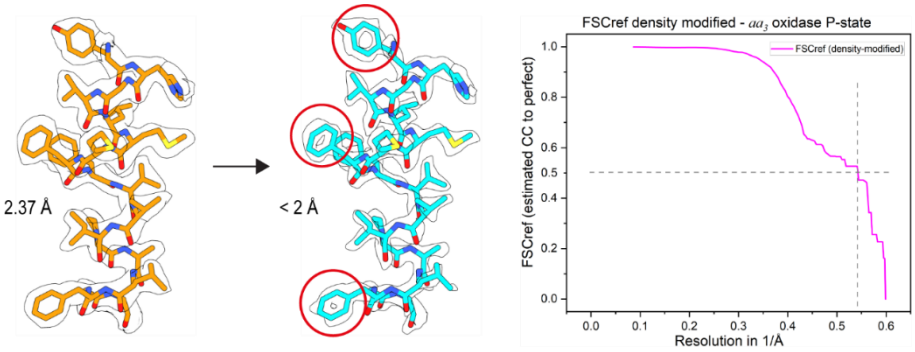


**Fig. 3.12. Density-modification of the P state map.** The density-modified map provides a significantly increased quality of the reconstructed map as can be seen for the aromatic residues. This figure was prepared by using Chimera.

independent are available which provides the opportunity to estimate resolution-dependent errors by comparison of Fourier transforms of both half maps. For that reason, a more complete error model can be calculated resulting in a more accurate final map with more locally distinct map features [87]. For the **O**, **R**, **$P_{co}$** and **F** dataset, significant resolution improvements were observed for each map after applying density modification. However, the resolution estimations, especially for the **$P_{co}$** (~ 1.9 Å) and **O** (~ 1.9 Å) state, might be partly overestimated due to the extensive calculation procedure (personal communication with Dr. Terwilliger). Nonetheless, judged by the density map quality itself, it is apparent that the **P** state map reflects local resolutions of higher than 2 Å (Fig. 3.12). Density-modified maps for **O**, **R**, and **F** state are presented in figure 3.13

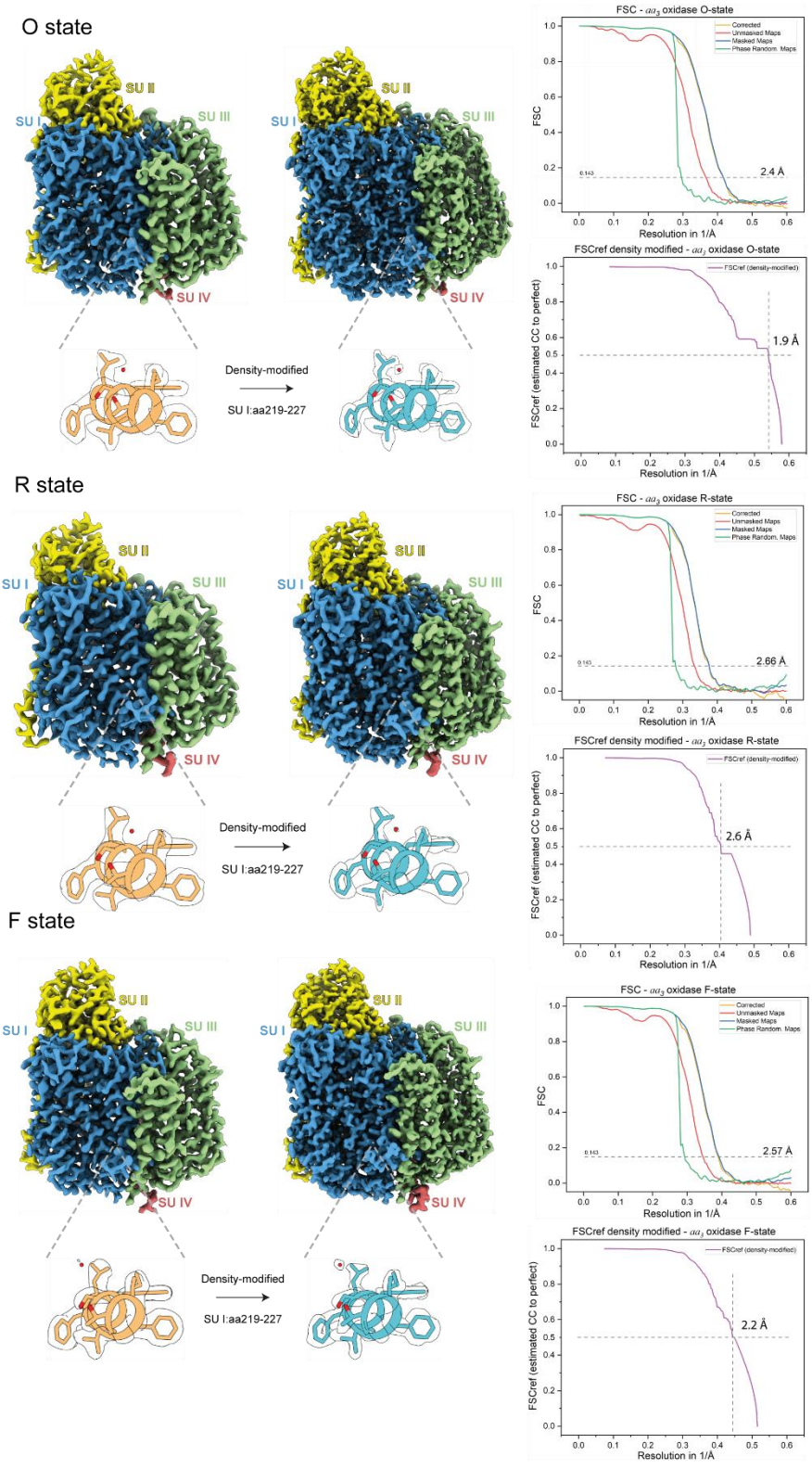


**Fig. 3.13. Density-modified maps of the O, R and F state.** For the **O** state, a larger map improvement was observed reasoned by the initial higher resolution (2.4 Å) in comparison to the **R** (2.66 Å) and **F** (2.57 Å) state. Quality improvements were observed for each map. Maps were prepared by using Chimera.

### 3.5.2 Evaluation of the temperature factor (*B*-factor)

Commonly, cryo-EM maps usually show heterogenous distributions of *B*-factors associated with high variability in resolution within different regions of the same map. Regardless of the electron-induced state, the cryo-EM map of the reconstituted, four-subunit cytochrome *c* oxidase show high variations for the atomic vibrations and conformational flexibilities, ranging from 21 to 6 Å$^2$ (Fig. 3.14A). Lowest temperature factors were observed for the region around the metal cofactors (heme $a_3$/heme $a$) defining the active site. As shown in figure 3.11B and 3.14B, a correlation between low *B*-factors and locally higher resolutions in regard to subunit I and II is evident and points out the importance of evaluating the entire density map by working with local resolution filtering to reveal its fully unrestricted potential, an enormous advantage over data evaluation in crystallography.

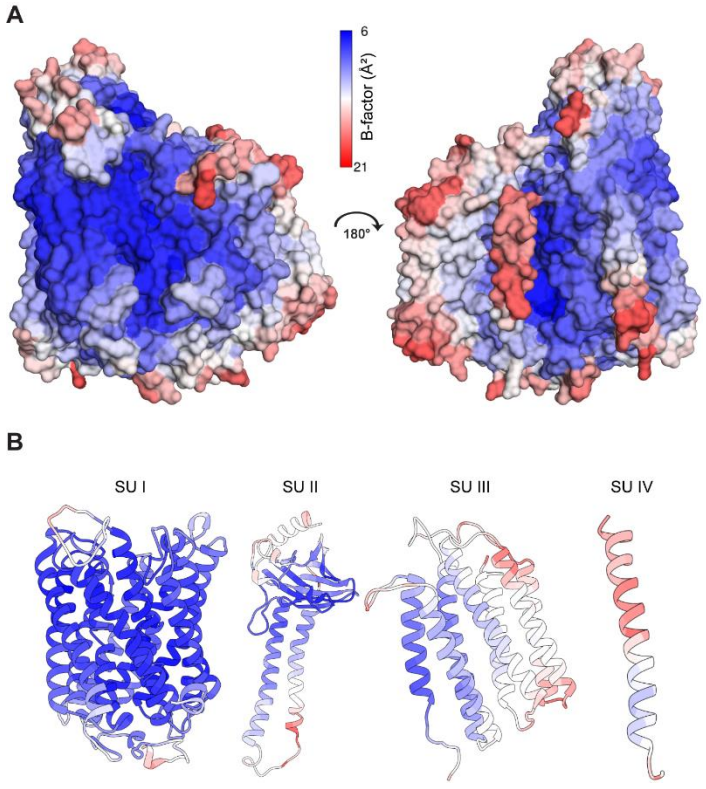


**Fig. 3.14. Illustration of atomic temperature factor (*B*-factor) distribution.** (**A**) The surface of density map of the C*c*O is colored based on its *B*-factors. Blue colored regions represent low values whereas red colored regions indicate high values. (**B**) *B*-factor illustration of each the structure of each subunit. Maps and structures were prepared by using ChimeraX.

### 3.6 Evaluation of the density maps for each state

While the architecture and composition of the C*c*O from *Paracoccus denitrificans* is considered as well elucidated, high-resolution structural evidence of the catalytic transition states of the dioxygen reduction reaction have remained elusive in the past (Fig. 3.15). With the aid of single particle cryo-EM, it became more feasible to generate reproducible and reliable structures of high-resolution allowing to address unsettled questions regarding the structural composition of the active site during the catalytic turnover of oxygen reduction. In order to provide a comprehensive and in-depth overview of the mechanism of action, the determination of the three-dimensional structures of each state, **O**, **R**, $\mathbf{P_{CO}}$ and **F**, was a required criterion to provide a deeper

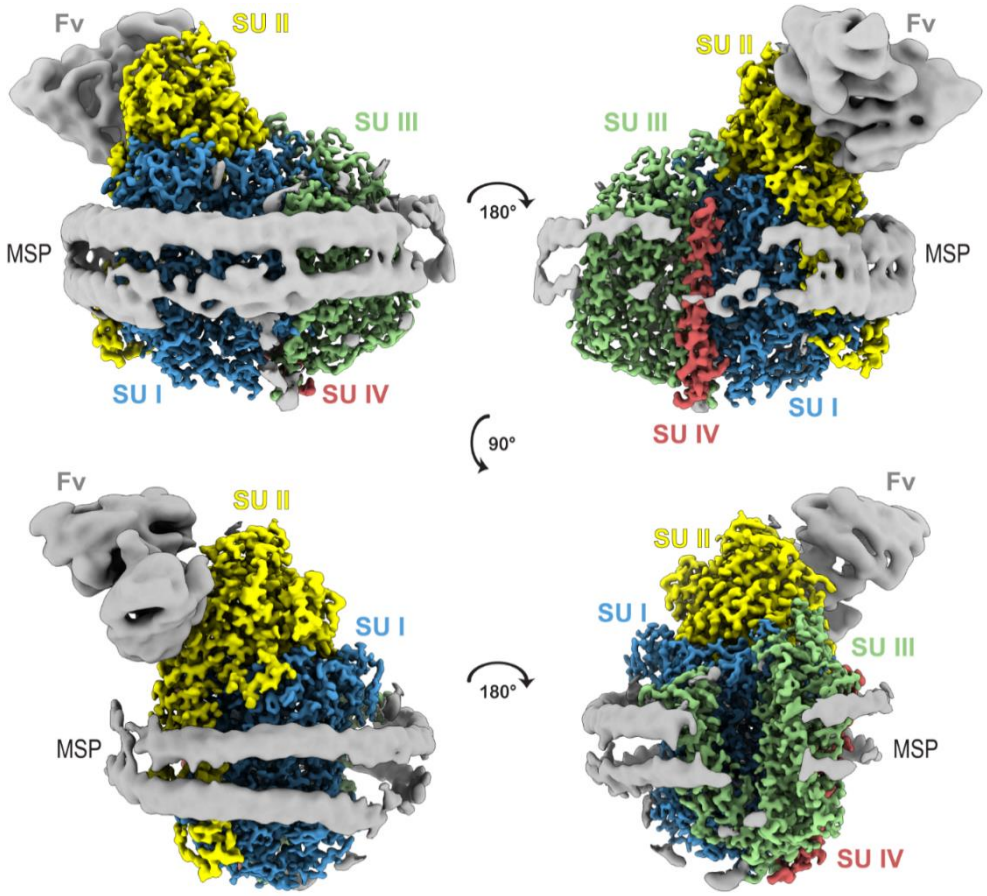


**Fig. 3.15**. **Cryo-EM density map (P state) of the $aa_3$ C*c*O oxidase from *P. denitrificans***. Surface representation of the fully assembled, reconstituted protein complex with the Fv fragment (grey) attached to the periplasmic surface of SU I. The membrane scaffold protein (MSP) encompasses the membrane protein as a double layer. Subunit I, II, III and IV are shown as blue, yellow, green and red, respectively. This figure was prepared by using Chimera.

understanding for the processes occurring at the binuclear site upon dioxygen reduction. By applying local masks and thereby gaining more reliable structural information about the regions of interest due to higher resolution, interesting and undescribed findings were discovered for the cytochrome *c* oxidase. Even though structures of this complex with higher resolution, mainly from the more complex eukaryotic counterpart (up to 2 Å), have been reported in the past years, they fail to adequality address questions concerning the active site as the toolset for data processing in crystallography is more limited (resolution filtering).

In the following subsections the structure of each intermediate state, with a prioritized focus on the binuclear site, will be presented in detail. Data set and refinement statistics of each structure are summarized in table 3.1.

**Table 3.1. Data and refinement statistics of the intermediate states of cytochrome *c* oxidase**

| | O-state | R-state | P-state | F-state |
|---|---|---|---|---|
| **Data collection** | | | | |
| Accession number | EMD-11925 | EMD-11922 | EMD-11921 | EMD-11924 |
| Magnification | 96k | 96k | 96k | 96k |
| Voltage / kV | 300 | 300 | 300 | 300 |
| Dose / $e^{-}$ Å$^{-2}$ | 30 | 30 | 30 | 30 |
| Pixel size / Å | 0.833 | 0.833 | 0.833 | 0.833 |
| Defocus range / µm | -0.5 to -2.5 | -0.5 to -2.5 | -0.5 to -2.5 | -0.5 to -2.5 |
| Recorded movies | 5140 | 5835 | 4487 | 4613 |
| Final particle images | 234,751 | 289,627 | 268,222 | 207,736 |
| Camera | Falcon III | Falcon III | Falcon III | Falcon III |
| Microscope | Titan Krios G3 | Titan Krios G3 | Titan Krios G3 | Titan Krios G3 |
| **Image processing** | | | | |
| Initial model | *de novo* generated with RELION 3.1, filtered to 15 Å | | | |
| Resolution ($FSC_{0.143}$) / Å | 2.4 | 2.66 | 2.37 | 2.57 |
| Applied B-factor / Å$^2$ | -100 | -120 | -94 | -109 |
| Density modified resolution / Å ($FSC_{ref}$) | 1.9 | 2.5 | 1.9 | 2.3 |
| **Model refinement** | | | | |
| PDB accession | 7AU6 | 7ATN | 7ATE | 7AU3 |
| Validation | | | | |
| $FSC^{map\text{-}to\text{-}model}_{(0.5)}$ / Å | 1.9 | 2.6 | 1.9 | 2.3 |
| MolProbity score | 2.25 | 2.10 | 2.1 | 1.88 |
| Composition | | | | |
| Atoms | 9024 | 8944 | 9056 | 9012 |
| Protein residues | 1092 | 1098 | 1098 | 1096 |
| Waters | 148 | 83 | 145 | 162 |
| Ligands | 2 PC1, 2 HEA, 1 CUA, 1 MN, 1 CA, 1 CU, 1 PEO, 6 OXY | 1 PC1, 2 HEA, 1 CUA, 1 MN, 1 CA, 1 CU | 1 PC1, 2 HEA, 1 CUA, 1 MN, 1 CA, 1 CU, 1 PGV, 1 PEO | 2 HEA, 1 CUA, 1 MN, 1 CA, 1 CU, 1 PGV, 1 OX, 1 2FK |
| Bonds (R.M.S.D.) | | | | |
| Length (Å) | 0.013 | 0.012 | 0.010 | 0.016 |
| Angles (°) | 1.576 | 1.136 | 1.135 | 1.961 |
| B-factors (min/max/mean) | | | | |
| Protein | 5.98/15.06/9.19 | 4.30/35.23/14.04 | 7.1/27.89/14.06 | 3.48/10.9/5.58 |
| Ligand | 6.12/15.82/10.23 | 5.01/41.57/19.82 | 8.96/24.67/15.79 | 4.58/15.42/6.97 |
| Waters | 6.75/10.13/8.52 | 5.64/15.48/9.49 | 8.51/16.13/11.91 | 3.7/6.35/5.18 |
| Clashscore | 18.54 | 14.32 | 16.89 | 13.09 |
| Ramachandran plot (%) | | | | |
| Favored | 96.49 | 96.51 | 96.79 | 97.70 |
| Allowed | 3.51 | 3.39 | 3.21 | 2.11 |
| Outliers | 0 | 0.09 | 0 | 0.18 |
| Rotamer outliers (%) | 1.9 | 1.89 | 1.67 | 1.78 |

### 3.6.1 O state

Based on the high-resolution density map of the fully oxidized state (**O** state) with local resolutions of sub 2 Å around the BNC, identification of a prominent and distinct density located between $Cu_B$ and heme $a_3$ was possible (Fig. 3.16A). Careful refinements with respect to distances to neighboring molecules let to the decision that the elongated shaped density corresponds most likely to a dioxide species. Indeed, such an assignment of a bridging dioxide molecule, presumably a peroxide species, strongly substantiates previous assumptions and observations explicitly for the A-type C*c*O and its eukaryotic counterpart [69, 71, 73]. For reasons of electrostatic repulsion forces coming from both positively charged ions, the presence of a negatively charged ligand appears to be favorable to adequately compensate those repelling forces. According to the Cambridge Structural Database, more than 90 non-protein-derived peroxide structures are reported that bridge two metal ions with an average length of 1.44 ± 0.06 Å (± s.d.) for the average O-O distance. This is in accordance with the fitted peroxide dianion in the observed density at the BNC of the **O** state density map (1.42 Å) [99]. Additionally, a second close-by density, corresponding to another dioxygen molecule, could be identified which appears to interact with $Val^{279.I}$. This observed density strongly resembles to the aforementioned density located in-between both metal cofactors in terms of the size and its shape. This newly discovered resting oxygen molecule is located at the end of an identified substrate conducting channel that points to the hydrophobic membrane interface near TMH1.I, the potential entry point for dioxygen from the membrane. Further details regarding this structural feature will be presented in detail in section 3.7.

As the available space within the binuclear center is strongly limited, spatial allocations and refinements of molecules must be performed as precisely as possible with respect to the van der Waals radii of each atom. The Fe$a_3$-$Cu_B$ distance is 4.7 Å with the heme $a_3$ iron (93°) coordinated almost in plane to the porphyrin scaffold, calculated from the merged bond angles heme $a_3$ N-Fe-$His^{411.\,I.}$ The crosslink distance between $N_{\varepsilon 2}$-$His^{276.I}$ and $C_{\varepsilon 2}$-$Tyr^{280.I}$ is 2.3 Å. As presented in figure 3.16B and C, the postulated bridged peroxide resides in a planar position with a reported distance of 2 Å and 2.5 Å

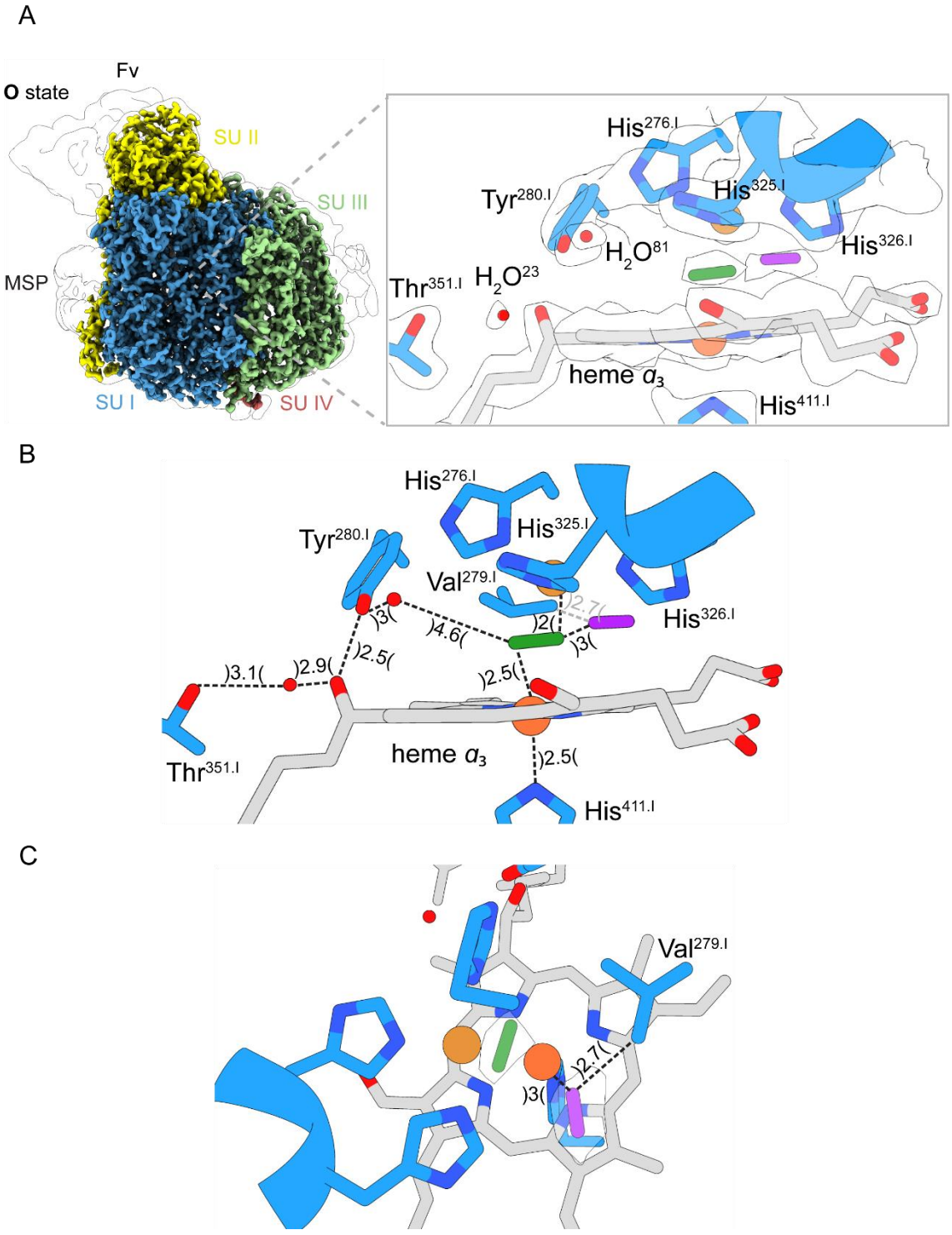


**Fig. 3.16**. **Cryo-EM density map (O state) and modelled structure of the binuclear site in C*c*O. (A)** Structural overview of the binuclear site in the **O** state. The bridging dioxide species (green) is located in-between the iron (orange) and the copper (brown) atom. In close proximity to the observed bridging ligand, a second prominent density, presumably molecular oxygen (purple), is located. The corresponding density map is illustrated a as white surface. **(B)** Measured distances (Å) for the assigned molecules at the active site. **(C)** Top view of the active site. This figure was prepared by using Chimera.

to the copper and iron atom, respectively. The potential existence of two individual hydroxide ions, as suggested in the past, were strictly excluded as those couldn't be accommodated due to the limited available space in proximity to both metals. On top of that, the density itself clearly indicates a single present molecule and neither a single nor two hydroxide ions could efficiently compensate both positive charges coming from the metal cofactors. With a measured distance of 3 Å to the neighboring peroxide species (edge-to-edge), the second dioxygen molecule (interacting with $Val^{279.I}$) is in accordance with geometrical and steric restraints, excluding a potential clash caused by van der Waals radii of the two independent oxygen atoms (~150 pm). One water molecule ($H_2O^{23}$) is hydrogen bonded (2.9 Å) to the OH group of the hydroxyethylfarnesyl residue of heme $a_3$ and to $Thr^{351.I}$ (3.1 Å) which constitutes the end of the short proton pathway, namely the K-pathway. The second water molecule ($H_2O^{81}$) is hydrogen bonded to the redox-active $Tyr^{280.I}$ and could possibly mark the product-exit channel.

### 3.6.2 R state

The density map of the fully reduced state (**R** state) provides insights into expected structural features of the active site of C*c*O. As highlighted in the previous sections (Fig.1.6), the heme $a_3$ resides as high-spin species with penta coordination and the $Cu_B$ is cuprous. In this state, the heme is capable of binding ligands, such as $O_2$, CO and NO. Upon binding of a dioxygen ligand transition from a high-spin to a low-spin heme occurs. The reported resolution of 2.6 Å is of sufficient quality to clearly assign a fully reduced state as the observed bridging density in the **O** state has vanished (Fig. 3.17A). Undoubtedly, the resolution of the **R** state map is in average ~0.5 Å lower than the other obtained density maps which can be justified, inter alia, by the fact that this state had to be "induced" by the addition of sodium dithionite causing a potential negative influence on the vitrification process (ice-thickness) and distribution of embedded particles [100]. In this context, it should be noted that the fully reduced state represents a four-electron reduced state as $Cu_A$, $Cu_B$ and both hemes are reduced and in a resting state. The primary reason for recording the **R** state was to confirm the

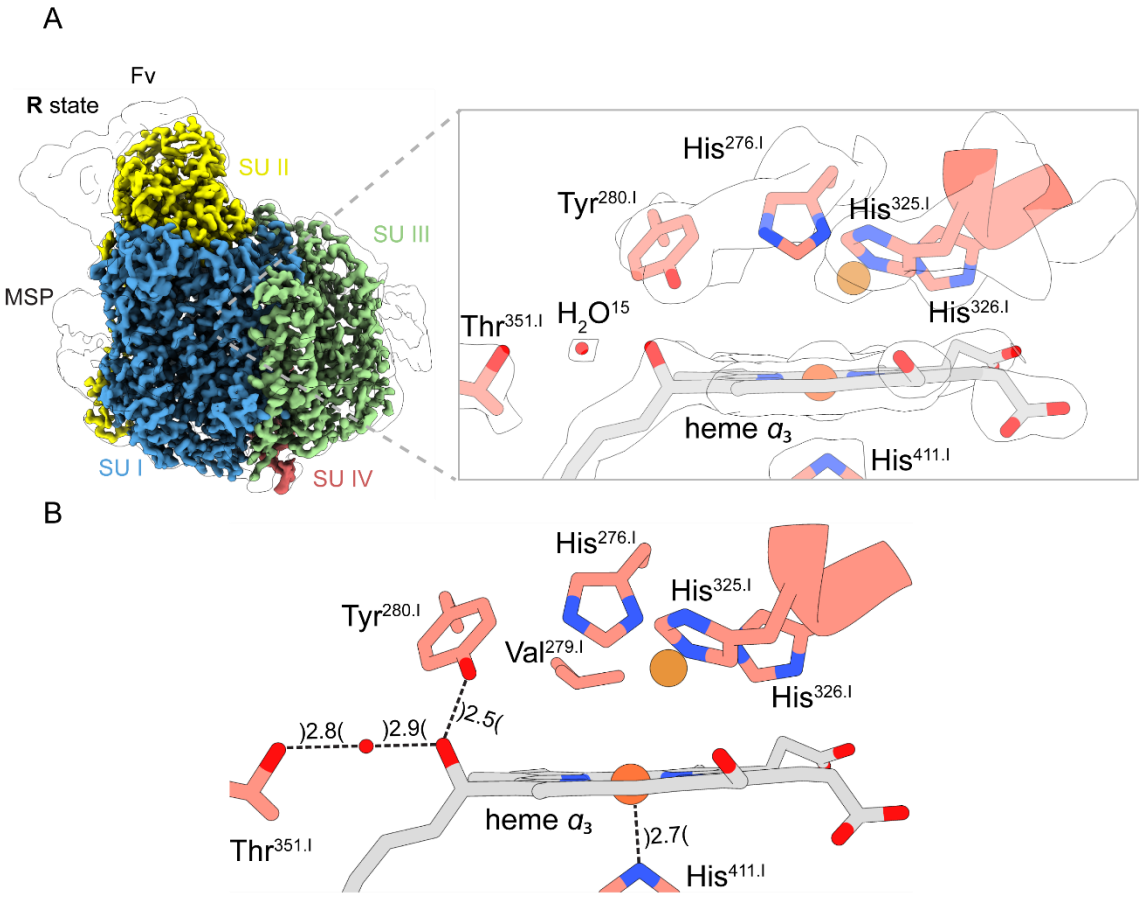


**Fig. 3.17**. **Cryo-EM density map (R state) and modelled structure of the binuclear site in C*c*O. (A)** Structural overview of the binuclear site in the **R** state. No significant densities located between the iron (orange) and copper atom (brown) were observed, indicating a fully reduced binuclear site. The corresponding density map is illustrated as a white surface. **(B)** Measured distances (Å) for the assigned molecules at the active site. This figure was prepared by using Chimera.

presence of a newly discovered oxygen conducting pathway observed in the **O** state map, therefore serving mainly as a reference structure. However, this will be presented in detail in section 3.8.

The interatomic Fe$a_3$-$Cu_B$ distance of 3.9 Å is around 0.7 Å shorter in comparison to the fully oxidized state and the central coordinated iron of heme $a_3$ is more out of plane in the ring system (82°, 93° **O**-state), resulting in an increased distance between the central iron and His$^{411.I}$ (2.7 Å) (Fig. 3.17B). Additionally, the covalent crosslink distance between N$_{\varepsilon 2}$-His$^{276.I}$ and C$_{\varepsilon 2}$-Tyr$^{280.I}$ is 2.8 Å. Distinct movements of the corresponding polypeptide chains were not observed in any related map which strongly argues for a locally restricted, redox-coupled structural change at the binuclear center. Interestingly, the measured Fe$a_3$-$Cu_B$ distance of ~4 Å can be considered as unexpected as previous crystallographic structures of the A-type C*c*O reported distances of approximately 5 Å. Clearly, the positioning of $Cu_B$ and Fe$a_3$

depends on the oxidation state of the metal sites and points out a certain flexibility for both atoms unlike to what has been reported for the bovine counterpart [101]. Identical to the fully oxidized map, a distinct water molecule ($H_2O^{15}$) in proximity to $Thr^{351.I}$ (2.8 Å) is located and hydrogen bonded with a distance of 2.9 Å to the hydroxyl group of the hydroxyethylfarnesyl of heme $a_3$.

### 3.6.3 P state

The **P** catalytic intermediate state was stably induced via limited exposure to carbon monoxide and was unambiguously confirmed via uv/visible absorption spectroscopy (Fig. 3.6). It is important to note that two catalytically relevant **P** states exist, the $\mathbf{P_M}$ and the $\mathbf{P_R}$ state. The most noteworthy difference between these two states is the electron distribution on the metal cofactors. The $\mathbf{P_M}$ state, which is at a redox level two electrons above the **O** state, is formed spontaneously by decay of compound **A** under conditions where both the low-spin heme and $\mathrm{Cu}_A$ are oxidized, commonly known as a mixed-valence state. The $\mathbf{P_R}$ state, a redox level one electron above the $\mathbf{P_M}$ state, is formed from compound **A** under conditions where the enzyme is initially fully reduced implying a reduced $\mathrm{Cu}_A$ and heme $a$ upon molecular oxygen binding to heme $a_3$. So far, only one crystallographic structure of an oxygen intermediate is available with a reported resolution of 2.5 Å which is claimed to represent the three-electron $\mathbf{P_R}$ state [73]. Even though this structure brought initial findings regarding the structural context of the binuclear site upon **P** state formation, many questions remain unaddressed such as potential structural discrepancies between the $\mathbf{P_M}$ and $\mathbf{P_R}$ states as they share almost identical spectral properties.

The structural context of the binuclear site at a local resolution of 1.9 Å clearly resembles that of the **O** state (Fig. 3.18A). As both density maps ($\mathbf{O}/\mathbf{P_{CO}}$) are of almost equally high-quality and provide similar local resolution around the active site (< 2 Å), it appears to be reasonable to draw direct conclusions by comparing these maps. A specific density in between the two metal centers was identified and its elongated, cohesive shape indicates the presence of a residing dioxide species, arguing for an intact O-O bond in the $\mathbf{P_{CO}}$ state. Furthermore, the nearby and previously observed dioxygen molecule near $Val^{279.I}$ appears to be absent and replaced by a water

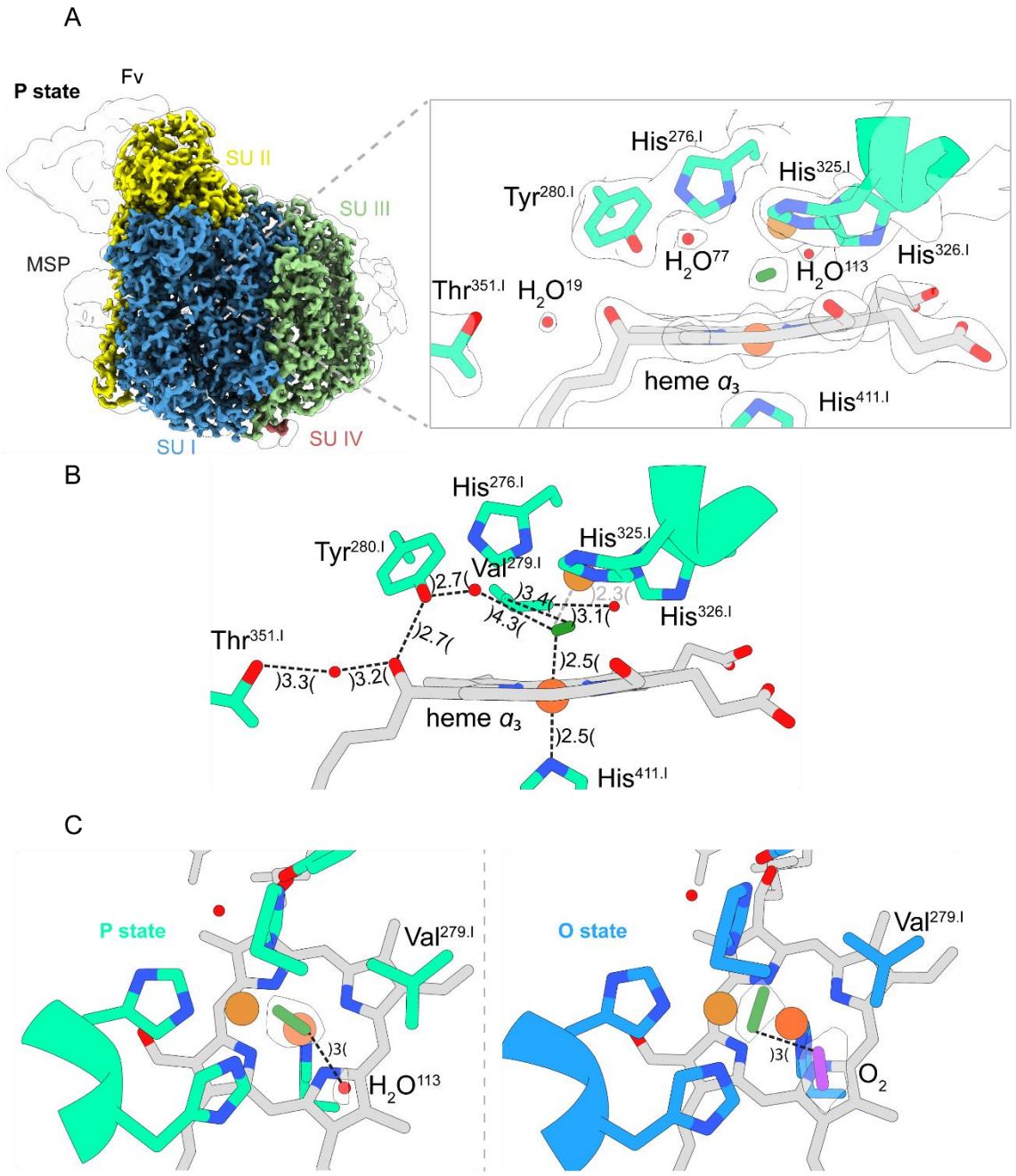


**Fig. 3.18**. **Cryo-EM density map (P state) and modelled structure of the binuclear site in C*c*O. (A)** Structural overview of the binuclear site in the **P** state. The bridging dioxide ligand (green) is embedded between the iron (orange) and the copper (brown) atom. The previously observed dioxygen molecule in the **O** state in the vicinity of $Val^{279.I}$ is replaced by a water ($H_2O^{113}$). **(B)** Measured distances (Å) for the assigned molecules at the active site. **(C)** On top view of the binuclear center of the **O** and **P** state to illustrate the rotation of the bridging dioxide species. The corresponding density map is illustrated as white-contoured. This figure was prepared by using Chimera.

($H_2O^{113}$).

The interatomic distance of Fe$a_3$-$Cu_B$ is 4.7 Å and the iron remains almost in the plane with the ring system (95°), sharing geometrical similarities with the **O** state structure. A distinct difference is found for the redox-active covalent crosslink distance of $N_{\varepsilon 2}$ - $His^{276.I}$ - $C_{\varepsilon 2}$-$Tyr^{280.I}$, shifting from 2.3 Å (**O**) to 1.6 Å ($\mathbf{P_{co}}$). Structural movements of the related polypeptide chains are not observed. Based on the spatial allocation of this density and due to geometrical and steric restrains, the existence of an oxoferryl heme species and a hydroxide ion or water bound $Cu_B$ center ($Cu_B$-$OH^-$/$H_2O$) is considered as unlikely as it was proposed based on previous functional studies (see review [102]). Modelling of these proposed occupancies would lead to a clash caused by van-der-Waals radii of the two non-intramolecular oxygen atoms as their distances are too short to each other (< 1.5 Å). Placing a dioxygen species in this spot is a logical consequence as geometrical criteria are met (van-der-Waals radii) and the cohesive, planar density corresponds most to a homonuclear diatomic molecule (Fig. 3.18B). Its distance to the copper and iron atom is 2.3 Å and 2.5 Å, respectively. The hydroxyl group of $Tyr^{280.I}$ is in hydrogen bond distance to $H_2O^{77}$ (2.7 Å) and to the OH group of the hydroxyethylfarnesyl of heme $a_3$ (3.2 Å). Even though, the **O** and **P** state appear to have a similar bridging density, the one observed in the **P** state is axially rotated by around 85° and points towards the newly appeared water molecule ($H_2O^{113}$) which has replaced the previously observed coordinated dioxygen molecule in the fully oxidized map (Fig. 3.18C). The measured distances here do not fall below 3 Å and are in good agreement with geometrical restraints.

### 3.6.4 F state

The **F** state is reported to be one redox level above the previous described $\mathbf{P_{Co}/P_M}$ state and formed upon protonation of the $\mathbf{P_R}$ state without additional electron input into the BNC. As described before, the ferryl-cupric species can be unambiguously assigned by its characteristic absorption maximum in the optical difference spectrum at ~ 580 nm (Fig. 3.5/3.6). Numerous Raman resonance spectroscopic studies have independently confirmed the presence of such a ferryl species for the **F** state and dioxygen bond cleavage has already occurred at this stage [63, 64]. So far, no structural attempts have been undertaken to unravel architectural disparities between the **P** and the **F** state which could adequately explain observed inconsistencies in earlier spectroscopic studies [67].

In order to gain insights into the previously unknown geometrical ligand arrangement of the ferryl-cupric **F** state, the cytochrome *c* oxidase was treated with an excess of hydrogen peroxide analogously to aforementioned Raman and EPR studies. The structural snapshot of the binuclear center was obtained at resolution of 2.3 Å. The interatomic space between $\mathrm{Cu}_B$ and heme $a_3$ does not show a distinct density as observed in the $\mathbf{P_{Co}}$ or **O** state structure (Fig. 3.19A). The absence of the previously coordinated dioxygen is apparent. Based on the density map features at the catalytic site, a geometrically optimized oxoferryl ligand at heme $a_3$ was modelled which agrees with previously postulated occupancies. Modelling of a water molecule as a potential fourth $\mathrm{Cu}_B$ ligand, providing a hydrogen bond to the oxoferryl oxygen, had to be excluded as the intermolecular spacing would be clearly too short (< 2 Å edge-to-edge distance). The Fe$a_3$-$\mathrm{Cu}_B$ distance of 4.5 Å is similar to that of the $\mathbf{O/P_{Co}}$ state while the coordinated iron is slightly more displaced from the center of the heme macrocycle plane (95°). Furthermore, the cross-linked $N_{\varepsilon 2}$ - $His^{276.I}$ - $C_{\varepsilon 2}$-$Tyr^{280.I}$ distance has significantly increased, to 2.7 Å, in comparison to the two-electron reduced $\mathbf{P_{Co}}$ state, indicating redox related conformational changes. Similar to the other states, distinct movements of related polypeptide chains are not observed. In addition, the bond distance between $His^{411.I}$ - Fe$a_3$ is shortened by 0.3 Å (2.2 Å) which can be explained by a different protonated state as outlined in a previous study (Fig. 3.19B) [12].

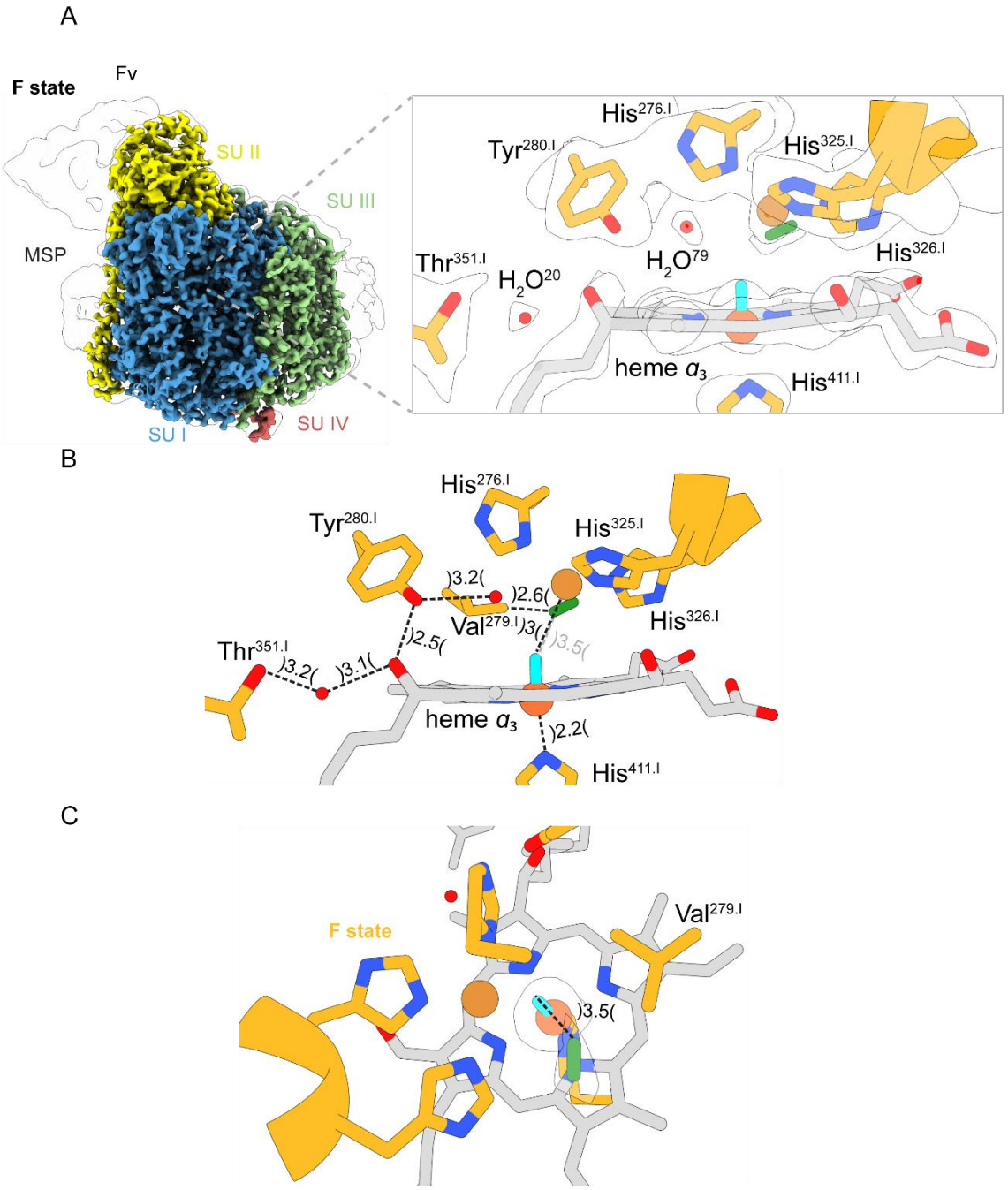


**Fig. 3.19**. **Cryo-EM density map (F state) and modelled structure of the binuclear site in C*c*O. (A)** Structural overview of the binuclear site in the **F** state. No bridging ligand is located between the iron (orange) and the copper (brown) atom. Instead, the density map may indicate the presence of an oxoferryl at the heme (cyan) and a dioxide species (green) in close proximity **(B)** Measured distances (Å) for the assigned molecules at the active site. **(C)** Top view of the binuclear center of the **F** state. The corresponding density map is illustrated as a white surface. This figure was prepared by using Chimera.

Intriguingly, a prominent and undescribed density is located in-between $His^{326.I}$ and $Val^{279.I}$ and in close proximity to the copper atom with a distance of 3.3 Å. The specific shape and spatial location of this density strongly argues for a coordinated dioxide species, most likely a superoxide. The bond length of the modelled iron-oxo complex ($Fe^{4+} = O^{2-}$) of 1.52 Å coincides with a previously reported distance of an oxoferryl species. Distances with a larger bond length (> 1.7 Å) are considered to represent a single bond species [103]. The interatomic oxygen-to-oxygen distance is 3.5 Å and thus it is not too close in regard to the van der Waals radii (Fig. 3.19C). Furthermore, the water molecules ($H_2O^{20}$, $H_2O^{79}$), coordinated by $Thr^{351.I}$ and $Tyr^{280.I}$, in proximity to the active site are also observed in the **O** and $\mathbf{P_{CO}}$ states but not for the **R** state.

### 3.7 Oxygen diffusion path

The dioxygen reaction itself occurs at the high-spin heme-copper complex and has been intensively studied in several families of heme-Cu oxidases. As the primary focus of previous functional and structural studies has been set mainly on understanding the catalytic mechanism of C*c*Os, rather little is known about a related pathway via which molecular oxygen arrives at the binuclear center. Until today, it seemed unclear whether specified oxygen channels are needed at all or oxygen can simply diffuse into the binuclear center. Functional evidence for a substrate channel was provided by the replacement of a conserved valine to isoleucine near the active site in cytochrome $bo_3$ of *E. coli*, resulting in an 8 times higher $K_M$ value for oxygen in comparison to the wild-type enzyme (*Paracoccus denitrificans*). Based on these findings it was assumed that the more bulky isoleucine causes a potential steric hinderance for oxygen diffusion [104]. A more recent crystallographic oxygen-mimicking study provided even more insight and proposed a Y-shaped channel with a length of 18-20 Å for the $ba_3$ cytochrome *c* oxidase, based on the affinities and occupancies of various noble gases bound to distinct sites [105]. However, a direct observation of oxygen molecules embedded in the protein interior leading towards the active site is still not present to date. The density map of the fully oxidized cytochrome *c* oxidase from this thesis work provides the first direct observation of dioxygen molecules leading in a direct manner towards the active site. The high-resolution map enabled modelling a continuous row

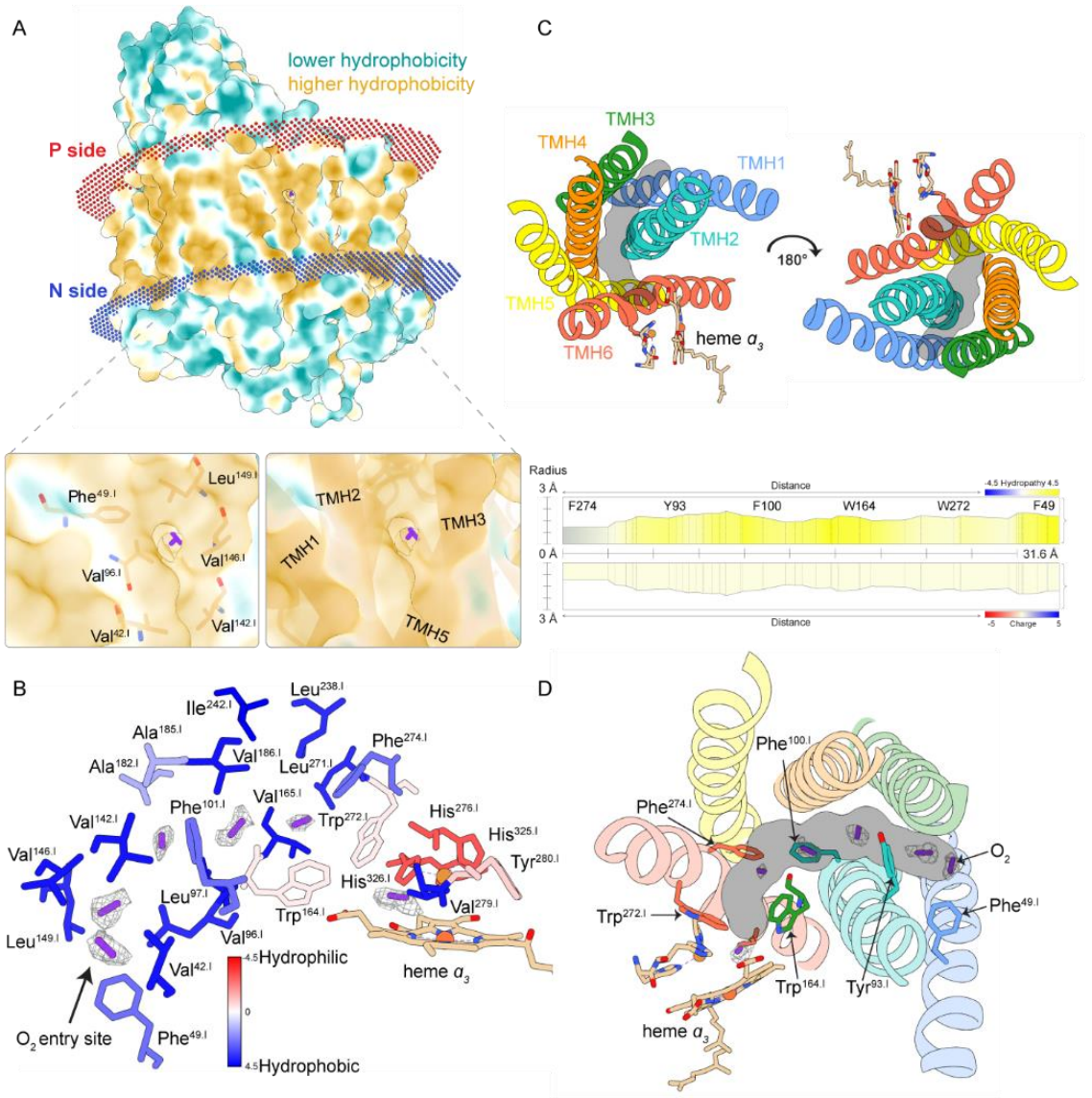


**Fig. 3.20**. **Oxygen pathway and channel composition. (A)** Surface representation of CcO colored by hydrophobicity. The identified oxygen entry site is located between TMH1.I and TMH3.I in the center of the membrane section. **(B)** Residues lining the oxygen-conducting channel are colored according to their hydrophobicity. **(C)** Interior channel embedded in-between six transmembrane helices and channel lining residues predicted by Mole 2.5. **(D)** Overlay of channel prediction by Mole 2.5 and individually displayed lining residues with observed dioxygen densities. Oxygen molecules are shown as violet. This figure was prepared by using Chimera.

of dioxygen molecules, starting at the hydrophobic membrane interface near Val$^{42.I}$ of TMH1.I and Leu$^{149.I}$, and ending at Val$^{279.I}$ in proximity to the dioxygen binding site of heme $a_3$ and $Cu_B$ (Fig. 3.20A). The entry point of the channel is defined by a very distinct hydrophobic cavity composed by the first and third transmembrane helix of the first subunit with a diameter of approximately 5 Å. The diameter of the embedded oxygen conducting channel constricts to 3.5 Å towards the oxygen reduction site which is still in accordance with the van der Waals radius of molecular oxygen. The channel is continuously characterized by hydrophobic side chains of amino acids therefore making a directed diffusion process possible. (Fig. 3.20B). For the **R** state, comparable corresponding densities in this location were not observed, pointing out that these observed densities are highly likely representing oxygen molecules waiting for reduction.

Furthermore, computational assisted calculations were performed by using the MOLE 2.5 server to map possible channels within the **O** state structure and to substantiate the finding made above. MOLE 2.5 is a universal toolkit for rapid and fully automated localization and characterization of channels, tunnels and pores in macromolecular structures. The used restraints and parameters are described in chapter 2.2.8. The use of this server enabled the identification and precise localization of a continuous hydrophobic pathway that clearly overlaps with the densities assigned to oxygen molecules (Fig. 3.20.C/D). The channel itself is predominantly formed by amino acids with hydrophobic side chains, namely Phe$^{274.I}$, Tyr$^{93.I}$, Phe$^{100.I}$, Trp$^{164.I}$, Trp$^{272.I}$ and F$^{49.I}$. Interestingly, this mapped pathway is in good agreement with the characterized oxygen channel of the B-type cytochrome *c* oxidase family mentioned above. Based on the location and length of this channel, a high similarity between HCOs and *bd*-type terminal oxidases is evident with respect to the dioxygen pathway [106]. The end of the mapped oxygen path is marked by Val$^{279.I}$ that resides in close proximity to the active site. This valine residue is fully conserved throughout four cytochrome *c* oxidases (*T. thermophilus, R, sphaeroides, P. denitrificans*, Bovine) and seems to be of importance for the access of molecular oxygen to the binuclear center [105].

### 3.8 Proton pathways

As described in section 1.4.2, the two proton conducting channels – the D- and the K-pathway – have been identified in bacterial quinol and cytochrome *c* oxidases by structure determination and mutagenesis experiments and have been further investigated by computational methods. From early experiments, it was evident that $Asp^{124.I}$ ("D") and $Lys^{354.I}$ ("K") play a crucial role for the enzymatic activity and associated proton pumping. The K-pathway provides a direct connection between the N-side of the membrane and the active site ($Lys^{354.I}$ → $Tyr^{280.I}$) while on the other hand, the D-pathway leads from the N-side of the membrane to the middle of the enzyme complex connecting two highly conserved residues ($Asp^{124.I}$ → $Glu^{278.I}$) which is located *ca.* 10 Å from the binuclear site. The D-channel accommodates several water molecules coordinated by polar amino acids. In contrast to that, the K-channel shows a few water molecules and no continuous proton translocation "wire" was observed in the past. In vicinity of the propionate region of heme $a_3$ (~3 Å), a water-filled cavity can be seen. This serves as a proton-loading site (PLS) and ejects protons in the direction of the P-side. On the basis of the aforementioned studies, it is believed that proton translocation through both channels is controlled or regulated by gating mechanisms e.g. isomerization of particular key residues upon different redox states [107].

Based on the obtained map of the fully oxidized state, 148 distinct densities were identified as water molecules in the structure of the C*c*O. A major fraction of those were assigned to the D-/ K-pathway and to the proton-loading site (Fig.3.21A). The allocated water molecules and the position of their corresponding key residues within the D-channel are in good agreement with very little variations with regard to previously published crystallographic structures. No further structural information could be obtained to adequately explain how protons might be efficiently transported from $Glu^{278.I}$ to the binuclear center as this distance is reported with 11 Å. Even though it is strongly assumed that certain residues are adopting different conformations depending on the protonation state, no structural alterations, regardless of the state of the density map, were observed. Special interest was put on the highly conserved residue $Asp^{124.I}$ which represents the entry point of the D-pathway. Due to its more

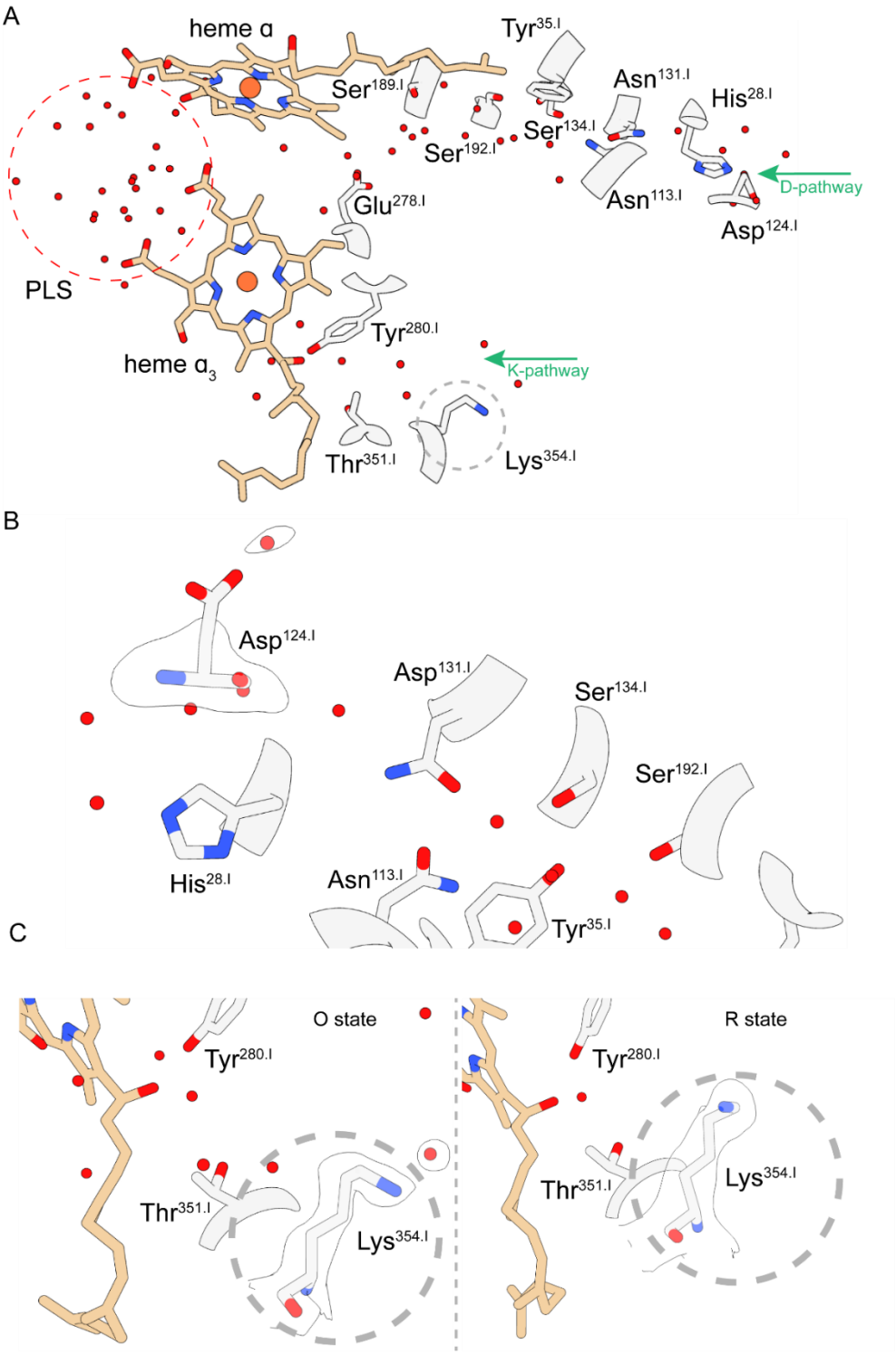


**Fig. 3.21**. **Depiction of the D- and K- proton transfer pathway in CcO. (A)** Key residues lining each proton pathway are indicated. Protons are taken up from the N-side and expelled from the PLS (proton-loading site) to the P-side of the membrane **(B)** Closer view of the D-pathway, showing the corresponding density of the key residue $Asp^{124.I}$, marking the entry point for proton uptake. **(C)** A redox dependent rotation of the key residue $Lys^{351.I}$, located in the K-pathway, is apparent. This figure was prepared by using Chimera.

distant and exposed position located on a flexible loop connecting TMH.2 and TMH.3 of subunit I, the carboxylic group is unambiguously suffering of adequate resolution caused either by the significantly higher *B*-value (> 120 Å$^2$) indicating an increased flexibility or the electron irradiation which is a commonly described problem (Fig.3.21B) [108]. A precise assignment of the side chain of Asp$^{124.I}$ was therefore not possible.

As can be seen in figure 3.21A, the K-pathway is rather short in comparison to the D-pathway. The distance is about 15 Å distance from the key residue Lys$^{354.I}$ to the cross-linked Tyr$^{280.I}$ of $Cu_B$ and provides a proton conduit from the negatively charged side (N-side) to the active site. Previous mutagenesis studies of Lys$^{354.I}$ showed a slowed-down reduction process of the fully oxidized state, whereas oxidation of the fully reduced state remained untouched. Based on these findings, it is believed that the K-pathway only provides chemical protons to the reductive half for the catalytic cycle [37, 109]. Furthermore, an electrometric study of a K319M variant suggested that reduction of the active site is connected to an observed electrogenic charge movement within the channel that could derive from flipping Lys$^{351.I}$ towards the BNC [110]. Interestingly, a distinct movement of the lysine side chain (Lys$^{351.I}$) was noticed when inspecting and comparing the density maps of each state. In the fully oxidized **O** map (as well as for the **P**$_{CO}$ and **F** map), the amino group points towards the N-side of the membrane whereas in the four-electron-containing reduced state, the headgroup rotates by approximately 90 degrees and is oriented towards the binuclear center (Fig.3.21C). Such a rotation was also postulated and observed in redox-state dependent dynamic simulation of the bovine C*c*O [111]. However, significant conformational changes in the tertiary structure of the surrounding helices located in subunit I and II which form the K-pathway were not observed.

# 4. Discussion

In order to understand the reduction process of molecular oxygen occurring at the binuclear center of cytochrome *c* oxidase in molecular detail, detailed structural information about the active site in different redox states is a prerequisite. While spectroscopic studies have contributed meaningful insights into this complex mechanism in the past, three-dimensional structural information of the distinct catalytic intermediates of the BNC have remained elusive. Therefore, the goal of this study was to combine uv/visible absorption spectroscopy with cryo-EM to investigate the structural composition of the binuclear center upon altering the redox states. Addressing these questions has become more accessible and feasible due to major technical improvements in the field of X-ray crystallography as it was recently demonstrated by Ishigami *et al.* by using time-resolved serial crystallography [73]. However, this approach is to a certain extent limited as it strongly depends on the formation of homogenous, well-diffracting and reproducible crystals in order to gather information of biochemically defined states of the C*c*O. Single-particle cryo-EM is ideally suited for these issues, as it is not dependent on the above-mentioned limitations and one can generate reproducible, high-resolution data in a relatively short time.

## 4.1 Characterization of studied C*c*O intermediates

The uv/visible absorption experiments verified the successful formation of the intermediates of interest, namely **O**, **R**, **P**$_{CO}$ and **F**, and are in good agreement with previous spectroscopic studies of bacterial C*c*O (Fig 3.6) [69]. Each intermediate state is indicated and distinguishable by its characteristic spectral fingerprint on the basis of shifting events of the corresponding Soret and α-band in the difference absorption spectrum. Starting with the oxidized state (**O**), its presence is indicated by a blue-shifted peak at 426 nm. The oxidized state was already recognized early on to exist in varying metastable states (“resting” versus “pulsed”, “slow” versus ”fast”) reasoned by

enzyme reduction and reoxidation processes with molecular oxygen [112]. Bloch *et al.* firstly provided evidence for this circumstance by showing that the reductive phase of the catalytic cycle (O → E → R) is exclusively connected to proton translocation only if followed immediately by an oxidative phase (R → O) where the enzyme is oxidized in presence of $O_2$ (Fig.1.6) [113]. Based on this observation the ferric/cupric intermediate was considered to exist as metastable state (**O**$_H$) under turnover conditions that can switch into a low-energy, resting **O** state upon depletion of electron donors. Even though following time-resolved titration experiments provided by Belevich *et al*. brought up additional evidence for the potential existence of such a metastable state, no spectroscopic differences between the **O** and **O**$_H$ state have been reported so far [114]. The possible existence of the **O**$_H$ state is to be doubted in view of the recent finding of Vilhjalmsdottir *et al.* [115]. However, as the sample preparation procedure for all cryo-EM studies involved the oxidation of the C*c*O in the presence of ferricyanide to provide an equal redox level and prevent unwanted electrogenic reactions, the possibility to obtain a structural mixture reflecting both species (**O**/**O**$_H$) can be considered as unlikely. As recently highlighted in a quantum mechanical calculation study by Bloomberg *et al*., a structural discrimination of those states would be certainly impossible as those observed difference most likely solely arise as a result of chemical modifications of the binuclear center and nearby redox active residues [116].

The **P$_{CO}$** intermediate species is characterized by its absorbance band at 607 nm with a red-shifted Soret band to 433 nm and its presence was unequivocally confirmed in the corresponding spectrum prior and after sample vitrification (Fig.3.6). The **P**$_{CO}$ state represents a two-electron reduced state after the reaction with molecular oxygen upon carbon monoxide treatment, whereas a three-electron reduced **P** state, termed **P**$_R$, was also observed during the reaction of fully reduced C*c*O with molecular oxygen [117]. In simple terms, the redox states of **P**$_{CO}$ and **P**$_R$ differ by 2 and 3 electrons, respectively, from the **O** state (Fig.1.6). Already early on, Morgan *et al.* outlined that it is not possible to fully establish distinctness between the two-electron and three-electron reduced **P** states based on the spectral properties, suggesting that the redox state of heme $a_3$ and the configuration of the heme-oxygen moiety are identical [67]. Limited exposure to carbon monoxide at alkaline pH ensured the enrichment of the two-electron reduced **P** species and potential overreduction, leading to a three-

electron reduced state, was prevented by tracking the red-shift of the Soret band. Clearly, a red-shift by a higher extend (> 440 nm) would have indicated an accumulated population of the $\mathbf{P}_R$ species. However, this was not the case as the Soret band of $\mathbf{P_{CO}}$ state prior and after sample vitrification remained around 433 nm (Fig 3.6). The co-existence of compound **A**, which is described to be converted by electronic reorganization within the binuclear center to the two-electron reduced $\mathbf{P_{CO}}$ state without additional electron uptake, can be excluded as no corresponding absorption in the α-band (595 nm) was observed (Fig. 3.6) [45].

The ferryl-cupric species (**F**) is indicated by an absorbance band at 585 nm in the difference spectrum and is known to be, in terms of redox levels, one electron above the $\mathbf{P_{M/CO}}$ state and equal to the $\mathbf{P_R}$ state. [118]. Based on observations in Raman spectroscopy studies, Oliveberg and Malmström proposed that the **F** state of the binuclear center results from the $\mathbf{P_R}$ state and just differs by one more proton residing in the latter intermediate [119]. Both states have been subject of considerable controversy in the last years as their corresponding optical spectra are very different in the α-band (607 nm vs. 585 nm) which suggest a chemical modification of greater extent on the porphyrin-ring system. It was suggested that this extra proton could form a water molecule as the fourth ligand of $\mathrm{Cu}_B$ and this aquo ligand could donate a hydrogen bond to the oxoferryl ligand that causes a symmetrical shift of the heme moiety of the active center resulting in a modified α-band. Yet, any structural evidence for that claim is missing as no dedicated **F** state structure is present to date and it appears questionable if a single proton reorganization process like this could lead to such a drastic change in the α-band of the spectrum. Even though, a recent XFEL bovine C*c*O structure from Ishigami *et al*. gave a first structural glance into the binuclear center upon $\mathbf{P_R}$ state formation, a more distinct assignment of the residing species is missing as the shown spectrum of the measured crystals does not include any information about the associated α-band, hence a mixture of $\mathbf{F/P_R}$ species has to be considered as likely [73].

### 4.2 Interpretation of the density maps in different redox states

In this work, it was shown that cryo-EM can be a valuable method for studying and investigating the structural composition of the binuclear center in C*c*O from *P. denitrificans* with respect to obtain high-resolution snapshots and coherent data sets of different biochemically defined states. This novel approach is of significant advantage over crystallography as it does not rely on crystal formation and makes a more close-to-native study feasible. Even though, numerous high-resolution structures from bovine and bacterial $aa_3$-type C*c*O are accessible, the majority of these represent either the fully oxidized or reduced state of the binuclear center. Other intermediate states of potentially higher interest, e.g. $\mathbf{P_M}$, $\mathbf{P_R}$ or **F** state, are not present or of insufficient quality to properly assign ligands in or around the active site. Recent developments of optical components for TEMs and the introduction of direct electron detectors have resulted in unprecedented possibilities to structurally characterize membrane proteins at high resolutions. Due to these advancements, unaddressed questions with respect to structural reorganization processes upon altered redox levels of C*c*O are moving more into the focus of research. At this point, it should be stressed that in-depth understanding of local events occurring at the binuclear center are inevitably connected to proton and electron translocation processes. Nowadays, such short-lived catalytic transitions can be adequately investigated by computational methods once a solid structural framework for *in silico* experiments is provided. In the following chapters, structural difference between the resolved catalytic intermediates of C*c*O are discussed.

#### 4.2.1 O state

In the **O** state structure, the presence of a prominent density within the binuclear center between heme $a_3$ and $\mathrm{Cu}_B$ was evident and described as a dioxide species (Fig.3.16). In the light of recent high-resolution crystallographic structures and numerous postulations pointing out that a negatively charged ligand has to be present to compensate the electrostatic repulsion between the two metals, a residing peroxide

dianion at that location appeared to be reasonable. This assumption was supported by the fact that a negatively charged ligand is required to account for the strong antiferromagnetic coupling between both metals observed by EPR [39]. The observed density clearly represents a homonuclear diatomic species because of its cohesive, longitudinal shape. Two hydroxide ions couldn't efficiently reside in this location due to the strongly limited space in regard to the metals and to each other. Therefore, the assumed existence of a water molecule or a hydroxide group as a $Cu_B$ ligand as it was originally proposed by Fann *et al.* had to be excluded [120]. Also, a peroxide dianion at this location make sense as the dianion could stabilize the BNC and the entire structure in regard to compensation of electrostatic repulsion forces. However, the interpretation of a stable peroxide at the active site of oxidized C*c*O was questioned by Kalia et *al.* on the basis of quantum chemical calculations in combination with spectroscopic data and re-refinement of two X-ray structures [121]. Based on XFEL studies conducted on $ba_3$-type cytochrome *c* oxidase from Andersson *et al*., they concluded that the subsequent ligand formation is affected by the exposure time to X-rays, the choice of the crystal growing method and applied temperature conditions resulting in either a single-oxygen molecule or a peroxide molecule formation [122]. Considering the fact that the **O** state density map (cryo-EM) showing a bound dioxygen species at the active site, it appears to be likely that observed differences in crystal structures are rather a result from the protein crystallization process itself. Even more importantly for cryo-EM, the sample is prepared by fast freezing in liquid nitrogen directly from a close-to-native buffer solution, therefore maintaining the C*c*O in its soluble state in comparison with a state in the crystal packing constraint. It is important to consider that beam-induced radiation damage, either caused by X-rays or the electron beam, is potentially present and could lead to certain artefacts e.g. breakdown of chemical bonds. However, incidents like that were more commonly reported for structures with higher doses (> 30 $e^-/Å^2$) and for carboxylic sidechains located more distantly with intrinsic higher *B*-factors as they interact more with the outer environment [108]. As the binuclear center of C*c*O is deeply embedded in the membrane protein itself, it appears to be unlikely that the active site could be affected by such an event. As this is, to date, the first cryo-EM structure of a fully oxidized $aa_3$-type CcO, a further confirmation of the observation made at the active site by another EM structure would be desirable. The recently published supercomplex structure (Complex III/IV) by Sun

*et al.* is not of sufficient quality (~3.5 Å), especially at the binuclear center, to adequately address this question [123].

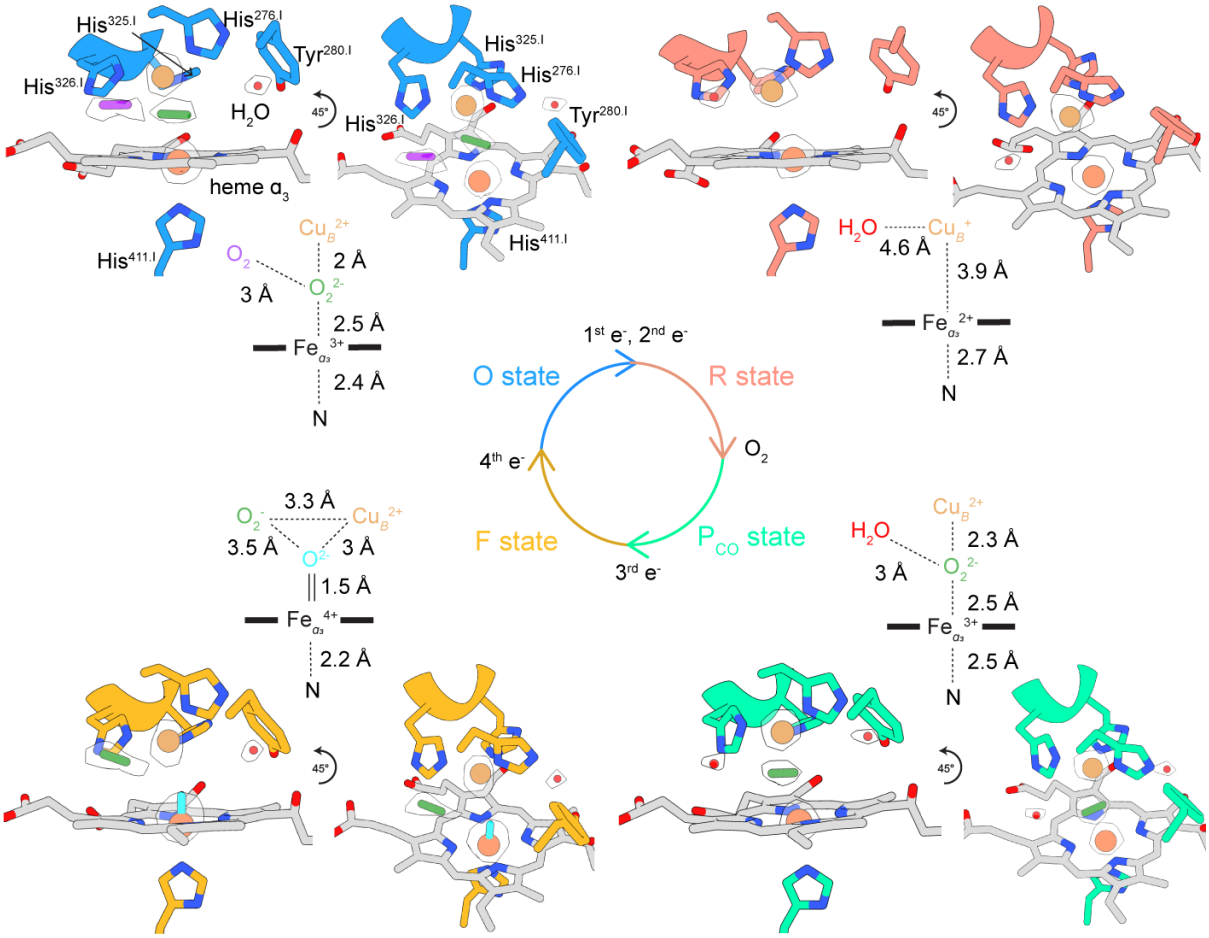


**Fig. 4.1**. **Structural reorganization of the binuclear center in different catalytic states of the C*c*O.** The heme remains in planar position while distinct rearrangements of dioxygen species and neighboring amino acids can be observed for each presented state. For reasons of simplification, the fully reduced **R** state represents the catalytic **R** state (see context). Corresponding densities are illustrated as a white surface. Local distances are indicated. This figure was prepared by using Chimera.

### 4.2.2 R state

The structure of the fully reduced **R** state C*c*O did not show significant changes in the overall structure of the enzyme. As was to be expected the absence of a bridging ligand between $Cu_B$ and Fe$a_3$ was observed. It is important to note that the fully reduced state is not part of the natural reaction cycle of cytochrome *c* oxidase and the obtained reduced structure reflects the four-electron reduced state under aerobic conditions. The major purpose of obtaining the structure was to serve as a reference to investigate certain structural rearrangements in comparison to the fully oxidized intermediate, especially for the newly discovered oxygen channel. While for all three intermediate states (**O**, **$P_{Co}$**, **F**) a water molecule with a hydrogen bond to Tyr$^{280.I}$ (2.7 – 3.2 Å) was observed, the fully reduced structure did not show a comparable density at this location. In contrast to this, the fully reduced C*c*O structure from *R. sphaeroides* accommodates a water at that position, residing in close proximity to the redox-active tyrosine [124]. A plausible and simple explanation for this might be the difference in resolution as the structure from Qin and coworkers has a resolution of (2.1 Å). A further, significant difference between both structures is the measured interatomic distance between the metal cofactors (Fe$a_3$/ $Cu_B$). Numerous crystal structures of reduced $aa_3$-type C*c*O are showing a slight displacement of the embedded iron in the porphyrin ring towards the His$^{411.I}$ ligand with a distance of ~ 4.9 Å. However, this observation does not match with the here presented **R** state structure as the measured distance has a length of 3.9 Å, approximately 1 Å shorter. One could argue that the **R** state does not represent at all a fully reduced state or is just partially reduced, however, the corresponding spectrum clearly indicates the opposite and the sample was vitrified in the presence of sodium dithionite. A more plausible explanation for this discrepancy might come from the method itself as the physical nature and mode of interaction of the incident beam differ strongly. As mentioned above, the potential impact of beam-induced artefacts cannot be completely ruled out [108]. For reasons of comparability, a further structure of the **R** state obtained by cryo-EM would be useful to independently confirm this observation.

### 4.2.3 P state

The **P** intermediate in the catalytic cycle of the C*c*O can be induced by using different approaches [69]. As the approach had to guarantee a stable species with a certain lifetime, generating the **P** state by limited exposure to carbon monoxide in the presence of oxygen was a necessary prerequisite. The presence of the $\mathbf{P_{CO}}$ species was unambiguously confirmed by absorption spectroscopy (Fig. 3.6). The structural context in and around the binuclear site can be considered as surprising due to the fact that the observed density between the two metal centers of the active site reflects a diatomic species, indicating a still intact O-O bond in the $\mathbf{P_{CO}}$ state. This finding is in clear contradiction to previously published studies as it is commonly assumed the dioxygen bond is broken already upon **P** state formation. This view is based on resonance Raman spectroscopy and appears to be widely accepted [125]. However, early on Ferguson-Miller noted that the species providing the signal in Raman spectroscopy may not reflect the most abundant population in the sample [126]. In contrast, particle averaging and class sorting in cryo-EM result in weighted map densities with the most populated species therefore having the strongest contribution to the map features. The density itself does not leave much room for speculations as the shape strongly resembles the other observed oxygens, especially the ones observed in the oxygen conducting channel. The next question that arises is what about the chemical experiments that have provided evidence for a split dioxygen bond in the $\mathbf{P_{CO}}$ state shown by Fabian *et al.* [127]. In their study, the $\mathbf{P_{CO}}$ state was generated by flashing off the carbon monoxide from mixed valence CO bound C*c*O in the presence of $^{18}O_2$. Around half of the $^{18}O$-label, compared to the amount of $\mathbf{P_{CO}}$ state C*c*O, was found as water. However, the reaction of CO with oxygen yielding $CO_2$ and water would provide the same experimental result. Clearly, the presence of a residing carbon monoxide within the active site has to be excluded on the basis of the investigated spectroscopic features. Not only the presence of peroxide dianion can be considered, also a neutral dioxygen molecule seems logical if one accepts that the **O** state BNC, which contains two electrons more than that of the $\mathbf{P_{CO}}$ state, accommodates a peroxide dianion. Since the structural composition of the BNC in $\mathbf{P_{CO}}$

state is obviously similar to that of the **O** state, this could also be used to justify the spectroscopic similarity.

Undoubtedly, this leaves much room for speculation and to provide further clarity more structural data of the two-electron reduced $\mathbf{P_{co}}$ state would be desirable, especially in combination with spectroscopic measurements such as Raman resonance spectroscopy to make a more specific assignment of the observed diatomic species between both metals. Also, it cannot be completely ruled out that the studied sample, between setting and freezing, was subjected to some internal decay processes resulting in a mixture of compound **A** and $\mathbf{P_{co}}$ state. However, this possible circumstance seems very unlikely for two reasons. Firstly, the set sample was kept consistently in a carbon monoxide atmosphere prior vitrification to prevent any oxidizing processes and secondly, a possible mixture of those two intermediate states would be clearly seen in the spectrum as the ferrous-oxy species (compound **A**) is clearly distinguishable due to its absorption behavior of the α-band at 595 nm (607 nm $\mathbf{P_{co}}$ state) [45, 46]. Unfortunately, to date “on grid” spectroscopic studies for cryo-EM is not feasible from a technical point of view. Methodological progress in this direction could allow a more comprehensive understanding of redox processes in bioenergetic enzymes. Nevertheless, just the presence and the first structural evidence of such a species in this intermediate state can be considered as an absolute novelty.

### 4.2.4 F state

In order to gain insight into the previously unknown ligand arrangement of the **F** state BNC and to get a better understanding of the transition between intermediate states in C*c*O, it was necessary to obtain the structure in a detailed level for this study. As outlined already above, the absence of the previously seen dioxygen species is apparent and replaced by a geometrically optimized oxoferryl group at the heme which agrees well with previous postulations [73]. The length of the ferryl $Fe^{4+} = O^{2-}$ bond was measured with a distance of 1.5 Å which is in well agreement with other studied iron-oxo complexes [103]. Ishigami *et al.* have claimed to found structural evidence for a **F** state species in their TR-SFX data set. However, it is more likely that this observed state reflects a mixed species as the double bond with a length of 1.9 Å is clearly too

long [73]. What was interesting to observe is the fact that there is no density of relevance in close proximity to $Cu_B$, which could indicate a possible OH or water group as a fourth ligand as commonly proposed. Even if there were a non-visible density at this spot, it seems questionable how it fits there geometrically considering the distance to the oxoferryl. The distance between each oxygen atom would be less than 2 Å which would be unrealistic considering the van der Waals radius of oxygen. Surprising was also the observation of a density corresponding to dioxygen species located between $His^{326.I}$ and $Val^{279.I}$ in close proximity to $Cu_B$ (3.3 Å). As postulated earlier by von der *Hocht et al.*, a superoxide at his position would make sense as this could transiently form a peroxide bridge after reduction has occurred. Exactly such a peroxide species is observed for the **O** state. Furthermore, the superoxide radical at this location is in agreement with complementary EPR and ligand-mimicking studies, which have shown that treatment of the **F** state C*c*O with catalase leads to the appearance of a tyrosine radical signal [69]. This observation can be explained if a superoxide present takes an electron from the C*c*O thus being converted to a peroxide that leaves the enzyme and is split by the catalase. Also, the increased crosslink distance with 2.7 Å for the **F** state in comparison to the $\mathbf{P_{CO}}$ state (1.6 Å) is presumably a result of a redox-coupled structural change leading to an altered crosslink behavior which is known to modify both the proton and electron affinities of the tyrosine [128, 129]. Moreover, the observation for the **F** state could possibly explain the drastic difference of the α-band in comparison to the **P** state as both states do not possess ferryl hemes.

Even though the structures of the intermediates seem relatively clear, the transition between these states raises questions. An essential question that emerges is how an oxoferryl group can be formed in the **F** state by the uptake of a single electron when a neutral dioxide is present in the **P** state. A possible explanation for this would be if, as postulated, a peroxide is present in the **P** state. Similarly, the transition from an **F** state species with an oxoferryl group and a superoxide would require input of two additional electrons to proceed to the **O** state. This is an argument in favor of the presence of a neutral dioxygen instead of a superoxide.

### 4.3 Oxygen diffusion channel

The density map of the **O** state allowed for the first time an accurate visualization of the oxygen channel due to its high resolution. As shown in section 3.7, a specific oxygen channel representing a unitary structure with its estimated length of 32 Å was identified. This can be considered as an important discovery as it was not necessarily clear whether such a specific channel responsible for oxygen diffusion is even existing. The identified oxygen channel starts at the protein-membrane interface at $Val^{42.I}$ of TMH1.I and $Leu^{149.I}$ of TMH3.I near the center of the lipid bilayer, where oxygen solubility is much higher than in the aqueous phase. The entry point of the identified channel is highlighted by a prominent cavity with a residing oxygen molecule. From that point on, a continuous wire of dioxygen molecules was identified. These molecules are in close range of hydrophobic amino acids, thereby facilitating the diffusion process towards the active site. Upon this finding, the performed computational assisted calculations by using MOLE 2.5 provided a deeper insight. The entire channel is embedded in a highly hydrophobic environment which is clearly indicative of a specific oxygen channel and shows a well-defined connection from the observed cavity at the interface of the transmembrane region to $Val^{279.I}$ at the binuclear site. This observation is consistent with the crystallographic noble gas binding studies of the $ba_3$ C*c*O from Luna *et al*. and the findings of Hofacker and Schulten based on molecular dynamic simulations [105, 130]. In this context, it should be mentioned that

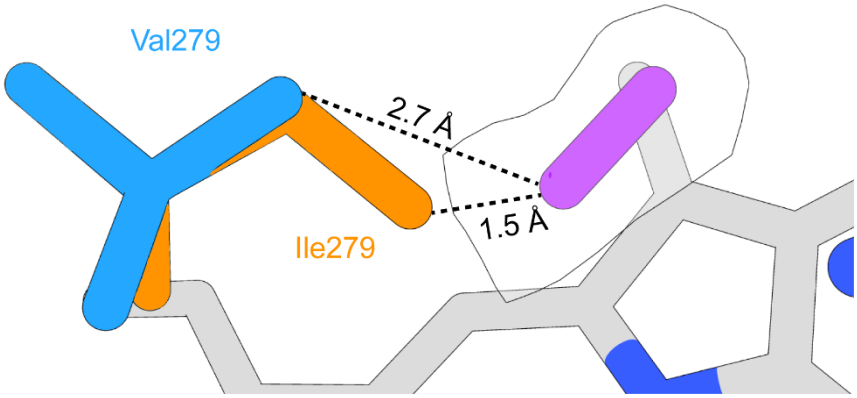


**Fig. 4.2**. **Replacement of Val279 to isoleucine at the binuclear center.** The longer sidechain of isoleucine protrudes into the observed oxygen channel and thus perturbs transport to the binding site. The molecular oxygen is shown in violet. The figure was prepared by using Chimera.

there is neither structural evidence of another oxygen pathway nor a possible division (Y-shape) of the channel itself as described by Luna *et al.* Furthermore, the site-directed mutagenesis experiments by Riistama *et al.* on $aa_3$-type C*c*O are an indirect confirmation for the structurally characterized oxygen pathway as the replacement of $Val^{279.I}$ to isoleucine resulted in a significantly higher $K_M$ for oxygen [131]. In the light of these structural insights, it appears reasonable to conclude that impairment of oxygen binding and reduction in the V279I mutant is caused by the introduced bulky residue at the end of this identified oxygen channel restricting access to the dioxygen reduction site (Fig.4.2). Interestingly, the shape and the length of the oxygen channel of the $aa_3$ cytochrome *c* oxidase resembles that of the *bd* oxidase from *E. coli*, which was recently identified. Although several previously undescribed water molecules were identified in relative proximity to the binuclear center, no specific water channel ("exit-pathway") leading away from the active site could be located. This can have several reasons. Considering the high resolutions of the respective density maps, lack of quality is not a logical explanation. It seems more logical that there are several channels through which the product (water) is transported to the soluble side.

## 5. Summary

The ability to obtain high-resolution, structural insights into the composition of cytochrome *c* oxidase using single-particle cryo-EM is a novelty. For a long time, cryo-EM did not appear to be a suitable method to study smaller (< 200 kDa), membrane-bound proteins and X-ray crystallography was the method of choice for decades. The rapid technical development of detectors and lens systems has revolutionized the field of structural biology - "the resolution revolution" – making it possible to achieve resolutions of 3-4 Å for smaller proteins.

Cytochrome *c* oxidase is a very extensive and extremely complex entity that has been attempted to be understood in its entirety for decades. The crystal structure in the 1990s made it possible to visualize the architecture of an $aa_3$-type cytochrome *c* oxidase for the first time. However, this was only the beginning of countless other questions concerning the complex process involved in the conversion of oxygen to water. Not only functional studies contribute to an essential part to the understanding of this complex, but also high-resolution structures in different biochemically defined states. The biggest advantage of cryo-EM over crystallography is that the method does not rely on homogenous, well-diffracting crystals, thus ensuring high reproducibility. This technical circumstance enabled this study to structurally elucidate different intermediate states of the C*c*O, which was previously nearly impossible using classical structural methods. The four generated structures of cytochrome *c* oxidase with an average resolution of 2.1 Å allowed detailed insights into the active site, the substrate binding site for molecular oxygen. The structures confirmed already suspected arrangements of oxygen molecules between the iron and copper center, such as a peroxide bridge in the **O** state or an oxoferryl in the **F** state. The two-electron reduced **P** state, as well as the three-electron reduced **F** state, whose structures are not yet available, showed unexpected structural arrangements in the binuclear center. In the **P** state, the presence of a homo nuclear molecule was identified, an oxygen species, contradicting previous postulates based on spectroscopic studies that suggested the presence of a single oxygen species. In the **F** state, the presence of a possible superoxide could be confirmed, which was already suspected based on EPR

and ligand mimicking studies. In addition, the high resolution of the **O** state allowed the identification of an oxygen channel, revealing a direct connection between the membrane side and the active site. Functional studies in recent years have suggested such an oxygen channel, but lacked any direct structural evidence. These structural data provide an excellent framework for further *in silico* calculations and may help to unravel the final mysteries of the cytochrome *c* oxidase.

# 6. Outlook

Although the cytochrome *c* oxidase has been studied intensively for many decades, more and more opportunities are emerging to better understand complex processes involved in the reduction of molecular oxygen to water using new methods.

In this study, four intermediates states of the $aa_3$ cytochrome c oxidase were structurally determined by cryo-EM. The structural content of these is of great importance as they allow further theoretical calculations to describe, for example, translocation processes of the proton channels more precisely. The higher the resolution of a structure, the more precisely side chains and water molecules can be assigned, whose exact positions are of great important for such types of calculations.

Since the confirmation of the respective intermediate states could only be done by uv/vis absorption spectroscopy, it would be desirable to be able to use another spectroscopic method to confirm the set states more accurately. A suitable method for this would be resonance Raman spectroscopy. Without question, it would be of great benefit to be able to spectroscopically examine the sample on the grid itself before recording the data for structure determination.

Now that the existence of an oxygen channel has been structurally proven and one has a much more accurate idea of the architecture, further point mutation studies would be of interest such as the entry point, localized between $Val^{42.I}$ and $Leu^{149.I}$ to see if oxygen uptake can be completely prevented. Also, the structure determinations of intermediates states in the reductive phase, for example the **E** state, would be of great interest, as there are no structural data on this either. One problem is that the samples have to be frozen anaerobically for measurement via cryo-EM. However, in view of advancing technical development, this will be gradually become possible, as has already been shown occasionally for metal complex proteins.

# 7. References


1. Brzezinski, P., *Redox-driven membrane-bound proton pumps.* Trends Biochem Sci, 2004. **29**(7): p. 380-7.
2. Wikstrom, M.K., *Proton pump coupled to cytochrome c oxidase in mitochondria.* Nature, 1977. **266**(5599): p. 271-3.
3. Brandt, U., *Energy converting NADH:quinone oxidoreductase (complex I).* Annu Rev Biochem, 2006. **75**: p. 69-92.
4. Cecchini, G., *Function and structure of complex II of the respiratory chain.* Annu Rev Biochem, 2003. **72**: p. 77-109.
5. Chandel, N.S., *Mitochondrial complex III: an essential component of universal oxygen sensing machinery?* Respir Physiol Neurobiol, 2010. **174**(3): p. 175-81.
6. Mulkidjanian, A.Y., et al., *Origin of first cells at terrestrial, anoxic geothermal fields.* Proc Natl Acad Sci U S A, 2012. **109**(14): p. E821-30.
7. Chelikani, P., I. Fita, and P.C. Loewen, *Diversity of structures and properties among catalases.* Cell Mol Life Sci, 2004. **61**(2): p. 192-208.
8. Landis, G.N. and J. Tower, *Superoxide dismutase evolution and life span regulation.* Mech Ageing Dev, 2005. **126**(3): p. 365-79.
9. Iwata, S., et al., *Structure at 2.8 A resolution of cytochrome c oxidase from Paracoccus denitrificans.* Nature, 1995. **376**(6542): p. 660-9.
10. Ostermeier, C., et al., *Structure at 2.7 A resolution of the Paracoccus denitrificans two-subunit cytochrome c oxidase complexed with an antibody FV fragment.* Proc Natl Acad Sci U S A, 1997. **94**(20): p. 10547-53.
11. Tsukihara, T., et al., *The whole structure of the 13-subunit oxidized cytochrome c oxidase at 2.8 A.* Science, 1996. **272**(5265): p. 1136-44.
12. Pinakoulaki, E., et al., *The protein effect in the structure of two ferryl-oxo intermediates at the same oxidation level in the heme copper binuclear center of cytochrome c oxidase.* J Biol Chem, 2013. **288**(28): p. 20261-6.
13. Abramson, J., et al., *The structure of the ubiquinol oxidase from Escherichia coli and its ubiquinone binding site.* Nat Struct Biol, 2000. **7**(10): p. 910-7.
14. Hendler, R.W., et al., *Comparison of energy-transducing capabilities of the two- and three-subunit cytochromes aa3 from Paracoccus denitrificans and the 13-subunit beef heart enzyme.* Biophys J, 1991. **60**(2): p. 415-23.
15. Witt, H. and B. Ludwig, *Isolation, analysis, and deletion of the gene coding for subunit IV of cytochrome c oxidase in Paracoccus denitrificans.* J Biol Chem, 1997. **272**(9): p. 5514-7.
16. Yoshikawa, S. and A. Shimada, *Reaction mechanism of cytochrome c oxidase.* Chem Rev, 2015. **115**(4): p. 1936-89.
17. Agmon, N., *The Grotthuss mechanism.* Chemical Physics Letters, 1995. **244**(5): p. 456-462.
18. Page, C.C., et al., *Natural engineering principles of electron tunnelling in biological oxidation-reduction.* Nature, 1999. **402**(6757): p. 47-52.
19. Fadda, E., N. Chakrabarti, and R. Pomes, *Acidity of a Cu-bound histidine in the binuclear center of cytochrome C oxidase.* J Phys Chem B, 2005. **109**(47): p. 22629-40.

20. Kaila, V.R., M.I. Verkhovsky, and M. Wikstrom, *Proton-coupled electron transfer in cytochrome oxidase.* Chem Rev, 2010. **110**(12): p. 7062-81.
21. Rieder, R. and H.R. Bosshard, *Comparison of the binding sites on cytochrome c for cytochrome c oxidase, cytochrome bc1, and cytochrome c1. Differential acetylation of lysyl residues in free and complexed cytochrome c.* J Biol Chem, 1980. **255**(10): p. 4732-9.
22. Antalis, T.M. and G. Palmer, *Kinetic characterization of the interaction between cytochrome oxidase and cytochrome c.* Journal of Biological Chemistry, 1982. **257**(11): p. 6194-6206.
23. Hill, B.C., *Modeling the sequence of electron transfer reactions in the single turnover of reduced, mammalian cytochrome c oxidase with oxygen.* J Biol Chem, 1994. **269**(4): p. 2419-25.
24. Northrup, S.H. and H.P. Erickson, *Kinetics of protein-protein association explained by Brownian dynamics computer simulation.* Proc Natl Acad Sci U S A, 1992. **89**(8): p. 3338-42.
25. Geren, L.M., et al., *Design of a ruthenium-cytochrome c derivative to measure electron transfer to the initial acceptor in cytochrome c oxidase.* J Biol Chem, 1995. **270**(6): p. 2466-72.
26. Konstantinov, A.A., et al., *The roles of the two proton input channels in cytochrome c oxidase from Rhodobacter sphaeroides probed by the effects of site-directed mutations on time-resolved electrogenic intraprotein proton transfer.* Proc Natl Acad Sci U S A, 1997. **94**(17): p. 9085-90.
27. Ruitenberg, M., et al., *Reduction of cytochrome c oxidase by a second electron leads to proton translocation.* Nature, 2002. **417**(6884): p. 99-102.
28. Moser, C.C., C.C. Page, and P.L. Dutton, *Darwin at the molecular scale: selection and variance in electron tunnelling proteins including cytochrome c oxidase.* Philos Trans R Soc Lond B Biol Sci, 2006. **361**(1472): p. 1295-305.
29. Oliveberg, M., P. Brzezinski, and B.G. Malmstrom, *The effect of pH and temperature on the reaction of fully reduced and mixed-valence cytochrome c oxidase with dioxygen.* Biochim Biophys Acta, 1989. **977**(3): p. 322-8.
30. Brzezinski, P., *Internal electron-transfer reactions in cytochrome c oxidase.* Biochemistry, 1996. **35**(18): p. 5611-5.
31. Verkhovsky, M.I., J.E. Morgan, and M. Wikstrom, *Control of electron delivery to the oxygen reduction site of cytochrome c oxidase: a role for protons.* Biochemistry, 1995. **34**(22): p. 7483-91.
32. Kaila, V.R., et al., *Interheme electron tunneling in cytochrome c oxidase.* Proc Natl Acad Sci U S A, 2010. **107**(50): p. 21470-5.
33. Hosler, J.P., et al., *Insight into the active-site structure and function of cytochrome oxidase by analysis of site-directed mutants of bacterial cytochrome aa3 and cytochrome bo.* J Bioenerg Biomembr, 1993. **25**(2): p. 121-36.
34. Pfitzner, U., et al., *Cytochrome c oxidase (heme aa3) from Paracoccus denitrificans: analysis of mutations in putative proton channels of subunit I.* J Bioenerg Biomembr, 1998. **30**(1): p. 89-97.
35. Pawate, A.S., et al., *A mutation in subunit I of cytochrome oxidase from Rhodobacter sphaeroides results in an increase in steady-state activity but completely eliminates proton pumping.* Biochemistry, 2002. **41**(45): p. 13417-23.
36. Henry, R.M., et al., *Functional hydration and conformational gating of proton uptake in cytochrome c oxidase.* J Mol Biol, 2009. **387**(5): p. 1165-85.

37. Adelroth, P., R.B. Gennis, and P. Brzezinski, *Role of the pathway through K(I-362) in proton transfer in cytochrome c oxidase from R. sphaeroides.* Biochemistry, 1998. **37**(8): p. 2470-6.
38. Vygodina, T.V., et al., *Mechanism of inhibition of electron transfer by amino acid replacement K362M in a proton channel of Rhodobacter sphaeroides cytochrome c oxidase.* Biochemistry, 1998. **37**(9): p. 3053-61.
39. Michel, H., *Cytochrome c oxidase: catalytic cycle and mechanisms of proton pumping--a discussion.* Biochemistry, 1999. **38**(46): p. 15129-40.
40. Moody, A.J., U. Brandt, and P.R. Rich, *Single electron reduction of 'slow' and 'fast' cytochrome-c oxidase.* FEBS Lett, 1991. **293**(1-2): p. 101-5.
41. Oliveberg, M. and B.G. Malmstrom, *Internal electron transfer in cytochrome c oxidase: evidence for a rapid equilibrium between cytochrome a and the bimetallic site.* Biochemistry, 1991. **30**(29): p. 7053-7.
42. Blackmore, R.S., C. Greenwood, and Q.H. Gibson, *Studies of the primary oxygen intermediate in the reaction of fully reduced cytochrome oxidase.* J Biol Chem, 1991. **266**(29): p. 19245-9.
43. Woodruff, W.H., et al., *Nature and functional implications of the cytochrome a3 transients after photodissociation of CO-cytochrome oxidase.* Proc Natl Acad Sci U S A, 1991. **88**(6): p. 2588-92.
44. Bailey, J.A., C.A. James, and W.H. Woodruff, *Flow-flash kinetics of O2 binding to cytochrome c oxidase at elevated [O2]: observations using high pressure stopped flow for gaseous reactants.* Biochem Biophys Res Commun, 1996. **220**(3): p. 1055-60.
45. Chance, B., C. Saronio, and J.S. Leigh, Jr., *Functional intermediates in the reaction of membrane-bound cytochrome oxidase with oxygen.* J Biol Chem, 1975. **250**(24): p. 9226-37.
46. Hill, B.C. and C. Greenwood, *Spectroscopic evidence for the participation of compound A (Fea32+-O2) in the reaction of mixed-valence cytochrome c oxidase with oxygen at room temperature.* Biochem J, 1983. **215**(3): p. 659-67.
47. Varotsis, C., W.H. Woodruff, and G.T. Babcock, *Time-resolved Raman detection of .mu.(Fe-O) in an early intermediate in the reduction of oxygen by cytochrome oxidase [Erratum to document cited in CA111(9):73737r].* Journal of the American Chemical Society, 1990. **112**(3): p. 1297-1297.
48. Verkhovsky, M.I., et al., *The "ferrous-oxy" intermediate in the reaction of dioxygen with fully reduced cytochromes aa3 and bo3.* Biochemistry, 1996. **35**(50): p. 16241-6.
49. Verkhovsky, M.I., et al., *Kinetic trapping of oxygen in cell respiration.* Nature, 1996. **380**(6571): p. 268-70.
50. Verkhovsky, M.I., J.E. Morgan, and M. Wikstrom, *Oxygen binding and activation: early steps in the reaction of oxygen with cytochrome c oxidase.* Biochemistry, 1994. **33**(10): p. 3079-86.
51. Varotsis, C., et al., *Resolution of the reaction sequence during the reduction of O2 by cytochrome oxidase.* Proc Natl Acad Sci U S A, 1993. **90**(1): p. 237-41.
52. Hill, B.C. and C. Greenwood, *The reaction of fully reduced cytochrome c oxidase with oxygen studied by flow-flash spectrophotometry at room temperature. Evidence for new pathways of electron transfer.* Biochem J, 1984. **218**(3): p. 913-21.
53. Proshlyakov, D.A., et al., *Selective resonance Raman observation of the "607 nm" form generated in the reaction of oxidized cytochrome c oxidase with hydrogen peroxide.* J Biol Chem, 1994. **269**(47): p. 29385-8.

54. Morgan, J.E., et al., *Identification of a "peroxy" intermediate in cytochrome bo3 of Escherichia coli.* Biochemistry, 1995. **34**(48): p. 15633-7.
55. Hirota, S., et al., *Observation of the Fe-O2 and FeIV=O stretching Raman bands for dioxygen reduction intermediates of cytochrome bo isolated from Escherichia coli.* FEBS Lett, 1994. **352**(1): p. 67-70.
56. Kitagawa, T. and T. Ogura, *Oxygen Activation Mechanism at the Binuclear Site of Heme–Copper Oxidase Superfamily as Revealed by Time-Resolved Resonance Raman Spectroscopy.* Progress in Inorganic Chemistry, 1996: p. 431-479.
57. Watmough, N.J., et al., *Cytochrome bo from Escherichia coli: reaction of the oxidized enzyme with hydrogen peroxide.* Biochem J, 1994. **300 ( Pt 2)**: p. 469-75.
58. Fabian, M. and G. Palmer, *The interaction of cytochrome oxidase with hydrogen peroxide: the relationship of compounds P and F.* Biochemistry, 1995. **34**(42): p. 13802-10.
59. Ogura, T., et al., *Time-Resolved Resonance Raman Evidence for Tight Coupling between Electron Transfer and Proton Pumping of Cytochrome c Oxidase upon the Change from the FeV Oxidation Level to the FeIV Oxidation Level.* Journal of the American Chemical Society, 1996. **118**(23): p. 5443-5449.
60. Michel, H., et al., *Cytochrome c oxidase: structure and spectroscopy.* Annu Rev Biophys Biomol Struct, 1998. **27**: p. 329-56.
61. Han, S., Y.C. Ching, and D.L. Rousseau, *Ferryl and hydroxy intermediates in the reaction of oxygen with reduced cytochrome c oxidase.* Nature, 1990. **348**(6296): p. 89-90.
62. Morgan, J.E., et al., *Role of the PR intermediate in the reaction of cytochrome c oxidase with O2.* Biochemistry, 2001. **40**(23): p. 6882-92.
63. Ogura, T., et al., *Observation of the Fe4+ = O stretching Raman band for cytochrome oxidase compound B at ambient temperature.* J Biol Chem, 1990. **265**(25): p. 14721-3.
64. Varotsis, C. and G.T. Babcock, *Appearance of the v(FeIV = O) vibration from a ferryl-oxo intermediate in the cytochrome oxidase/dioxygen reaction.* Biochemistry, 1990. **29**(32): p. 7357-62.
65. Wikstrom, M., *Energy-dependent reversal of the cytochrome oxidase reaction.* Proc Natl Acad Sci U S A, 1981. **78**(7): p. 4051-4.
66. Witt, S.N., D.F. Blair, and S.I. Chan, *Chemical and spectroscopic evidence for the formation of a ferryl Fea3 intermediate during turnover of cytochrome c oxidase.* J Biol Chem, 1986. **261**(18): p. 8104-7.
67. Morgan, J.E., M.I. Verkhovsky, and M. Wikstrom, *Observation and assignment of peroxy and ferryl intermediates in the reduction of dioxygen to water by cytochrome c oxidase.* Biochemistry, 1996. **35**(38): p. 12235-40.
68. Moody, A.J. and P.R. Rich, *The reaction of hydrogen peroxide with pulsed cytochrome bo from Escherichia coli.* Eur J Biochem, 1994. **226**(2): p. 731-7.
69. von der Hocht, I., et al., *Interconversions of P and F intermediates of cytochrome c oxidase from Paracoccus denitrificans.* Proc Natl Acad Sci U S A, 2011. **108**(10): p. 3964-9.
70. Han, S., S. Takahashi, and D.L. Rousseau, *Time Dependence of the Catalytic Intermediates in Cytochromec Oxidase*.* Journal of Biological Chemistry, 2000. **275**(3): p. 1910-1919.
71. Koepke, J., et al., *High resolution crystal structure of Paracoccus denitrificans cytochrome c oxidase: New insights into the active site and the proton transfer*

*pathways.* Biochimica et Biophysica Acta (BBA) - Bioenergetics, 2009. **1787**(6): p. 635-645.
72. Muramoto, K., et al., *Bovine cytochrome c oxidase structures enable O2 reduction with minimization of reactive oxygens and provide a proton-pumping gate.* Proc Natl Acad Sci U S A, 2010. **107**(17): p. 7740-5.
73. Ishigami, I., et al., *Snapshot of an oxygen intermediate in the catalytic reaction of cytochrome c oxidase.* Proc Natl Acad Sci U S A, 2019. **116**(9): p. 3572-3577.
74. Yip, K.M., et al., *Atomic-resolution protein structure determination by cryo-EM.* Nature, 2020.
75. Gerhus, E., P. Steinrucke, and B. Ludwig, *Paracoccus denitrificans cytochrome c1 gene replacement mutants.* J Bacteriol, 1990. **172**(5): p. 2392-400.
76. Hilbers, F., et al., *True wild type and recombinant wild type cytochrome c oxidase from Paracoccus denitrificans show a 20-fold difference in their catalase activity.* Biochim Biophys Acta, 2013. **1827**(3): p. 319-27.
77. Kleymann, G., et al., *Engineered Fv fragments as a tool for the one-step purification of integral multisubunit membrane protein complexes.* Biotechnology (N Y), 1995. **13**(2): p. 155-60.
78. Essen, L.O., et al., *1.3 A X-ray structure of an antibody Fv fragment used for induced membrane-protein crystallization.* Acta Crystallogr D Biol Crystallogr, 2003. **59**(Pt 4): p. 677-87.
79. Ritchie, T.K., et al., *Chapter 11 - Reconstitution of membrane proteins in phospholipid bilayer nanodiscs.* Methods Enzymol, 2009. **464**: p. 211-31.
80. Frazier, A.E. and D.R. Thorburn, *Biochemical analyses of the electron transport chain complexes by spectrophotometry.* Methods Mol Biol, 2012. **837**: p. 49-62.
81. Kuhlbrandt, W., *Biochemistry. The resolution revolution.* Science, 2014. **343**(6178): p. 1443-4.
82. Wang, H.W. and J.W. Wang, *How cryo-electron microscopy and X-ray crystallography complement each other.* Protein Sci, 2017. **26**(1): p. 32-39.
83. Zheng, S.Q., et al., *MotionCor2: anisotropic correction of beam-induced motion for improved cryo-electron microscopy.* Nat Methods, 2017. **14**(4): p. 331-332.
84. Zivanov, J., et al., *New tools for automated high-resolution cryo-EM structure determination in RELION-3.* Elife, 2018. **7**.
85. Zivanov, J., T. Nakane, and S.H.W. Scheres, *Estimation of high-order aberrations and anisotropic magnification from cryo-EM data sets in RELION-3.1.* IUCrJ, 2020. **7**(Pt 2): p. 253-267.
86. Rohou, A. and N. Grigorieff, *CTFFIND4: Fast and accurate defocus estimation from electron micrographs.* J Struct Biol, 2015. **192**(2): p. 216-21.
87. Terwilliger, T.C., et al., *Improvement of cryo-EM maps by density modification.* Nat Methods, 2020. **17**(9): p. 923-927.
88. Harrenga, A. and H. Michel, *The cytochrome c oxidase from Paracoccus denitrificans does not change the metal center ligation upon reduction.* J Biol Chem, 1999. **274**(47): p. 33296-9.
89. Liebschner, D., et al., *Macromolecular structure determination using X-rays, neutrons and electrons: recent developments in Phenix.* Acta Crystallogr D Struct Biol, 2019. **75**(Pt 10): p. 861-877.
90. Emsley, P., et al., *Features and development of Coot.* Acta Crystallogr D Biol Crystallogr, 2010. **66**(Pt 4): p. 486-501.

91. Chen, V.B., et al., *MolProbity: all-atom structure validation for macromolecular crystallography.* Acta Crystallogr D Biol Crystallogr, 2010. **66**(Pt 1): p. 12-21.
92. Pettersen, E.F., et al., *UCSF Chimera--a visualization system for exploratory research and analysis.* J Comput Chem, 2004. **25**(13): p. 1605-12.
93. Goddard, T.D., et al., *UCSF ChimeraX: Meeting modern challenges in visualization and analysis.* Protein Sci, 2018. **27**(1): p. 14-25.
94. Pravda, L., et al., *MOLEonline: a web-based tool for analyzing channels, tunnels and pores (2018 update).* Nucleic Acids Res, 2018. **46**(W1): p. W368-W373.
95. Wikstrom, M. and J.E. Morgan, *The dioxygen cycle. Spectral, kinetic, and thermodynamic characteristics of ferryl and peroxy intermediates observed by reversal of the cytochrome oxidase reaction.* J Biol Chem, 1992. **267**(15): p. 10266-73.
96. Punjani, A., et al., *cryoSPARC: algorithms for rapid unsupervised cryo-EM structure determination.* Nat Methods, 2017. **14**(3): p. 290-296.
97. van Heel, M. and M. Schatz, *Fourier shell correlation threshold criteria.* J Struct Biol, 2005. **151**(3): p. 250-62.
98. Scheres, S.H., *RELION: implementation of a Bayesian approach to cryo-EM structure determination.* J Struct Biol, 2012. **180**(3): p. 519-30.
99. Groom, C.R., et al., *The Cambridge Structural Database.* Acta Crystallogr B Struct Sci Cryst Eng Mater, 2016. **72**(Pt 2): p. 171-9.
100. Glaeser, R.M., et al., *Factors that Influence the Formation and Stability of Thin, Cryo-EM Specimens.* Biophys J, 2016. **110**(4): p. 749-55.
101. Yoshikawa, S., et al., *Redox-coupled crystal structural changes in bovine heart cytochrome c oxidase.* Science, 1998. **280**(5370): p. 1723-9.
102. Wikstrom, M., K. Krab, and V. Sharma, *Oxygen Activation and Energy Conservation by Cytochrome c Oxidase.* Chem Rev, 2018. **118**(5): p. 2469-2490.
103. Hohenberger, J., K. Ray, and K. Meyer, *The biology and chemistry of high-valent iron-oxo and iron-nitrido complexes.* Nat Commun, 2012. **3**: p. 720.
104. Riistama, S., et al., *Channelling of dioxygen into the respiratory enzyme.* Biochimica et Biophysica Acta (BBA) - Bioenergetics, 1996. **1275**(1): p. 1-4.
105. Luna, V.M., et al., *Crystallographic studies of Xe and Kr binding within the large internal cavity of cytochrome ba3 from Thermus thermophilus: structural analysis and role of oxygen transport channels in the heme-Cu oxidases.* Biochemistry, 2008. **47**(16): p. 4657-65.
106. Safarian, S., et al., *Active site rearrangement and structural divergence in prokaryotic respiratory oxidases.* Science, 2019. **366**(6461): p. 100-104.
107. Reidelbach, M. and P. Imhof, *Proton transfer in the D-channel of cytochrome c oxidase modeled by a transition network approach.* Biochim Biophys Acta Gen Subj, 2020. **1864**(8): p. 129614.
108. Marques, M.A., M.D. Purdy, and M. Yeager, *CryoEM maps are full of potential.* Curr Opin Struct Biol, 2019. **58**: p. 214-223.
109. Riegler, D., et al., *Characterization of steady-state activities of cytochrome c oxidase at alkaline pH: mimicking the effect of K-channel mutations in the bovine enzyme.* Biochim Biophys Acta, 2005. **1706**(1-2): p. 126-33.
110. Lepp, H., et al., *Charge transfer in the K proton pathway linked to electron transfer to the catalytic site in cytochrome c oxidase.* Biochemistry, 2008. **47**(17): p. 4929-35.

111. Supekar, S. and V.R.I. Kaila, *Dewetting transitions coupled to K-channel activation in cytochrome c oxidase.* Chem Sci, 2018. **9**(32): p. 6703-6710.
112. Wilson, M.T., et al., *A plausible two-state model for cytochrome c oxidase.* Proc Natl Acad Sci U S A, 1981. **78**(11): p. 7115-8.
113. Bloch, D., et al., *The catalytic cycle of cytochrome c oxidase is not the sum of its two halves.* Proc Natl Acad Sci U S A, 2004. **101**(2): p. 529-33.
114. Belevich, I., et al., *Exploring the proton pump mechanism of cytochrome c oxidase in real time.* Proc Natl Acad Sci U S A, 2007. **104**(8): p. 2685-90.
115. Vilhjalmsdottir, J., R.B. Gennis, and P. Brzezinski, *The electron distribution in the "activated" state of cytochrome c oxidase.* Sci Rep, 2018. **8**(1): p. 7502.
116. Blomberg, M.R.A., *The structure of the oxidized state of cytochrome c oxidase - experiments and theory compared.* J Inorg Biochem, 2020. **206**: p. 111020.
117. Karpefors, M., et al., *Formation of the "peroxy" intermediate in cytochrome c oxidase is associated with internal proton/hydrogen transfer.* Biochemistry, 2000. **39**(47): p. 14664-9.
118. Verkhovsky, M.I., et al., *Translocation of electrical charge during a single turnover of cytochrome-c oxidase.* Biochimica et Biophysica Acta (BBA) - Bioenergetics, 1997. **1318**(1): p. 6-10.
119. Oliveberg, M. and B.G. Malmstrom, *Reaction of dioxygen with cytochrome c oxidase reduced to different degrees: indications of a transient dioxygen complex with copper-B.* Biochemistry, 1992. **31**(14): p. 3560-3.
120. Fann, Y.C., et al., *Structure of CuB in the binuclear heme-copper center of the cytochrome aa3-type quinol oxidase from Bacillus subtilis: an ENDOR and EXAFS study.* Biochemistry, 1995. **34**(32): p. 10245-55.
121. Kaila, V.R., et al., *A combined quantum chemical and crystallographic study on the oxidized binuclear center of cytochrome c oxidase.* Biochim Biophys Acta, 2011. **1807**(7): p. 769-78.
122. Andersson, R., et al., *Serial femtosecond crystallography structure of cytochrome c oxidase at room temperature.* Sci Rep, 2017. **7**(1): p. 4518.
123. Sun, C., et al., *Structure of the alternative complex III in a supercomplex with cytochrome oxidase.* Nature, 2018. **557**(7703): p. 123-126.
124. Qin, L., et al., *Redox-dependent conformational changes in cytochrome C oxidase suggest a gating mechanism for proton uptake.* Biochemistry, 2009. **48**(23): p. 5121-30.
125. Babcock, G.T., *How oxygen is activated and reduced in respiration.* Proc Natl Acad Sci U S A, 1999. **96**(23): p. 12971-3.
126. Ferguson-Miller, S. and G.T. Babcock, *Heme/Copper Terminal Oxidases.* Chem Rev, 1996. **96**(7): p. 2889-2908.
127. Fabian, M., et al., *Mass spectrometric determination of dioxygen bond splitting in the "peroxy" intermediate of cytochrome c oxidase.* Proc Natl Acad Sci U S A, 1999. **96**(23): p. 13114-7.
128. Buse, G., et al., *Evidence for a copper-coordinated histidine-tyrosine cross-link in the active site of cytochrome oxidase.* Protein Sci, 1999. **8**(5): p. 985-90.
129. Kaila, V.R., et al., *The chemistry of the CuB site in cytochrome c oxidase and the importance of its unique His-Tyr bond.* Biochim Biophys Acta, 2009. **1787**(4): p. 221-33.
130. Hofacker, I. and K. Schulten, *Oxygen and proton pathways in cytochrome c oxidase.* Proteins, 1998. **30**(1): p. 100-7.

131. Riistama, S., et al., *Binding of O(2) and its reduction are both retarded by replacement of valine 279 by isoleucine in cytochrome c oxidase from Paracoccus denitrificans.* Biochemistry, 2000. **39**(21): p. 6365-72.

## 8. Appendix

*Paracoccus denitrificans* - Cytochrome c oxidase subunit 1 – ctaDII

```
        10         20         30         40         50
MADAAVHGHG DHHDTRGFFT RWFMSTNHKD IGILYLFTAG IVGLISVCFT
        60         70         80         90        100
VYMRMELQHP GVQYMCLEGA RLIADASAEC TPNGHLWNVM ITYHGVLMMF
       110        120        130        140        150
FVVIPALFGG FGNYFMPLHI GAPDMAFPRL NNLSYWMYVC GVALGVASLL
       160        170        180        190        200
APGGNDQMGS GVGWVLYPPL STTEAGYSMD LAIFAVHVSG ASSILGAINI
       210        220        230        240        250
ITTFLNMRAP GMTLFKVPLF AWSVFITAWL ILLSLPVLAG AITMLLMDRN
       260        270        280        290        300
FGTQFFDPAG GGDPVLYQHI LWFFGHPEVY IIILPGFGII SHVISTFAKK
       310        320        330        340        350
PIFGYLPMVL AMAAIGILGF VVWAHHMYTA GMSLTQQAYF MLATMTIAVP
       360        370        380        390        400
TGIKVFSWIA TMWGGSIEFK TPMLWAFGFL FLFTVGGVTG VVLSQAPLDR
       410        420        430        440        450
VYHDTYYVVA HFHYVMSLGA VFGIFAGVYY WIGKMSGRQY PEWAGQLHFW
       460        470        480        490        500
MMFIGSNLIF FPQHFLGRQG MPRRYIDYPV EFAYWNNISS IGAYISFASF
       510        520        530        540        550
LFFIGIVFYT LFAGKRVNVP NYWNEHADTL EWTLPSPPPE HTFETLPKRE

DWDRAHAH
```

*Paracoccus denitrificans* - Cytochrome c oxidase subunit 2 – ctaC

```
        10         20         30         40         50
MMAIATKRRG VAAVMSLGVA TMTAVPALAQ DVLGDLPVIG KPVNGGMNFQ
        60         70         80         90        100
PASSPLAHDQ QWLDHFVLYI ITAVTIFVCL LLLICIVRFN RRANPVPARF
       110        120        130        140        150
THNTPIEVIW TLVPVLILVA IGAFSLPILF RSQEMPNDPD LVIKAIGHQW
       160        170        180        190        200
YWSYEYPNDG VAFDALMLEK EALADAGYSE DEYLLATDNP VVVPVGKKVL
       210        220        230        240        250
VQVTATDVIH AWTIPAFAVK QDAVPGRIAQ LWFSVDQEGV YFGQCSELCG
       260        270        280        290
INHAYMPIVV KAVSQEKYEA WLAGAKEEFA ADASDYLPAS PVKLASAE
```

*Paracoccus denitrificans* - Cytochrome c oxidase subunit 3 – ctaE

```
        10         20         30         40         50
MAHVKNHDYQ ILPPSIWPFF GAIGAFVMLT GAVAWMKGIT FFGLPVEGPW
        60         70         80         90        100
MFLIGLVGVL YVMFGWWADV VNEGETGEHT PVVRIGLQYG FILFIMSEVM
       110        120        130        140        150
FFVAWFWAFI KNALYPMGPD SPIKDGVWPP EGIVTFDPWH LPLINTLILL
       160        170        180        190        200
LSGVAVTWAH HAFVLEGDRK TTINGLIVAV ILGVCFTGLQ AYEYSHAAFG
       210        220        230        240        250
LADTVYAGAF YMATGFHGAH VIIGTIFLFV CLIRLLKGQM TQKQHVGFEA
       260        270
AAWYWHFVDV VWLFLFVVIY IWGR
```

*Paracoccus denitrificans* - Cytochrome c oxidase subunit 4 – ctaH

```
        10         20         30         40         50
MASHHEITDH KHGEMDIRHQ QATFAGFIKG ATWVSILSIA VLVFLALANS
```

## Strains

| ***Strain*** | ***genotype*** | ***reference*** |
|---|---|---|
| ***E. coli* JM83** | F$^-$*ara* Δ(*lac-proAB*) *rpsL* (Str$^r$) *thi* Φ80dΔ(lacZ)*M15* | Grodberg, 1988 |
| ***E. coli Bl21-Gold(DE3)*** | B F$^-$ *ampT hsdS*($r_B^-$ $m_B^-$) *dcm*$^+$ Tet$^r$ gal λ(DE3) *endA Hte* | Weiner, 1994 |
| ***E. coli* RP4-4** | RP-derivative in J53 with Amp$^r$, Tet$^r$, Km$^r$ | O. Richter, University of Frankfurt, Frankfurt Main, Germany |
| ***P. denitrificans* AO1** | PD1222 derivative, ΔctaDI::Km$^R$, ΔctaDII::Tet$^r$. ΔccON::Gm$^r$, Rif$^r$ | Pfitzner, 1998 |

## Plasmids

| ***plasmid*** | ***properties*** | ***reference*** |
|---|---|---|
| **pASK68** | *Amp$^r$, laclm f1IG, lac$^{p/o}$ompA-($V_H$)-strep, phoA-($V_L$)-myc* | Kleymann, 1995 |
| **pUB39** | pBBR1 MCS derivative Sm$^r$, Kn$^r$, ctaC2-Promoter *KpnI/XbaI, ctaDII XbaI/HindIII* | Kovach, 1994 Pfitzner |
| ***p*MSP1D1** | *Kan$^r$, laclR,f1ori-F, phoA-($V_L$)-myc, HindIII, Nco I* | Denisov, 2004 |

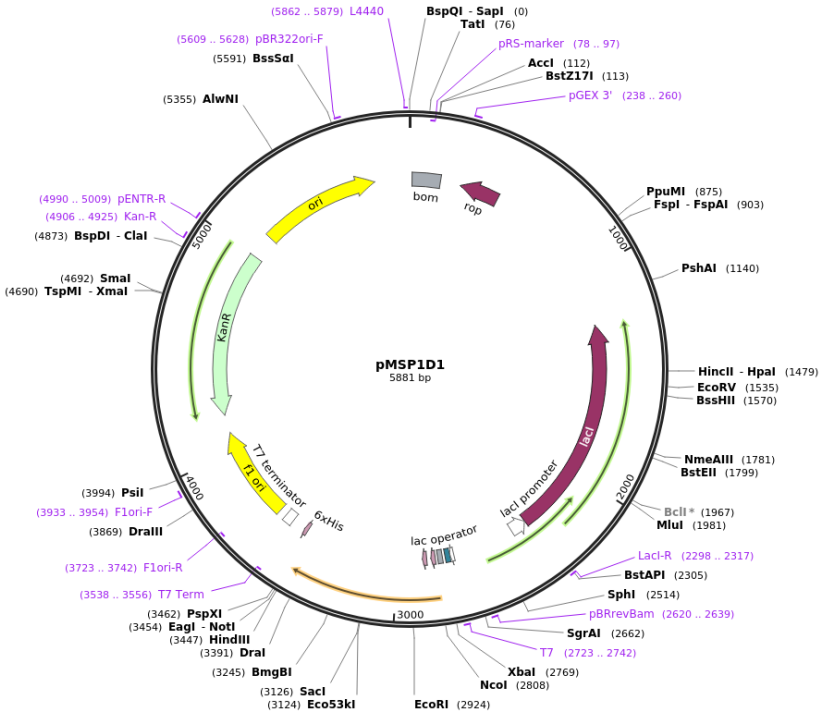
Created with SnapGene®
pMSP1D1
5881 bp
(5862 .. 5879) L4440
BspQI - SapI (0)
TatI (76)
(5609 .. 5628) pBR322ori-F
pRS-marker (78 .. 97)
(5591) BssSαI
AccI (112)
BstZ17I (113)
pGEX 3' (238 .. 260)
(5355) AlwNI
PpuMI (875)
FspI - FspAI (903)
PshAI (1140)
HincII - HpaI (1479)
EcoRV (1535)
BssHII (1570)
NmeAIII (1781)
BstEII (1799)
BclI * (1967)
MluI (1981)
LacI-R (2298 .. 2317)
BstAPI (2305)
SphI (2514)
pBRrevBam (2620 .. 2639)
SgrAI (2662)
T7 (2723 .. 2742)
XbaI (2769)
NcoI (2808)
EcoRI (2924)
(3124) Eco53kI
(3126) SacI
(3245) BmgBI
(3391) DraI
(3447) HindIII
(3454) EagI - NotI
(3462) PspXI
(3538 .. 3556) T7 Term
(3723 .. 3742) F1ori-R
(3869) DraIII
(3933 .. 3954) F1ori-F
(3994) PsiI
(4692) SmaI
(4690) TspMI - XmaI
(4873) BspDI - ClaI
(4906 .. 4925) Kan-R
(4990 .. 5009) pENTR-R
ori
bom
rop
KanR
T7 terminator
f1 ori
6xHis
lac operator
lacI promoter
lacI
1000
2000
3000
4000
5000

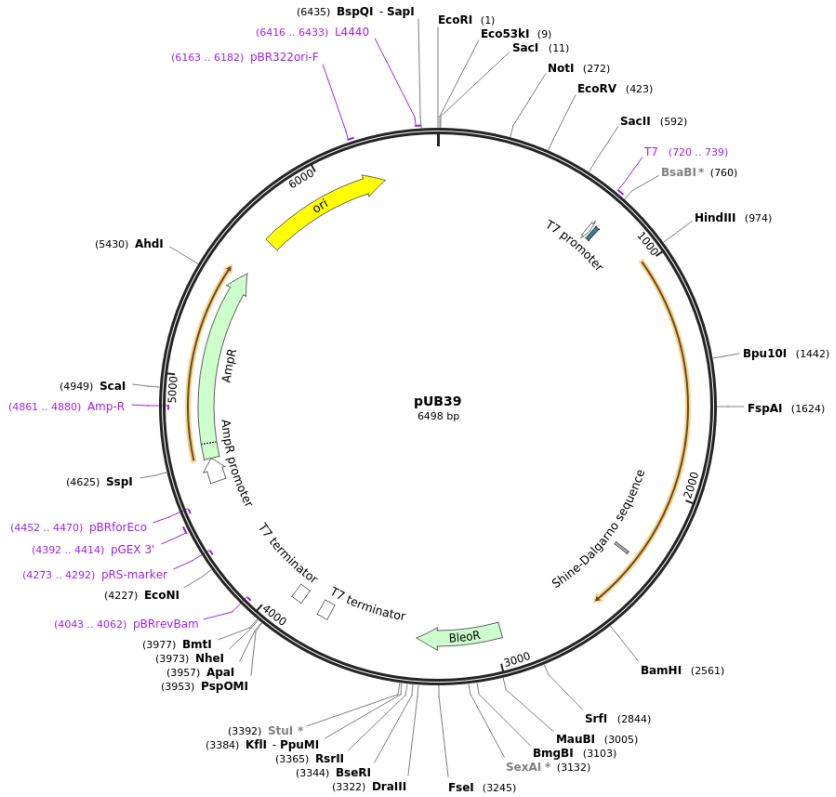
Created with SnapGene®
pUB39
6498 bp
(6435) BspQI - SapI
EcoRI (1)
Eco53kI (9)
SacI (11)
NotI (272)
EcoRV (423)
SacII (592)
T7 (720 .. 739)
BsaBI * (760)
HindIII (974)
Bpu10I (1442)
FspAI (1624)
BamHI (2561)
SrfI (2844)
MauBI (3005)
BmgBI (3103)
SexAI * (3132)
FseI (3245)
(3322) DraIII
(3344) BseRI
(3365) RsrII
(3384) KflI - PpuMI
(3392) StuI *
(3953) PspOMI
(3957) ApaI
(3973) NheI
(3977) BmtI
(4043 .. 4062) pBRrevBam
(4227) EcoNI
(4273 .. 4292) pRS-marker
(4392 .. 4414) pGEX 3'
(4452 .. 4470) pBRforEco
(4625) SspI
(4861 .. 4880) Amp-R
(4949) ScaI
(5430) AhdI
(6163 .. 6182) pBR322ori-F
(6416 .. 6433) L4440
ori
AmpR
AmpR promoter
T7 terminator
T7 terminator
BleoR
T7 promoter
Shine-Dalgarno sequence
1000
2000
3000
4000
5000
6000

# Copyright permission license for Figure 2.1

Order Completed

Thank you for your order.

This Agreement between Felix Kolbe ("You") and John Wiley and Sons ("John Wiley and Sons") consists of your order details and the terms and conditions provided by John Wiley and Sons and Copyright Clearance Center.

| | |
|---|---|
| License number | Reference confirmation email for license number |
| License date | Feb, 22 2022 |

### Licensed Content

| | |
|---|---|
| Licensed Content Publisher | John Wiley and Sons |
| Licensed Content Publication | Protein Science |
| Licensed Content Title | How cryo-electron microscopy and X-ray crystallography complement each other |
| Licensed Content Author | Jia-Wei Wang, Hong-Wei Wang |
| Licensed Content Date | 07.09.2016 |
| Licensed Content Volume | 26 |
| Licensed Content Issue | 1 |
| Licensed Content Pages | 8 |

### Order Details

| | |
|---|---|
| Type of use | Dissertation/Thesis |
| Requestor type | University/Academic |
| Format | Print |
| Portion | Figure/table |
| Number of figures/tables | 1 |
| Will you be translating? | No |

### About Your Work

| | |
|---|---|
| Title | Structural insights into the catalytic binuclear center of cytochrome c oxidase from Paracoccus denitrificans |
| Institution name | Max Planck Institute for Biophysics |
| Expected presentation date | Feb 2022 |

### Additional Data

| | |
|---|---|
| Portions | Figure 1 |

### Requestor Location

| | |
|---|---|
| Requestor Location | Max Planck Society<br>Max von Laue Str. 3<br><br>Frankfurt, 60438<br>Germany<br>Attn: Max Planck Society |

### Tax Details

| | |
|---|---|
| Publisher Tax ID | EU826007151 |

### Billing Information

| | |
|---|---|
| Billing Type | Invoice |
| Billing address | Max Planck Society<br>Max von Laue Str. 3<br><br>Frankfurt, Germany 60438<br>Attn: Max Planck Society |

### $ Price

| | |
|---|---|
| Total | 0.00 EUR |

## 9. Deutschsprachige Zusammenfassung

Die Cytochrom-*c*-Oxidase, lokalisiert als terminales Enzym in der Atmungskette in Mitochondrien und vielen aeroben Bakterien, katalysiert die Elektronenübertragung von Cytochrom *c* auf molekularen Sauerstoff, wodurch die Reduktion zu Wasser ermöglicht wird. Die Cytochrom-*c*-Oxidase ist eine Oxidoreduktase, welche üblicherweise auch Komplex IV genannt wird. Sie gehört aufgrund der Beschaffung zur Superfamilie der Häm-Kupfer-Oxidasen. Annäherungsweise werden rund 90 % des von lebenden Organismen verbrauchten Sauerstoffs von Enzymen dieser Art umgesetzt, wodurch dieses Membranprotein mit seiner Funktion als eines der wichtigsten Proteine im biologischen Kontext überhaupt gilt. Die Übertragung der Elektronen von Cytochrom *c* auf molekularen Sauerstoff ist eine exergone Redoxreaktion, die energetisch an den Aufbau eines elektrochemischen Protonengradienten gekoppelt ist. Hierbei werden die Elektronen von Cytochrom *c* aus dem Intermembranraum aufgenommen, die Substratprotonen hingegen werden aus der mitochondrialen Matrix bzw. dem bakteriellen Cytoplasma zur Verfügung gestellt. Zusätzlich zu diesem elektrogenen Prozess werden Protonen über die Membran transloziert, ein Vorgang, der als Protonenpumpprozess bezeichnet wird. Damit ergibt sich folgende Nettoreaktion:

$$4\ \text{cyt}\ c^{2+} + O_2 + 8\ H^+_{\text{innen}} \rightarrow 4\ \text{cyt}\ c^{3+} + 2\ H_2O + 4\ H^+_{\text{außen}}$$

Der dabei entstehende elektrochemische Gradient wird von der $F_oF_1$-ATP-Synthase dazu verwendet, Adenosin-5´-Triphosphat (ATP) aus Adenosin-5´-Diphosphat (ADP) und anorganischem Phosphat ($P_i$) zu synthetisieren, ein essentielles Nukleotid, das als Energieträger in Zellen fungiert. Bei der Übertragung der Elektronen von Cytochrom *c* auf molekularen Sauerstoff sind vier verschiedene Metallzentren von essentieller Bedeutung. Dies sind zwei Kupferkomplexe $Cu_A$ und $Cu_B$ sowie zwei Häme, Häm $a$ und Häm $a_3$. Das Substrat, in dem Falle molekularer Sauerstoff, wird während der Reaktion im sogenannten binuklearen Zentrum gebunden, welches sich aus Häm $a_3$ und $Cu_B$ zusammensetzt. Dies dient dem primären Zweck, die Freisetzung von hochreaktiven Oxoverbindungen (z.B. Radikale) zu verhindern, die auf zellulärer Basis toxisch wirken und zu unkontrollierter Zellschädigung führen

können. Der Reduktionsvorgang von Sauerstoff zu Wasser erfolgt über mehrere Schritte. Seine Funktionsweise ist hochkomplex ist und bis heute nicht genau aufgeklärt und somit immer noch Gegenstand von aktuellen Forschungen bzw. der Grundlagenforschung. Die Reduktion von Sauerstoff erfolgt über Zwischenzustände, welche schon bereits vor mehreren Jahrzehnten spektroskopisch charakterisiert wurden.

Ende der 90er Jahre konnte die erste, dreidimensionale röntgenkristallographische Struktur einer Cytochrom-*c*-Oxidase ermittelt werden, die strukturellen Einblicke in die Beschaffung des aktiven Zentrums ermöglichte. Somit ließen sich u.a. in Verbindung mit Punktmutationsstudien Protonenkanäle identifizieren. Seitdem wurden vermehrt kristallographische Strukturen der Cytochrom-*c*-Oxidase aus unterschiedlichen Familien mit teils unterschiedlichen Häm-Gruppen in immer höheren Auflösungen publiziert, die jeweils neue und detailliertere Einblicke möglich machten. Zunehmend stieg auch das Interesse an den Versuchen, das aktive Zentrum der Oxidase in verschiedenen Zwischenzuständen strukturell bestimmen zu können, wobei es grundsätzlich mehrere Methoden gibt, entsprechen Zustände mittels biochemischer Verfahren relativ langlebig zu arretieren. Fast alle bis heute publizierte Strukturen, die biochemisch definiert wurden, reflektieren dabei entweder den voll reduzierten (**R**) oder den voll oxidierten (**O**) Zustand. Doch um das katalytische Geschehen im binuklearen Zentrum besser verstehen zu können, ist der zwei-elektronen reduzierte **P** Zustand, sowie der drei-elektronen reduzierte **F** Zustand zunehmend in den Mittelpunkt der Betrachtung gerückt. Diese Zwischenzustände sind spektroskopisch gut charakterisierbar und können auch spezifisch hergestellt werden, jedoch stößt die Methodik der Röntgenkristallographie hier zunehmend an Grenzen, die kaum zu überwinden erscheinen. Ein großes Problem dabei ist, Kristalle in ausreichendem Maße herzustellen, die über eine entsprechend hohe Qualität verfügen, dabei ein sehr gutes Diffraktionsmuster besitzen und zudem noch reproduzierbar sind. Diese Voraussetzung zu schaffen – unter Einsatz von ergänzenden Chemikalien (z.B. Wasserstoffperoxid) – erweist sich im Hinblick auf ein Membranprotein als nahezu unmöglich.

Die Kryo-Elektronenmikroskopie hat in den letzten Jahren auf dem Gebiet der Strukturbiologie in erheblichem Maße an Bedeutung gewonnen durch die Verfügbarkeit immer modernerer Detektoren und Linsensysteme, was erstmals

Auflösungen von 4 Ångström und höher von makromolekularen Komplexen ermöglichte. Daher war es das Ziel dieser Arbeit, die Strukturen von aeroben Zwischenzustände (**O, P** und **F**), die der oxidativen Phase des katalytischen Zyklus zuzuordnen sind, der Cytochrom-*c*-Oxidase mittels Kryo-Elektronenmikroskope zu bestimmen sowie den voll reduzierten **R** Zustand, welcher als „Referenzstruktur" diente. Da die allgemeine Architektur der Oxidase bereits schon sehr gut beschrieben ist, stand das binukleare Zentrum im Fokus dieser Arbeit. Insbesondere der **P** und **F** Zustand waren von großem Interesse, da deren Strukturen bis heute nicht bekannt sind und mögliche Sauerstoffspezies/Sauerstoffprodukte lediglich auf Basis von spektroskopischen Untersuchungen postuliert wurden, ohne dafür einen strukturellen Beleg zu haben. Aber auch der **O** Zustand enthielt interessante Details, die aufgrund der hochauflösenden Dichtekarte identifiziert und charakterisiert werden konnten, so z.B. einen Sauerstoffkanal, der von der cytosolischen Membranseite hin zum aktiven Zentrum führt.

Ein erster, wichtiger Schritt hin zu kryoelektronischen Aufnahmen bestand in der optimierten Aufreinigung des Membranproteins. Dafür erfolgte die Orientierung primär an einem bereits vorhandenen Protokoll, wobei die Cytochrom-*c*-Oxidase nativ aus dem gram-negativen Bakterium *Paracoccus denitrificans* isoliert wurde mithilfe eines Antikörperfragments, welches an die zweite Untereinheit der Oxidase bindet und mithilfe eines Strep-*tag* aufgereinigt werden konnte. Im weiteren Prozess der Aufreinigung wurde die Homogenität des Membranprotein mittels chromatographischer Verfahren, Ionenaustauschchromatographie und Größenausschlusschromatographie, maximiert. Statt wie üblich Detergenzien zur Solubilisierung von Membranproteinen zu nehmen, wurden für die kryoelektronischen Arbeiten sogenannte Nanodiscs verwendet. Daher war es zunächst zwingend erforderlich zu überprüfen, ob die uv/vis spektroskopischen Eigenschaften der zu vermessenden Zwischenzustände sich nicht unterscheiden von jenen Spektren, die in Anwesenheit von Detergens aufgenommen wurden. Hierbei zeigte sich, dass der spektroskopische Fingerabdruck der jeweiligen Zustände sich eindeutig einstellen ließ. Zudem musste auch der rekonstituierte Membrankomplex auf seine Funktionalität überprüft werden, was mittels Sauerstoffelektrodenmessungen geschah, welche eine relativ unveränderte Umsatzrate von ca. 350 $e^-/s^{-1}$ ergab. Nach erfolgter biophysikalischer Charakterisierung des rekonstituierten

Membrankomplexes folgten die kryelektronischen Arbeiten. Das übergeordnete Ziel dieser Arbeit war es, ein katalytisch zusammenhängendes Bild des binuklearen Zentrums zu generieren, bestehend aus **O**, **R, P** und **F** Zustand.

Der **O** Zustand wurde eingestellt, indem das binukleare Zentrum des Membranproteins mithilfe von oxidiertem Kaliumhexacyanoferrat(III) vollständig oxidiert wurde. Freies Salz wurde vor der Aufnahme mittels chromatographischer Verfahren wieder abgetrennt und anschließend wurde die Proteinlösung auf eine Konzentration von 2 mg/mL verdünnt. Stöchiometrische Mengen der Proteinlösung wurden auf kupferbeschichtete Gitter pipettiert und in einem standardisierten Verfahren in flüssigem Ethan gefroren. Die Aufnahme erfolgte über ein Falcon 3 Detektorsystem, mit dessen Hilfe im Durschnitt 5000 „Filme" aufgenommen wurden. Der Durschnitt bezieht sich hier auf alle gemessenen Zwischenzustände. Die Daten wurden standardisiert mit dem Datenbearbeitungs- programm Relion 3.1 prozessiert und anschließend mittels „Coot" und „Chimera" visualisiert. Die primäre Auflösung lag bei 2.3 Å, konnte jedoch mit Hilfe eines weiteren spezifischen Algorithmus („Density modification") auf 1.9 Å verbessert werden. Die hohe Auflösung verbunden mit der hochwertigen Qualität der prozessierten Dichtekarte ermöglichte insbesondere am binuklearen Zentrum eine konkrete Zuordnung von Molekülen. Es konnte zwischen dem Eisen im Porphyrinring und dem Kupfer eine planare, längliche Dichte lokalisiert werden, die eindeutig einer Sauerstoffspezies zugeordnet werden konnte. Diese Beobachtung steht im Einklang mit bereits vorherigen Annahmen, die die Anwesenheit eines Peroxid-Dianion ($O_2^{2-}$) in dieser Position als zwingend notwendig erachten aufgrund elektrostatischer Repulsionskräfte, ausgehend von den positiven Ladungen des Eisens und des Kupfers. Zudem konnte ein Sauerstoffkanal lokalisiert und erstmals auch strukturell charakterisiert werden, dessen Anfangspunkt auf der cytosolischen Membranseite liegt und mit einer Gesamtlänge von ca. 32 Å an der Sauerstoffbindestelle am binuklearen Zentrum endet. Hier konnte eine Kette von Sauerstoffmolekülen identifiziert werden, die mutmaßlich vom umgebenden hydrophoben Umfeld transloziert werden. Der **R** Zustand diente als Referenzstruktur, da dieser Zustand ein voll reduziertes binukleares Zentrum widerspiegelt und daher nicht physiologisch relevant ist. Der Zustand wurde durch Zugabe von Natriumdithionit in Anwesenheit von atmosphärischem Sauerstoff gemessen, die Auflösung lag bei ca. 2.6 Å. Entsprechende Sauerstoffmoleküle in dem zuvor beobachten Sauerstoffkanal

im **O** Zustand waren nicht mehr zu sehen. Wie den voll reduzierten Zustand zu erwarten, war keine spezifische Dichte am binuklearen Zentrum zu beobachten. Der **P** Zustand widerspiegelt ein zwei-elektronen reduziertes binukleares Zentrum und wurde mittels Begasung von Kohlenstoffmonoxid in Anwesenheit eines basischen pH-Werts spezifisch eingestellt. Die Auflösung erreichte ähnliche Werte wie die des **O** Zustandes und ermöglichte die Identifizierung einer unbeschriebenen Dichte am binuklearen Zentrum. Diese Beobachtung ist in Anbetracht funktioneller Studien und Simulationen der letzten Jahrzehnte nahezu revolutionär, da man bisher davon ausging, dass die Sauerstoffbindung im zwei-elektronen reduzierten **P** Zustand schon gebrochen ist. Die erhaltene Dichtekarte zeigte die Anwesenheit eines homonuklearen Moleküls, eine Sauerstoffspezies. Zudem zeigte sich, dass ein zuvor beobachtetes Sauerstoff Molekül im **O** Zustand, ausgehend vom neu identifizierten Sauerstoffkanal, durch ein Wasser ersetzt ist. Hinweise wie zuvor angenommen auf eine Oxoferryl Spezies konnte hingegen nicht gefunden werden. Der **F** Zustand wurde in einem äquimolaren Verhältnis von 1:500 ($CcO/H_2O_2$) durch Wasserstoffperoxid eingestellt. Die finale Auflösung von 2.3 Å ermöglichte einen bisher nicht existenten Einblick in die strukturelle Beschaffenheit des drei-elektronen reduzierten binuklearen Zentrums. Hierbei war, wie schon von spektroskopischen Arbeiten postuliert, keine Dichte zwischen den Metallen zu sehen. Stattdessen konnte hier die Dichte mit der Anwesenheit einer Oxoferryl Spezies erklärt werden. Es gab keine strukturellen Hinweise auf ein vom Kupfer koordiniertes Hydroxdion oder Wasser, dass geometrisch korrekt angeordnet wäre. Interessanterweise konnte eine prominente Dichte in unmittelbarer Nähe zum aktiven Zentrum lokalisiert werden, die eine Sauerstoffspezies eindeutig repräsentiert. Diese Beobachtung wiederum steht im Einklang mit vorherigen Annahmen, basierend auf EPR und Katalase Studien. Die hier gezeigten hochauflösenden Strukturen bieten ein sehr gutes Fundament für weitere theoretische Simulationen, um andere bisher unbeantwortete Fragen, insbesondere bezüglich der Protonkanäle und der Elektronen- und Protonenreorganisation innerhalb des binuklearen Zentrums, adäquat zu adressieren.

## 10. Publications

**F. Kolbe,** S. Safarian, Ż. Piórek, S. Welsch, H. Müller, H. Michel. Cryo-EM structures of intermediates suggest an alternative catalytic reaction cycle of cytochrome *c* oxidase (Nature Communications, accepted 25$^{th}$ November 2021)